UNIVERSIDADE FEDERAL DE SÃO CARLOS
CENTRO DE CIÊNCIAS EXATAS E DE TECNOLOGIA
DEPARTAMENTO DE QUÍMICA
PROGRAMA DE PÓS-GRADUAÇÃO EM QUÍMICA

"ANÁLISE TEÓRICA-EXPERIMENTAL DE SEMICONDUTORES"

Mateus Meneghetti Ferrer*

Tese apresentada como parte dos requisitos para obtenção do título de DOUTOR EM CIÊNCIAS, área de concentração: FÍSICO-QUÍMICA.

Orientador: Elson Longo

São Carlos - SP
2016

Folha de Aprovação

Assinaturas dos membros da comissão examinadora que avaliou e aprovou a Defesa de Tese de Doutorado do candidato Mateus Meneghetti Ferrer, realizada em 07/03/2016:
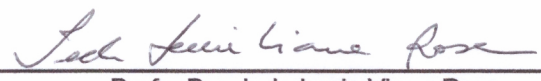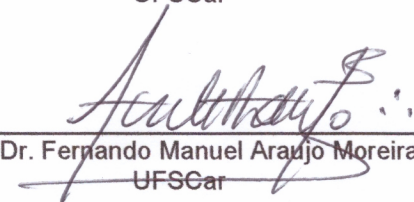
Prof. Dr. Elson Longo da Silva
UFSCar

Prof. Dr. Júan Manuel Andrés Bort
UJI/Espanha

Prof. Dr. Máximo Siu Li
USP

Profa. Dra. Ieda Lucia Viana Rosa
UFSCar

Prof. Dr. Fernando Manuel Araújo Moreira
UFSCar

PUBLICAÇÔES

Publicações Presentes

1. FERRER M. M., GOUVEIA A. F., GRACIA L., LONGO E. & ANDRÉS, J. "A 3D platform for the morphology modulation of materials: first principles calculations on the thermodynamic stability and surface structure of metal oxides: Co_2O_3, α-Fe_2O_3, and In_2O_3". Model. Simul. Mater. Sc., **24**: 025007, 2016.

2. ANDRÉS J., FERRER M. M., GRACIA L., BELTRAN A., LONGO V. M., CRUVINEL G. H., TRANQUILIN R. L. & LONGO E. "A Combined Experimental and Theoretical Study on the Formation of Ag Filaments on β-Ag_2MoO_4 Induced by Electron Irradiation". Part. Part. Syst. Char., **32**: 646, 2015.

3. LONGO E., VOLANTI D. P., LONGO V. M., GRACIA L., NOGUEIRA I. C., ALMEIDA M. A. P., PINHEIRO A. N., FERRER M. M., CAVALCANTE L. S. & ANDRÉS J. "Toward an Understanding of the Growth of Ag Filaments on α-Ag_2WO_4 and Their Photoluminescent Properties: A Combined Experimental and Theoretical Study". J. Phys. Chem. C, **118**: 1229-1239, 2014.

4. FERRER M. M., DE SANTANA Y. V. B., RAUBACH C. W., LA PORTA F. A., GOUVEIA A. F., LONGO E. & SAMBRANO J. R. "Europium doped zinc sulfide: a correlation between experimental and theoretical calculations". J. Mol. Model., **20**: 2375, 2014.

5. ANDRÉS J., GRACIA L., GONZALEZ-NAVARRETE P., LONGO V. M., AVANSI W., VOLANTI D. P., FERRER M. M., LEMOS P. S., LA PORTA F. A., HERNANDES A. C. & LONGO E. "Structural and electronic analysis of the atomic scale nucleation of Ag on α-Ag_2WO_4 induced by electron irradiation". Sci. Rep., **4**: 5391, 2014.

Outras Publicações

6. ANDRÉS J., GRACIA L., GOUVEIA A. F., FERRER M. M. & LONGO E. "Effects of surface stability on the morphological transformation of metals and metal oxides as investigated by first-principles calculations". Nanotechnology, **26**: 405703, 2015.

7. ROSA I. L. V., OLIVEIRA M. C., ASSIS M., FERRER M. M., ANDRÉ R. S., LONGO E. & GURGEL M. F. C. "A theoretical investigation of the structural and electronic properties of orthorhombic $CaZrO_3$". Ceram. Int., **41**: 3069-3074, 2015.

8. GOUVEIA A. F., SCZANCOSKI J. C., FERRER M. M., LIMA A. S., SANTOS M. R. M. C., LI M. S., SANTOS R. S., LONGO E. & CAVALCANTE L. S. "Experimental and Theoretical Investigations of Electronic Structure and Photoluminescence Properties of β-Ag_2MoO_4 Microcrystals". Inorg. Chem., **53**: 5589-5599, 2014.

9. LONGO V. M., DE FOGGI C. C., FERRER M. M., GOUVEIA A. F., ANDRÉ R. S., AVANSI W., VERGANI C. E., MACHADO A. L., ANDRÉS J., CAVALCANTE L. S., HERNANDES, A. C. & LONGO E. "Potentiated Electron Transference in α-Ag_2WO_4 Microcrystals with Ag Nanofilaments as Microbial Agent". J. Phys. Chem. A, **118**: 140305132037000, 2014.

10. RAUBACH C. W., POLASTRO L., FERRER M. M., PERRIN A., PERRIN C., ALBUQUERQUE A. R., BUZOLIN P. G. C., SAMBRANO J. R., DE SANTANA Y. B. V., VARELA J. A. & LONGO E. "Influence of solvent on the morphology and photocatalytic properties of ZnS decorated CeO_2 nanoparticles". J. Appl. Phys., **115**:213514, 2014.

11. RAUBACH C. W., GOUVEIA A. F., DE SANTANA, Y. V. B., VARELA J. A., FERRER M. M., LI M. S. & LONGO E. "Towards controlled synthesis and better understanding of blue shift of the CaS crystals". J. Mat. Chem. C, **2**: 2743, 2014.

12. LA PORTA F. A., FERRER M. M., DE SANTANA Y. V. B., RAUBACH C. W., LONGO V. M., SAMBRANO J. R., LONGO E., ANDRÉS J., LI M. S. & VARELA J. A. "Synthesis of wurtzite ZnS nanoparticles using the microwave assisted solvothermal method". J. Alloys Compd, **556**: 153-159, 2013.

13. RAUBACH C. W., FERRER M. M., DE SANTANA Y. V. B., PRESCILA B. C., SAMBRANO J. R. & LONGO E. "Photocatalytic activity of semiconductor sulfide heterostructures". Dalton Trans., **42**: 11111-11116, 2013.

14. FERRER M. M., DE SANTANA Y. V. B., RAUBACH C. W., SAMBRANO J. & LONGO E. "Experimental and Theoretical Studies of Photoluminescence in ZnS Obtained by Microwave-Assisted Solvothermal Method". Curr. Phys. Chem., **3**: 413-418, 2013.

15. LA PORTA F., FERRER, M. M., DE SANTANA, Y. V. B., RAUBACH C. W., LONGO V., SAMBRANO J., LONGO E., ANDRÉS J., LI M. S. & VARELA J. "Towards an Understanding on the Role of Precursor in the Synthesis of ZnS Nanostructures". Curr. Phys. Chem., **3**: 378-385, 2013.

16. RAUBACH C. W., BUZOLIN P. G. C., DE SANTANA, Y. V. B., LONGO E., LONGO V. M., VARELA J. A., AVANSI W., FERRER M. M. & SAMBRANO J. R. "Strutural and optical approach of CdS@ZnS core shell system". Chem. Phys. Lett., **536**: 96-99, 2012.

17. MOREIRA M. L., LONGO V. M., AVANSI W., FERRER M. M., ANDRÉS J., MASTELARO V. R., VARELA J. A. & LONGO E. "Quantum Mechanics Insight into the Microwave Nucleation of $SrTiO_3$ Nanospheres". J. Phys. Chem. C, **116**: 24792-24808, 2012.

AGRADECIMENTOS

LIST OF TABLES

LIST OF FIGURES

FIGURE 1 – TEM images of the formation of Ag filaments from the a-Ag$_2$WO$_4$ bulk. (a) and (b) TEM images obtained at different magnifications indicate a smooth and clear surface. (c)–(f) Thick Ag filaments grow at the edge of the sample, whereas

2.3 – Toward an Understanding of the Growth of Ag Filaments on α-g$_2$WO$_4$ and Their photoluminescent Properties: A Combined Experimental and Theoretical Study

2.4 – A Combined Experimental and Theoretical Study on the Formation of Ag Filaments on β-Ag$_2$MoO$_4$ Induced by Electron Irradiation

2.5 – A 3D platform for the morphology modulation of materials: first principles calculations on the thermodynamic stability and surface structure of metal oxides: Co$_3$O$_4$, α-Fe$_2$O$_3$ and In$_2$O$_3$

RESUMO

ANÁLISE TEÓRICA-EXPERIMENTAL DE SEMICONDUTORES

A rápida modernização dos polos industriais e tecnológicos faz com que o desenvolvimento de novos materiais seja fundamental, sempre pesquisando maiores eficiências e menores custos. Por outro lado, a expressão "novos materiais" não está somente relacionada à uma nova classe ou composto obtidos pela primeira vez, mas também às modificações estruturais de materiais já conhecidos, incluindo o efeito do tamanho, forma e incorporações sinergéticas. Neste contexto, pesquisas usando modelos teórico-experimentais tendem a ser cada vez mais comuns devido à melhor correlação entre características do sistema e propriedades. Por tanto, interpretações mais claras e precisas podem auxiliar no planejamento e desenvolvimento de novos materiais. No presente trabalho, um conjunto de modelos teórico-experimentais foi construído a fim de explicar propriedades e fenômenos de semicondutores. Os semicondutores escolhidos foram: α-Ag_2WO_4, β-Ag_2MoO_4, Co_3O_4, α-Fe_2O_3 e In_2O_3. Técnicas de caracterização de Difração de Raios-X, refinamento Rietveld, espectroscopia Raman, microscopia de varredura e microscopia de transmissão foram vinculadas com cálculos mecânico-quânticos para um melhor entendimento dos resultados observados. Resultados teóricos de estrutura de bandas e densidade de orbitais corroboraram com os "band gaps" experimentais. Os dados mostraram a criação de novos estados na região proibida do "band gap" devido à criação de defeitos, por meio de dopagem ou mudanças estruturais. Os modelos finais foram utilizados para melhor explicar as modificações das propriedades fotoluminescentes. Cálculos mecânico-quânticos também foram utilizados para explicar o fenômeno de crescimento de prata em cristais de α-Ag_2WO_4 e β-Ag_2MoO_4 com a adição de elétrons. Neste modelo, a redução da prata resulta em seu afastamento dos "clusters" gerando o aparecimento de filamentos de prata metálica na superfície dos materiais. Por fim, foi criada uma nova abordagem sobre o mapeamento e previsão de morfologias de cristais, servindo como um referencial experimental para a comparação entre superfícies e propriedades finais. Os trabalhos presentes consistem em estudos interdiciplinares, do fundamento até a aplicação de diversos materiais, e mostram como a química quântica e outros meios teóricos podem ser usados para o etendimento de propriedades para o "design" de novos materiais.

ABSTRACT

THEORETICAL AND EXPERIMENTAL ANALYSIS OF SEMICONDUCTORS

The rapid modernization of industrial and technological poles spurs the development of new materials, always in search of efficiency and low costs, given that the expression "new materials" does not relate just to the new classes or compounds never seen before but also to the structural modifications in materials already studied. In this context, research using theoretical and experimental models tends Researches using combined theoretical and experimental methods tend to be more and more commonly due to the better correlation between system characteristics and properties. However, a better interpretation can assists in the planning and developing of new materials. In the present study, a set of theoretical and experimental models were built in order to explain the properties and phenomena of semiconductors. The chosen materials were the α-Ag_2WO_4, β-Ag_2MoO_4, Co_3O_4, α-Fe_2O_3 and In_2O_3. Characterization techniques of X-Ray difraction, Rietveld refinament, Raman spectroscopy, scanning electron microscopy and transmission electron microscopy were related with quantum mechanical calculations to a better understanding of the observed results. Theoretical results of band structure and density of states are in agreement with the experimental band gaps.The data showed a creation of new eletronic states on the forbiden region on the band gap due to the criation of structural defects, by means of a impurity or structural changes. The final models were used to a better explanation of the photoluminescent properties modifications. Quantum mechanical calculations were also used to the explanation of a phenomenon caused by electron bombing, which was observed in Ag_2WO_4 and Ag_2MoO_4 crystals. In this model, the Ag reduction results in its removal of the clusters generating the Ag metallic filaments on the material surface. Finally, it was created a new approach about the mapping and prediction of crystals morphology that serves as an experimental reference to the comparison between surface and final properties. The presented papers consist in an interdisciplinary research, from fundamental to applications and show how quantum chemical and other theoretical computational means can be used for an understanding of physical and chemical properties of materials for searching a rational materials design.

SUMMARY

1 – INTRODUCTION

The rapid modernization of industrial and technological poles spurs the development of new materials, always in search of efficiency and low costs, given that the expression "new materials" does not relate just to the new classes or compounds never seen before but also to the structural modifications, including size effect or synergetic incorporations in materials already studied. Ceramic materials are an important group that can be used as example. Ceramic is one of the most ancient industries on the planet but it has followed the footsteps of changing need.[1]

In order to study new possibilities of materials applications, it considers that the morphology, dimensionality, and crystal structure all play important roles in the electronic, optical, magnetic, catalytic, chemical, and other physical properties.[2, 3]

Due to the difficulty of measuring structures and processes, principally at the nanoscale, it is extremely valuable to combine experiments and computational modeling. This synergy between theory and experiment has been initiated already many years ago. For example, the reconstruction of Si surfaces was determined 30 years ago with significant input from theory.[4]

Both fields, theoretical and experimental, have their advantages and limitations. Even the experimental methods of characterization are more and more evolved and accurate, the explanation of the facts at atom scale is not so tangible yet. On the other hand, the richness of details of real systems over multiple length and time scales poses limitations on the capacity to simulate with atomics detail of a high level of accuracy. Therefore, part of the limitations is clearly excluded when the theory and experiment work together.

A great diversity of tools has been created and improved to the calculation of chemistry structures in order to circumvent some limitations, as example the size. Large system simulations, as crystalline lattices, involve a high number of atoms and, consequently, an enormous number of electrons. For this, some programs include periodic models, making with that a created unit cell may be replicated to the infinite in the Cartesian directions to reproduce crystals of all types.[5-7] Such periodic models allowed a great progress in the prevision and explanation in the materials science field.

Researches using combined theoretical and experimental methods tend to be more and more commonly due to the better clarity of the interpretation and connections between the results. Focusing on the articles regarding to the presented study, a large variety of subjects can be better treated by these methods, e.g. the study of the electronic bands, redox reaction, structural stabilization, defects and surfaces. By means of these studies, optical properties, structural defects, influence of impurities, redox reactions, and morphology can be explained more effectively.

The studied materials presented here were chosen due to their importance in level of user application or the need of new methods to the explanation of the properties and phenomena. It is the case of the Zinc sulfide (ZnS). The ZnS is an important II-IV semiconductor material with a wide band gap.[8] It has a wide range of applications for flat-panel displays, optical sensors, IR windows, catalysts, lasers, etc.[9-11] By doping the ZnS with different metal ions, it is possible to realize full-color luminescence in the UV–visible region.[12] Thus, a number of publications concerning well-formed ZnS nanocrystals doped with various types of impurities have appeared in recent years.[13-15] In addition, impurities can produce drastic changes in optical behaviors. These effects can be used as an important tool in lighting and display areas. Therefore, theoretical models can be very useful to explain how the impurities act on the electronic bands helping with the experimental planning for devices.

Recently, silver molibdates and tungstates have been the focus of investigations by our group; we have synthesised this material using different methods (coprecipitation, sonochemistry and hydrothermal synthesis) and have studied their properties.[16] In both materials, the formation of Ag filaments on crystal, via irradiation of electrons by an accelerated electron beam from an electron microscope under high vacuum, was observed, and the corresponding potential applications were investigated. The current investigation is motivated by our incomplete understanding of the underlying fundamental phenomena and mechanisms driving the nucleation and growth of Ag filaments. While the concept of crystal a wide range of material properties, in reality, disorder is ubiquitous and is capable of drastically influencing various properties.[17] The creation of the theoretical and experimental model presented here is also to understand the basis of the early-nucleation and -growth of Ag filaments after the irradiation process.

The current combination of theory, simulation, and experiment is not only capable of developing new functional materials with predictable and desirable

properties, but also enables us to understand the nature of micro and nano-structures with novel morphologies.

Control of the morphology of micro and nanocrystals depends on factors such as the internal structure of the crystal and the external growth conditions. The surface facet energies can be modified by the use of different synthetic methods, reaction times, the nature of surfactants etc. In this sense, the rational design of nanomaterials is one of the holy grails of nanoscience and nanotechnology. The precise regulation and controlled synthesis of specific morphologies is crucial to enhance their performance in practical applications of micro and nanomaterials.[18]

Among the articles presented here, it was introduced recent work, based on the joint use of experimental findings and first principle calculations, so as to give deeper knowledge on the electronic, structural and energetic properties controlling the morphology and the transformation mechanism of different metals oxides.

These investigations are useful to gain further understanding of how to achieve morphological control of complex three dimensional crystals by tuning the ratio of the surface energy values of the different facets. This strategy allows the prediction of possible morphologies for a crystal and/or nanocrystal by controlling the relative values of surface energies.

Predicting the 3D morphologies of crystalline materials can be used to guide the analysis of field-emission scanning electron microscopy images of the materials, and could be a very useful tool to design the synthesis of new materials. However, there are many scientific and technological challenges to overcome; in particular, it is necessary to understand the relationship between properties and structure.

The overriding goal of this joint project was to conduct interdisciplinary research, from fundamental to applications, in materials of different sizes. Some results using theoretical and experimental models are discussed in these papers and show how quantum chemical and other theoretical computational means can be used for an understanding of physical and chemical properties of materials for searching a rational materials design.

2 – PUBLISHED ARTICLES

Published articles with the association of theory and experiments can be found at the following pages.

2.1 – Europium doped zinc sulfide: a correlation between experimental and theoretical calculations

ORIGINAL PAPER

Europium doped zinc sulfide: a correlation between experimental and theoretical calculations

Mateus M. Ferrer · Yuri V. B. de Santana ·
Cristiane W. Raubach · Felipe A. La Porta ·
Amanda F. Gouveia · Elson Longo · Julio R. Sambrano

Abstract
This paper presents the correlation among electronic and optical property effects induced by the addition of different concentrations of europium (Eu^{3+}) in zinc sulfide (ZnS) by microwave-assisted solvothermal (MAS) method. A shift of the photoluminescence (PL) emission was observed with the increase of Eu^{3+}. The periodic DFT calculations with the B3LYP hybrid functional were performed using the CRYS TAL computer code. The UV–vis spectra and theoretical results indicate a decrease in behavior of the energy gap as a function of dopant concentration. Therefore, new localized states are generated in the forbidden band gap region, the new states increase the probability of less energy transitions which may be responsible for a red shift in the PL bands spectrum.

Keywords B3LYP · DFT · Doping process · Eu · Microwave · Photoluminescence · ZnS

M. M. Ferrer · Y. V. B. de Santana · C. W. Raubach · A. F. Gouveia
INCTMN-UFSCar, Universidade Federal de São Carlos,
P.O. Box 676, 13565-905 São Carlos, SP, Brazil

F. A. La Porta · E. Longo
INCTMN-UNESP, São Paulo State University, P.O. Box 355,
14801-907 Araraquara, SP, Brazil

J. R. Sambrano (✉)
Grupo de Modelagem e Simulação Molecular, INCTMN-UNESP,
São Paulo State University, P.O. Box 473, 17033-360 Bauru, SP,
Brazil
e-mail: sambrano@fc.unesp.br

Introduction

Luminescent materials such as rare earth doped powders have attracted attention due to their possible photonic applications [1–4]. Among several rare earths reported, trivalent europium (Eu^{3+}), which has been recognized as efficient luminophore, is one of the most studied, mainly due to non-degenerated levels involved in electronic transitions [5–8]. Emission spectra of the Eu^{3+} ion show narrow sharp bands due to 4f-4f intraconfiguration transitions protection by external $5s^2$ and $5p^6$ sub-shells [9]. For this reason, the Eu^{3+} ion is used as luminescent probe because it is little affected by chemical environment changes; this characteristic may be important to improve the development of materials science.

Furthermore, the doping process in semiconductors produces changes in structural and electronic properties of materials, which is an efficient way to further enhance their properties and applications [10]. A suitable host must also possess a large optical band gap as well as good solubility and stability. In particular, zinc sulfide (ZnS) is suitable as a host matrix. It is an important II-VI semiconductor material with a wide band gap (about 3.72 eV for the cubic zinc blende phase, and 3.77 eV for the wurtzite phase in bulk materials at 300 K) [11–13]. By doping with different metal ions (including transition metals and rare earths), it is possible to realize full-color luminescence in the UV–visible region [14]. Thus, a number of publications concerning well-formed ZnS nanocrystals doped with various types of impurities have appeared in recent years [15–18]. In addition, impurities can produce drastic changes in optical behaviors. These effects can be used as an important tools in lighting and display areas.

Eu^{3+} as a dopant in ZnS has been prepared by chemical vapor deposition (1073 K and 10 min), solid-state reaction (1573 K and 60 min), sol–gel, solvothermal (413 K and 300 min) and other synthetic methods [15–17, 19]. Therefore, it is important to develop new low cost and

environmently friendly processing material methods with the possibility of the formation of materials at the micro and nanoscale level with well-defined morphologies. Recently, the microwave-assisted solvothermal (MAS) method has emerged as an alternative in field of powder preparation with both expected and unexpected merits; e.g., kinetic enhancement, low reaction temperature and time reduction as well as the control of the overall particle size and aggregation process [20, 21]. The ability to achieve a high temperature stable phase at very low temperatures not only provides an economically viable route for applications, but also opens a new way to study the structural kinetics and chemistry of nanocrystals and various functional materials [22–24]. Very recently, our group conducted experimental studies of ZnS and CdS obtained with MAH method and showed its ease and efficiency enabling a range of studies that can be done. In the case of ZnS, it was possible to obtain the organized phase in 413 K and 1 min [23–26].

Changes induced by addition of different concentrations of Eu^{3+} (1, 2 and 4 %) in the pure ZnS prepared by the MAS method are reported. A systematic investigation of the structural, electronic, and optical properties of doped ZnS zinc-blend (cubic) structure as a function of different concentrations of Eu^{3+}. In order to explain experimental outcomes, quantum mechanical results were calculated based on the density functional theory (DFT) at the B3LYP level. Changes caused in optical properties illustrate the kinds of defects which are caused by europium addition.

Methods

Sample preparation

To obtain pure ZnS, anhydrous $ZnCl_2$ (3.67 mmols) was dissolved in 25 mL of ethylene glycol. Subsequently, 4.74 mmols of tetramethylammonium hydroxide (TMAH) in a methanol solution was added (solution 1). Separately, 3.67 mmol of thiourea was dissolved in 25 mL of ethylene glycol (solution 2). Under stirring, solution 2 was quickly added into solution 1. The resulting solution was transferred to a reactor coated with polytetrafluoroethylene (PTFE) and placed into a domestic Microwave-Solvothermal (MS) system (2.45 GHz, maximum power of 800 W). The MAS processing was performed at 413 K for 16 min. The resulting solution was washed with deionized water and ethanol several times to neutralize the solution pH (≈7) and the precipitates were finally collected and dried at 343 K for 24 h.

Different concentrations of $EuCl_3$ were dissolved in solution 1 according to the desired dopant concentration (1, 2 and 4 % nominal) to obtain the ZnS doped with Eu^{3+} (ZnS:Eu).

Characterization techniques

The obtained powders were characterized by X-ray diffraction (XRD) (Rigaku DMax 2500PC using Cu $K_{\alpha 1}$ (λ=1.5406 Å) and Cu $K_{\alpha 2}$ (λ=1. 54434 Å) radiation setup) and field emission scanning electron microscopy (FE-SEM) (Supra 35-VP, Carl Zeiss, Germany). Ultraviolet–visible (UV–vis) spectroscopy (Cary 5G equipment) provided optical reflectance spectra of ZnS powders.

PL spectra were collected with a Thermal Jarrel-Ash Monospec monochromator and a Hamamatsu R446 photomultiplier. The 350.7 nm exciting wavelength of a krypton ion laser (Coherent Innova) was used; the output of the laser was maintained at 200 mW. All measurements were taken at room temperature.

An inductively coupled plasma atomic emission spectrometer (ICP-AES) simultaneous CCD–VISTA–MPX (Varian) with a radial configuration was used for the chemical analysis of ca. 0.0200 g samples. The dissolution procedure was conducted using 10 mL of HCl (37 % purity) in closed vessels at room temperature. Analytical blanks were prepared following the same acid digestion procedure, and the final 100 mL sample solutions were diluted with de-ionized water.

Model system and computational method

Several theoretical research works are based on DFT theory for studies in materials science. Periodic DFT calculations have demonstrated that they are able to reproduce with accuracy the electronic structure of solid state systems. In this study, the periodic DFT calculations with the B3LYP hybrid functional [27, 28] were performed using the CRYSTAL06 computer code [29], which has been successfully employed for studies of electronic and structural properties of diverse compounds [30–33]. CRYSTAL is an ab initio (Hartree-Fock and DFT) LCAO program for the treatment of periodic systems. LCAO, in the present case, means that each crystalline orbital is a linear combination of Bloch functions.

The level of accuracy of the calculation of Coulomb and the exchange series is controlled by five parameters. The 8, 8, 8, 8, 14 parameters was chosen for the Coulomb overlap, Coulomb penetration, exchange overlap, first exchange pseudo-overlap, and second exchange pseudo overlap parameters, respectively. The integration in the reciprocal space was performed by sampling the Brillouin zone with an 6x6x6 pack-Monkhorst.

The ZnS zinc-blend (cubic) structure has just one lattice parameter "a" with two atoms per unit cell; with atomic positions: (0,0,0) and (0.25,0.25,0.25) for Zn and S atoms, respectively.

The atomic centers are described by the entire electron basis set 86-411d31G [34] for Zn and 86-311G* for S [35] atoms. For europium atoms, it is convenient to avoid core
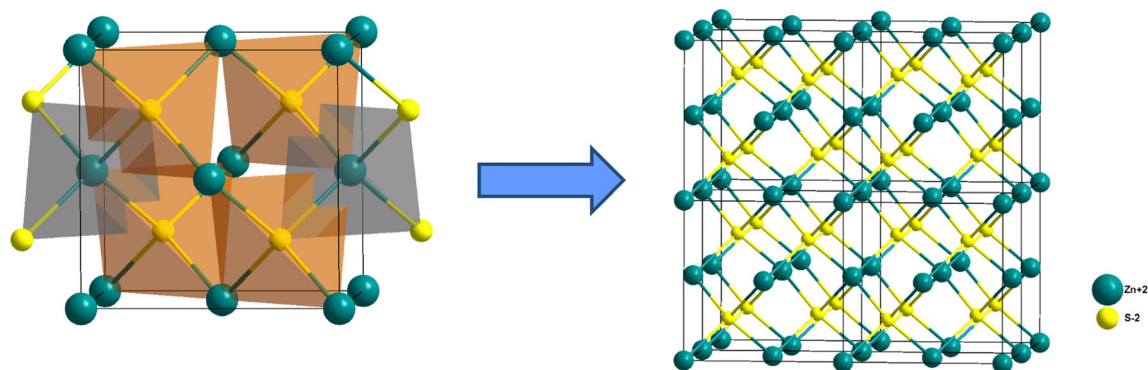
Fig. 1 Pure ZnS 2x2x2 supercell

electrons, and adopt the well-assessed effective core pseudopotential (ECP) techniques [36, 37]. The large-core ECP basis, ECP52MWB [38, 39] (http://www.theochem.uni-stuttgart.de/pseudopotentials) has been chosen to represent the Eu^{3+} in this work. To the best of our knowledge this basis set is the only pseudopotential available and there is no all-electron basis set available to be used in the CRYSTAL program.

A full optimization procedure was carried out to determine the zinc blend equilibrium geometry. The optimized and experimental values (given in parentheses) are $a=5.516$ (5.40) Å[40].

From this optimized lattice parameter, two 2x2x2 supercell periodic models were used to study the pure and doped ZnS. This supercell contains 32 ZnS units, totaling 64 atoms. The first represents the pure ZnS (p-ZnS) and the second one represents the doped ZnS (d-ZnS) where one Eu atom replaces one Zn atom, resulting in 3.125 % Eu. These models can be useful to represent different behavior and properties in the material.

Figure 1 illustrates a schematic representation for pure ZnS supercell. A new optimization procedure of d-ZnS supercell

was made to determine the equilibrium geometry. For these simulations we recommend the use of a symmetric supercell (2x2x2). The new calculated cell parameter is $a=5.576$ Å, very close to the previous results presented here. The computational cost is dependent on the sueprcell size, large models can be prohibitive.

The band structures were calculated for 100 K points along the appropriate high-symmetry paths of the adequate Brillouin zone. Diagrams of the density of state (DOS) were obtained for analysis of the corresponding electronic structure.

Results and discussion

Figure 2 illustrates XRD patterns of the samples with three different concentrations of Eu^{3+} in the microwave synthesis which were used to analyze the long-range order. The diffraction peaks indicate a cubic structure which is in agreement with the JCPDS card: 67–790 [40]. Differences observed between the samples indicate structural changes. With the increase of Eu^{3+}, diffraction peaks became broader and less defined which is probably due to ineffective ordering of the lattice. Results of all samples indicate just ZnS diffraction peaks.

Another important aspect concerning the diffraction peaks exposed in Fig. 2 is the significant broadening of the most intense reflections in the XRD patterns which shows the
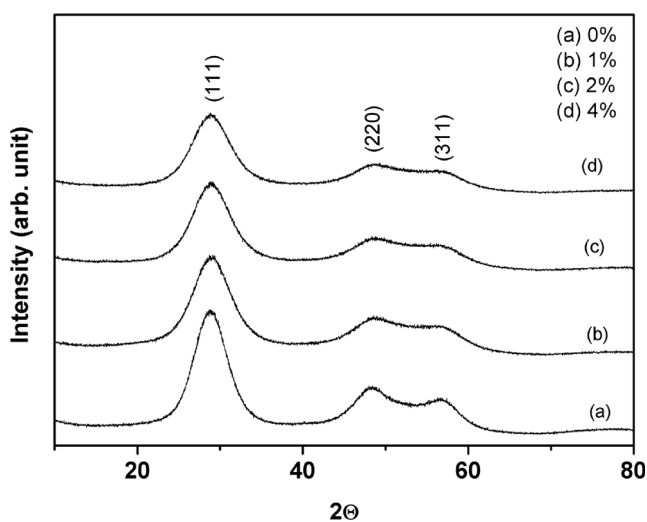
Fig. 2 XRD patterns of ZnS powders with **a**) 0, **b**) 1, **c**) 2, and **d**) 4 % of Eu^{3+} processed in a MAS system at 413 K for 16 min

Table 1 Average of crystallite sizes and ICP-AES results of the ZnS pure and with different Eu^{3+} concentrations

Samples	Crystallite sizes (nm)	ICP-AES	
		Expected	Result
Pure ZnS	3.36	0 %	0 %
ZnS:Eu 1 %	3.01	1 %	1.2 %
ZnS:Eu 2 %	3.00	2 %	2.1 %
ZnS:Eu 4 %	2.94	4 %	2.8 %

Fig. 3 FE-SEM images of **a**) pure ZnS and **b**) ZnS:Eu 4 %
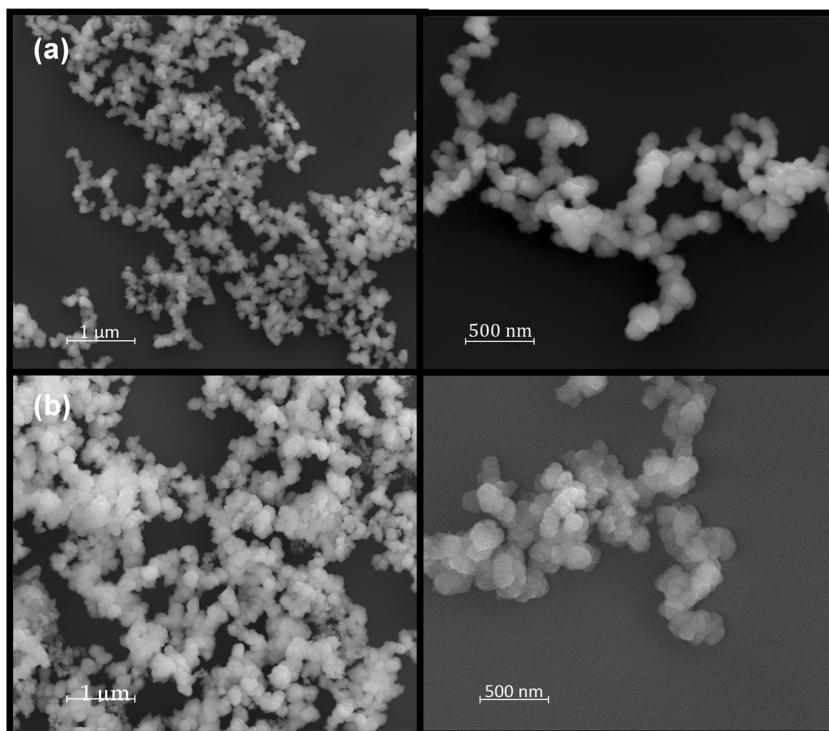
extent europium is incorporated into the ZnS structure and suggests a decrease in the crystallite size of the material obtained by the MAS method. The average crystallite size of all samples was estimated using the Debye-Scherer method [41]. The equation below encompasses the spherical shape and reduced size of the sample.

Average crystallite size of material t = $k\lambda/\beta \cos\theta$ (01)

where, k is a constant; λ is the wavelength of the x-rays in nm; β is the full width half maximum (FWHM) of the major peak in radians as calculated from XRD peaks data and θ is the diffraction angle.

Estimated size values using the main peak are depicted in Table 1. With the addition of europium, there is an initial decrease in the size, but little variation occurs with the increase of dopant concentration.

To evaluate the dopant arrangement as a substitution ion (or even as a superficial element) a chemical analysis is fundamental. Table 1 shows the expected values of Eu^{3+} calculated according to the amount of precursors added and the results of the ICP-AES technique.

These ICP-AES results indicate that pure ZnS, ZnS:Eu 1 % and ZnS:Eu 2 % are in agreement with the expected

Fig. 4 UV–vis spectra of ZnS powders with a) 0 %, b) 1 %, c) 2 %, and d) 4 % of Eu^{3+}
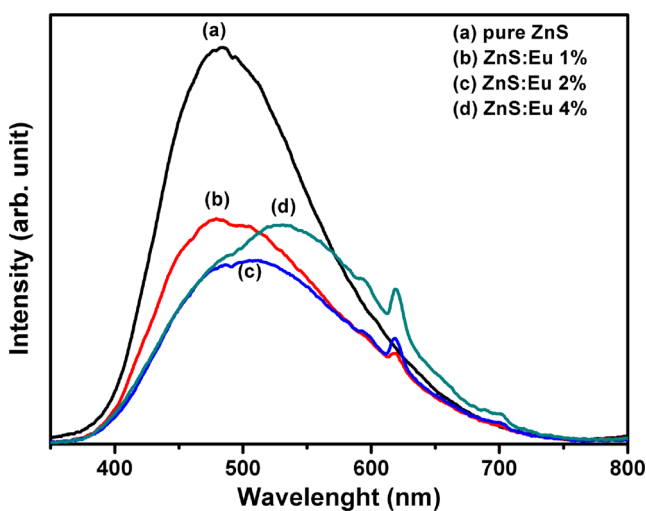
Fig. 5 PL spectrum of ZnS powders at room temperature ($\lambda_{excitation}$= 350.7 nm); a) pure ZnS, b) ZnS:Eu 1 %, c) ZnS:Eu 2 %, and d) ZnS:Eu 4 %
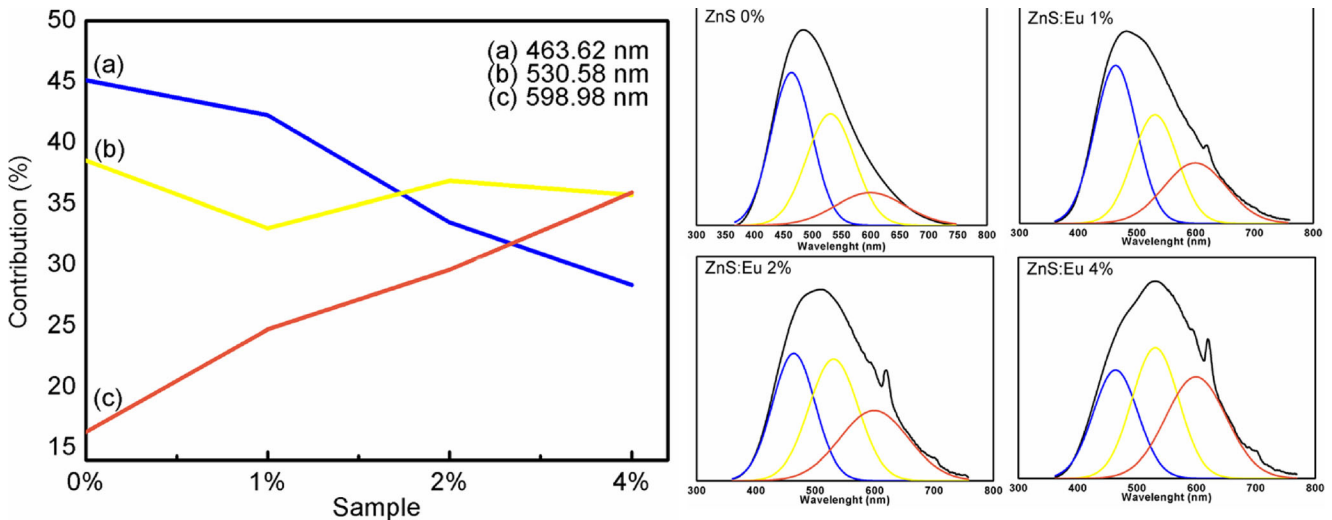
Fig. 6 Deconvoluted PL bands of three curves centered at 463.62 nm, 530.58, nm and 598.98 nm and their contributions

percentage of doping; however, the Zns:Eu 4 % result shows a considerable difference which indicates that Eu^{3+} maximum percentage was achieved in the lattice by this method. The percentage of Eu in relation to Zn is slightly lower than expected mainly due to the ZnS synthesis yield.

Figure 3 shows a FE-SEM image for pure and ZnS:Eu 4 % after 16 min in the microwave. In both cases, the particles are agglomerated, spherical, and of varying sizes. These conditions were not sufficient to avoid the agglomeration and possible particle coalescence. No major differences were observed between the samples.

Gap energy values can be obtained by the Wood and Tauc method [42] using UV–vis spectroscopy (see Fig. 4).

The UV–vis spectra indicate a decrease in behavior of the energy gap as a function of dopant concentration (3.72 eV to 3.55 eV). Clusters formed by the europium replacement, EuS_4, create a different local charge density when compared with ZnS_4 clusters. Furthermore, the different dopant charge can provide the formation regarding vacancies or interstitial

defects (due to the different charge density of Eu^{3+} ion) in the ZnS host lattice. These defects introduce a symmetry breakdown and, as a consequence, an introduction of a new energy level in the forbidden region. Several research works show the variation of the semiconductor band gap caused by structure change [43–46].

Figure 5 shows the PL emission spectra of pure and doped ZnS powders recorded at room temperature with excitation at 350.7 nm. The emission spectra show a broad band centered at ~484 nm which may be attributed to ZnS matrix, and the profile of emission band is typical of a multi-phonon and multilevel; i.e., a system in which relaxation occurs by several paths involving the participation of numerous states within the band gap of the semiconductor.

The PL emission spectra of doped ZnS powders show that the maximum emission bands are centered at 498, 510, and 534 nm, for 1 %, 2 %, and 4 % Eu^{3+}, respectively. Therefore, a red shift emission was observed with the increase of europium concentration. The emission spectra show the characteristic narrow band assigned to $^5D_0$-$^7F_2$ transitions in Eu^{3+} at 612 nm
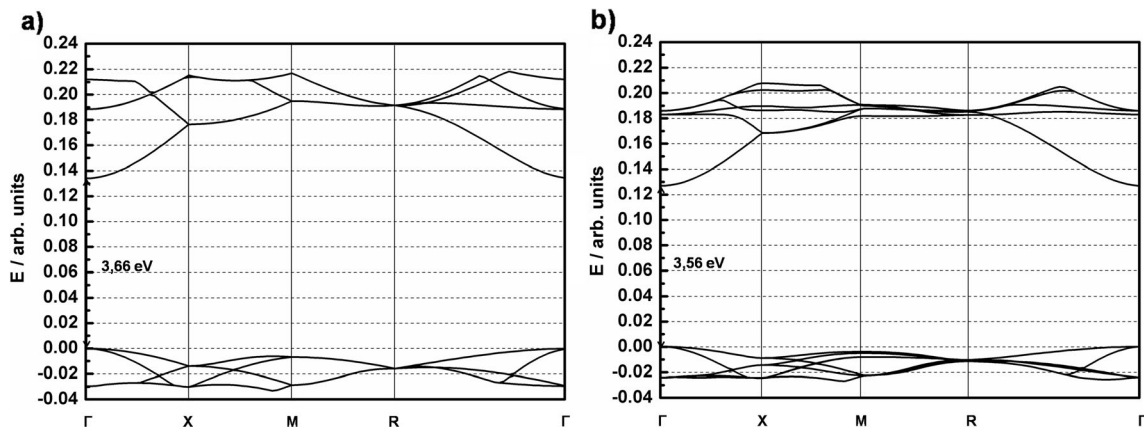
Fig. 7 Band structures of **a)** p-ZnS and **b)** d-ZnS models

in all doped samples. This suggests the incorporation of Eu^{3+} ion in the ZnS nanoparticles did not change its radiative relaxation processes. The red shift effect denotes a strong influence of the europium orange lines emission associated to the allowed transitions originated from electronic reconfiguration.

To obtain a better understanding about the PL modifications in relation to the structural defects caused by the dopant, PL emission spectra were analyzed using decomposition PeakFit. The contribution of each deconvoluted curve and its variations are depicted in Fig. 6. Upon deconvolution, three pseudo-voids were chosen to describe the emissions; i.e.,

463.62 nm (blue), 530.58 nm (yellow), and 598.98 nm (orange) labeled as *a*, *b*, and *c*, respectively.

Pure ZnS has a greater contribution from the blue region; however, with the addition of europium and its increase, the contributions from the blue region decrease while the contribution from the orange region increases. The europium, besides its well defined bands, has modified the wide band of the matrix in the region between the orange and the red emissions, which indicates deep defects as a consequence of a different charge density in the lattice due to the Eu addition.

To gain a better understanding of differences caused by the introduction of europium in PL results and the variations

Fig. 8 DOS of **a**) p-ZnS and **b**) d-ZnS models
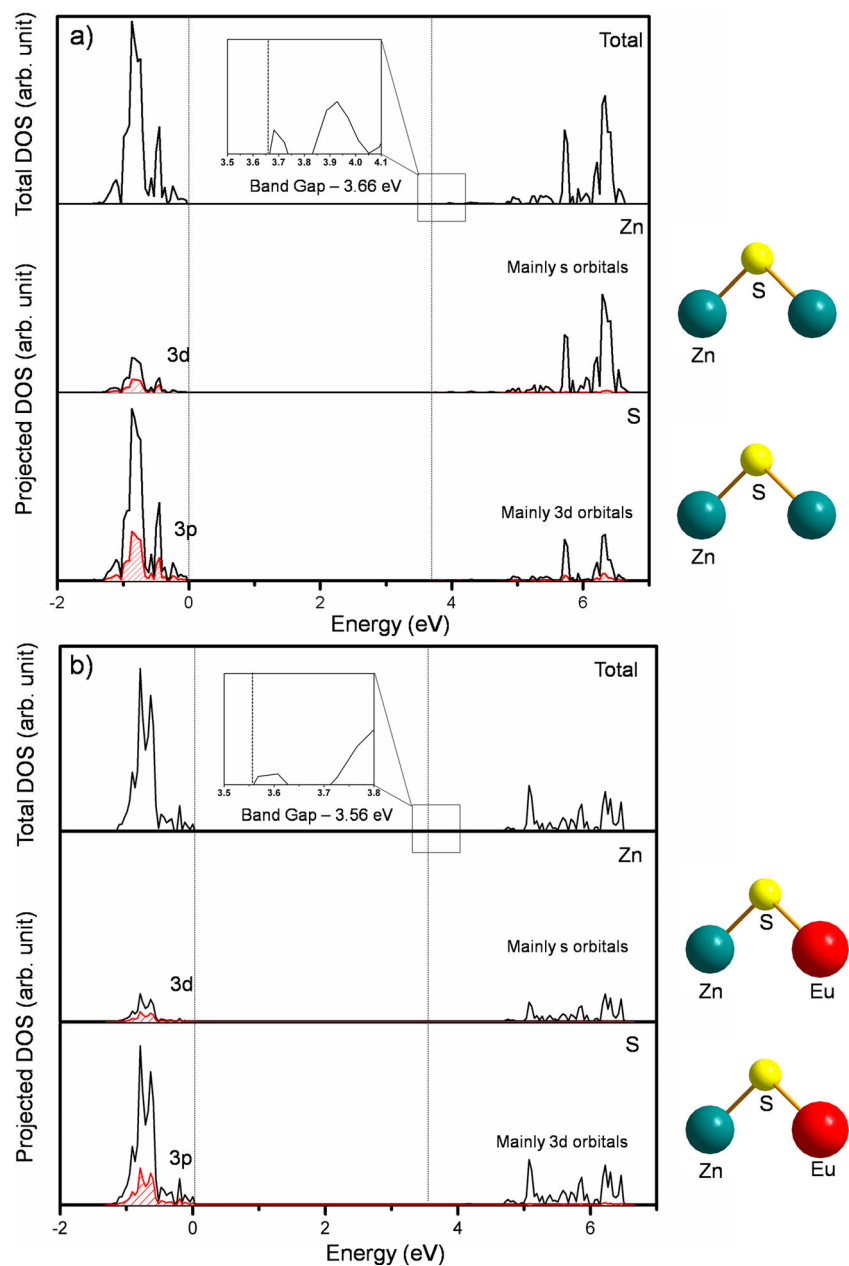
observed in the atomic orbitals, theoretical models of pure ZnS (p-ZnS) and doped ZnS (d-ZnS) were made. The doped models are not an exact replication of all modifications caused by the dopant in the lattice. The symmetry was maintained in both instances and the system d-ZnS has 3.125 % of europium.

Simulation results of band structure (Fig. 7) indicate a direct band gap at the Γ point in both models. The band gap values of p-ZnS and d-ZnS were 3.66 eV and 3.56 eV, respectively. Although there are limitations in simulating the experimental system, the theoretical and experimental results show the same behavior, i.e., the band gap decreases from pure to doped system.

Figure 8 shows the density of states (DOS) of p-ZnS and d-ZnS models

The DOS is very useful to verify different transition levels locations and band compositions. Comparing the total DOS (see Fig. 8a and b), the addition of 3.125 % of Eu^{3+} in the lattice generated a considerable modification of the profile.

An analysis of the projected DOS in both cases (p-ZnS and d-ZnS) for Zn atoms, indicates that the valence band (VB) consists mainly of 3d ($3d_{x-y}$, $3d_{x-z}$, $3d_{y-z}$, $3d_{x^2-y^2}$, and $3d_{z^2}$) levels with a minor contribution of 3p ($3p_x$, $3p_y$, and $3p_z$). The ionic characteristic of the ZnS causes the oxidation state of Zn to remain near to 2+. The conduction band (CB) of the Zn (greatest contribution of the CB of the total DOS) comes mainly from the "s" orbitals. The DOS of the S atoms show that VB is composed mainly from $3p_x$, $3p_y$, and $3p_z$ orbitals while the CB is derived mainly from "d" levels. Quantum-mechanical calculations for d-ZnS indicate that localized states generated in the band gap reduce the gap energies. These findings corroborate with the experimental evidence of the incorporation of Eu^{3+} in the lattice. The characteristic energy structure of the nanoparticles can explain why the energy transfer from nanosized ZnS host to Eu^{3+} ions is so efficient. This mixing transforms the forbidden transitions of

Eu^{3+} ions to allowed transitions, which results in broadening of the transition peaks of Eu^{3+} activators in ZnS nanoparticles. Another benefit of the mixing is an enhanced energy transfer rate to the *d-f* electronic levels of Eu^{3+}.

A correlation can be made between the involved orbitals and PL results. According to the wide band model [47, 48] there are three necessary steps: excitation, recombination, and emission. The first step consists basically of the absorption of energy, corresponding mainly to the transition from "S 3p" orbitals states at the valence up to "Zn 4s" orbitals states inside the forbidden band gap. After excitation, there are recombination processes that occur among the excited states closer to the CB. Finally, there is emission due to the return of the electron to the ground state.

To verify the polarization created by the introduction of dopant in the system, Fig. 9 shows a charge density map of a sulfur layer near to the position where the europium was added:

As a reminder, the computational model considers the pure system as a perfect crystal, with no defects. According to the simulation, all Zn atoms have the same charge and all S atoms have the opposite charge, and thus there is no polarization. For this reason the sulfur layer (see Fig. 8a) has the same pattern. However, the equality of the charge is modified when europium is present in the structure. The introduction of the impurity in the lattice changes the charges of Zn and S atoms as an approximation for the europium atom. Figure 8b shows that there is a visual modification in the sulfur layer in the europium region only; i.e., this impurity generates a polarization in the lattice which is responsible for modifications in the DOS. This structure generates greater local imbalanced charges and the formation of static electrons and holes in the lattice. Noticeably, the polarizations around this new cluster coordination change the structural configurations around europium atoms.
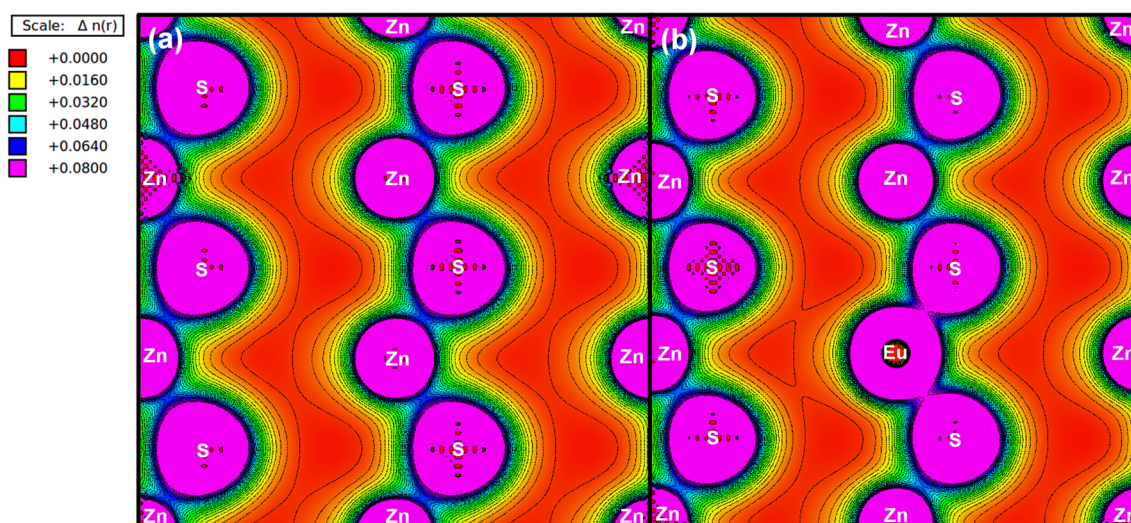
Fig. 9 Electron density maps of **a**) p-ZnS and **b**) d-ZnS models

New localized states generated by the addition of Eu^{3+} in the forbidden band gap region increase the probability of fewer energy transitions which causes a red shift in the PL bands.

Conclusions

In summary, the MAH method has shown itself very efficient and facile to the synthesis of ZnS and ZnS:Eu. Structural analyses were conducted through XRD and FE-SEM. To complement experimental results, a quantum-chemical modeling was made based on the DFT and periodic supercell models in order to evaluate the symmetry of the system. The chemical analysis (ICP-AES) indicated a Eu^{3+} saturation in percentages up to 2.8 %.

In this work, experimental results showed that the addition of Eu^{3+} in the cubic ZnS lattice causes disorder in the structure and the modification of the optical properties.

To complement the studies of the change modifications by the dopant, theoretical studies showed the addition of Eu^{3+} in Zn position causes a symmetry breaking and a local polarization in the structure. The difference of the simulated band gap between pure and doped models showed a great similarity with experimental results. Besides that, by means of DOS it was possible to verify the modification of the profile of the electronic levels.

Therefore the red shift in the PL profile according to the dopant amount can be attributed to new intermediate levels in the band gap region, which are generated by structure defects as distortions or vacancies as was confirmed by first-principles calculations.

References

1. Zhang C, Lin J (2012) Defect-related luminescent materials: synthesis, emission properties and applications. Chem Soc Rev 41:7938–7961
2. Liu Y, Tu D, Zhu H, Li R, Luo W, Chen X (2010) A Strategy to achieve efficient dual-mode luminescence of Eu^{3+} in lanthanides doped multifunctional $NaGdF_4$ nanocrystals. Adv Mater 22:3266–3271
3. Blasse G, Grabmaier BC (1994) Luminescence mater. Springer, Berlin
4. Reisfeld RJ, Christian KJ (1977) Lasers and excited states of rare earths. Ber Bunsen Phys Chemie 82:844–844
5. Zhang K, Yu Y, Sun S (2012) Influence of Eu doping on the microstructure and photoluminescence of CdS nanocrystals. Appl Surf Sci 258:7658–7663
6. Sadhu S, Chowdhury PS, Patra A (2007) Understanding the role of particle size on photophysical properties of CdS:Eu^{3+} nanocrystals. J Lumin 126:387–392
7. Wen X, Li M, Wang Y, Zhang J, Fu L, Hao R, Ma Y, Ai X (2008) Colloidal nanoparticles of a europium complex with enhanced luminescent properties. Langmuir 24:6932–6936
8. Silva D, Abreu A, Davolos MR, Rosaly M (2011) Determination of the local site occupancy of Eu^{3+} ions in $ZnAl_2O_4$ nanocrystalline powders. Opt Mater 33:1226–1233
9. Ekambaram S (2005) Effect of host-structure on the charge of europium ion. J Alloy Compd 390:L1–L3
10. Sapra S, Prakash A, Ghangrekar A, Periasamy N, Sarma DD (2005) Emission properties of manganese-doped ZnS nanocrystals. J Phys Chem B 109:1663–1668
11. Biswas S, Kar S (2008) Fabrication of ZnS nanoparticles and nanorods with cubic and hexagonal crystal structures: a simple solvothermal approach. Nanotechnology 19
12. Tran TK, Park W, Tong W, Kyi MM, Wagner BK, Summers CJ (1997) Photoluminescence properties of ZnS epilayers. J Appl Phys 81:2803–2809
13. Ong HC, Chang RPH (2001) Optical constants of wurtzite ZnS thin films determined by spectroscopic ellipsometry. App Phys Lett 79:3612–3614
14. Peng WQ, Qu SC, Cong GW, Wang ZG (2005) Concentration effect of Mn2+ on the photoluminescence of ZnS : Mn nanocrystals. J Cryst Growth 279:454–460
15. Lee SY, Shin YH, Kim Y, Kim S, Ju S (2011) Thermal quenching behavior of emission bands in Eu-doped ZnS nanowires. J Luminescence 131:1336–1339
16. Wang L, Xu X, Yuan X (2010) Preparation and photoluminescent properties of doped nanoparticles of ZnS by solid-state reaction. J Luminescence 130:137–140
17. Ashwini K, Pandurangappa C, Nagabhushana BM (2012) Synthesis and optical properties of undoped and Eu-doped ZnS nanoparticles. Phys Scripta 85:065706
18. Amaranatha Reddy D, Murali G, Poornaprakash B, Vijayalakshmi RP, Reddy BK (2012) Effect of annea ling temperature on optical and magnetic properties of Cr doped ZnS nanoparticles. Solid State Commun 152:596–602
19. Planelles-Arago J, Julian-Lopez B, Cordoncillo E, Escribano P, Pelle F, Viana B, Sanchez C (2008) Lanthanide doped ZnS quantum dots dispersed in silica glasses: an easy one pot sol–gel synthesis for obtaining novel photonic materials. J Mater Chem 18:5193–5199
20. Thostenson ET, Chou TW (1999) Microwave processing: fundamentals and applications. Compos Part A Appl S 30:1055–1071
21. Komarneni S, Roy R, Li QH (1992) Microwave-hydrothermal synthesis of ceramic powders. Mater Res Bull 27:1393–1405
22. Cavalcante LS, Longo VM, Sczancoski JC, Almeida MAP, Batista AA, Varela JA, Orlandi MO, Longo E, Li MS (2012) Electronic structure, growth mechanism and photoluminescence of $CaWO_4$ crystals. Cryst Eng Comm 14:853–868
23. Raubach CW, de Santana YVB, Ferrer MM, Longo VM, Varela JA, Avansi W Jr, Buzolin PGC, Sambrano JR, Longo E (2012) Strutural and optical approach of CdS@ZnS core–shell system. Chem Phys Lett 536:96–99
24. de Santana YVB, Raubach CW, Ferrer MM, La Porta F, Sambrano JR, Longo VM, Leite ER, Longo E (2011) Experimental and theoretical studies on the enhanced photoluminescence activity of zinc sulfide with a capping agent. J Appl Phys 110:123507–123507
25. Ferrer MM, de Santana YVB, Raubach CW, Sambrano JR, Longo E (2013) Experimental and theoretical studies of photoluminescence in ZnS obtained by microwave-assisted solvothermal method. Curr Phys Chem 3:413–418
26. La Porta FA, Ferrer MM, de Santana YVB, Raubach CW, Longo VM, Sambrano JR, Longo E, Andrés J, Li MS, Varela JA (2013)

Synthesis of wurtzite ZnS nanoparticles using the microwave assisted solvothermal method. J Alloy Compd 556:153–159

27. Becke AD (1993) Density-functional thermochemistry.3. the role of exact exchange. J Chem Phys 98:5648–5652

28. Lee C, Yang W, Parr RG (1988) Development of the colle-salvetti correlation-energy formula into a functional of the electron density. Phys Rev B 37:785–789

29. Dovesi RS, Saunders VR, Roetti C, Orlando R, Zicovich-Wilson CM, Pascale F, Civalleri B, Doll K, Harrison NM, Bush IJ, D'Arco P, Llunell M (2009) Crystal09 user's manual. University of Torino, Torino

30. Marana NL, Longo VM, Longo E, Martins JBL, Sambrano JR (2008) Electronic and structural properties of the (10(1)over-bar0) and (11(2)over-bar0) ZnO surfaces. J Phys Chem A 112:8958–8963

31. Moreira ML, Buzolin PGC, Longo VM, Nicoleti NH, Sambrano JR, Li MS, Varela JA, longo e joint experimental and theoretical analysis of order disorder effects in cubic BaZrO(3) assembled nanoparticles under decaoctahedral shape. J. Phys. Chem. A 115:4482–4490

32. Sambrano JR, Longo VM, Longo E, Taft CA (2007) Electronic and structural properties of the (001) $SrZrO_3$ surface. J Mol Struct (THEOCHEM) 813:49–56

33. Sambrano JR, Nóbrega GF, Taft CA, Andrés J, Beltrán A (2005) A theoretical analysis of the TiO_2/Sn doped (1 1 0) surface properties. Surf Sci 580:71–79

34. Jaffe JE, Hess AC (1993) Hartree-fock study of phase changes in ZnO at high pressure. Phys Rev B 48:7903–7909

35. Lichanot A, Aprà E, Dovesi R (1993) Quantum Mechnical Hartree-Fock Study of the Elastic Properties of Li_2S and Na_2S. Phys Status Solidi B 177:157–163

36. Hay PJ, Wadt WR (1985) Ab initio effective core potentials for molecular calculations potentials for the transition metal atoms Sc to Hg. J Chem Phys 82:270–283

37. Durand P, Barthelat JC (1975) A theoretical method to determine atomic pseudopotentials for electronic structure calculations of molecules and solids. Theoret Chim Acta 38:283–302

38. Eick HA, Baenziger NC, Eyring L (1956) The preparation, crystal structure and some properties of SmN, EuN and YbN1. J Am Chem Soc 78:5987–5989

39. Eick HA, Baenziger NC, Eyring L (1956) Lower oxides of samarium and europium. the preparation and crystal structure of $SmO_{0.4-0.6}$, SmO and EuO_1. J Am Chem Soc 78:5147–5149

40. Yeh CY, Lu ZW, Froyen S, Zunger A (1992) Zinc-blende-wurtzite polytypism in semiconductors. Phys Rev B 46:10086–10097

41. Klug HP, Alexander LA (1962) X-ray diffraction procedures. Wiley, New York

42. Wood DL, Tauc J (1972) Weak absorption tails in amorphous semiconductors, Phys. Rev. B 5:3144-&

43. Cavalcante LS, Sczancoski JC, Li MS, Longo E, Varela JA (2012) β-$ZnMoO4$ microcrystals synthesized by the surfactant-assisted hydrothermal method: growth process and photoluminescence properties. Coll Surf A: Phys Eng Asp 396:346–351

44. Cavalcante LS, Almeida MAP, Avansi W, Tranquilin RL, Longo E, Batista NC, Mastelaro VR, Li MS (2012) Cluster coordination and photoluminescence properties of α-Ag_2WO_4 microcrystals. Inorg Chem 51:10675–10687

45. Moreira ML, Longo VM, Avansi W, Ferrer MM, Andrés J, Mastelaro VR, Varela JA, Longo E (2012) Quantum mechanics insight into the microwave nucleation of SrTiO3 nanospheres. J Phys Chem C 116:24792–24808

46. Willardson RK, Goering HL (1962) Compound semiconductors. Reinhold, New York

47. Longo VM, Cavalcante LS, de Figueiredo AT, Santos LPS, Longo E, Varela JA, Sambrano JR, Paskocimas CA, De Vicente FS, Hernandes AC (2007) Highly intense violet-blue light emission at room temperature in structurally disordered SrZrO(3) powders. Appl Phys Lett 90

48. Moreira ML, Paris EC, do Nascimento GS, Longo VM, Sambrano JR, Mastelaro VR, Bernardi MIB, Andres J, Varela JA, Longo E (2009) Structural and optical properties of CaTiO(3) perovskite-based materials obtained by microwave-assisted hydrothermal synthesis: an experimental and theoretical insight. Acta Mater 57:5174–5185

2.2 – Structural and electronic analysis of the atomic scale nucleation of Ag on α-Ag$_2$WO$_4$ induced by electron irradiation

SCIENTIFIC REPORTS

Structural and electronic analysis of the atomic scale nucleation of Ag on α-Ag$_2$WO$_4$ induced by electron irradiation

Juan Andrés[1], Lourdes Gracia[1,2], Patricio Gonzalez-Navarrete[1,2], Valeria M. Longo[3], Waldir Avansi, Jr.[4], Diogo P. Volanti[5], Mateus M. Ferrer[4], Pablo S. Lemos[4], Felipe A. La Porta[2], Antonio C. Hernandes[3] & Elson Longo[2]

[1]Departament de Química Física i Analítica, UJI−Universitat Jaume I, Av. de Vicent Sos Baynat, s/n, Castelló de la Plana 12071, Spain, [2]Instituto de Química, UNESP−Universidade Estadual Paulista, R. Francisco Degni, 55, Araraquara 14800-900, Brazil, [3]Instituto de Física de São Carlos, USP−Universidade de São Paulo, Av. Trabalhador são-carlense, São Carlos 13560-970, Brazil, [4]Departamento de Física, UFSCar−Universidade Federal de São Carlos, Rod. Washington Luis, km 235, São Carlos 13565-905, Brazil, [5]Departamento de Química e Ciências Ambientais, UNESP−Universidade Estadual Paulista, R. Cristóvão Colombo, 2265, São José do Rio Preto 15054-000, Brazil.

In this work, we utilise a combination of theory, computation and experiments to understand the early events related to the nucleation of Ag filaments on α-Ag$_2$WO$_4$ crystals, which is driven by an accelerated electron beam from an electron microscope under high *vacuum*. The growth process and the chemical composition and elemental distribution in these filaments were analysed in depth at the nanoscale level using TEM, HAADF, EDS and XPS; the structural and electronic aspects were systematically studied in using first-principles electronic structure theory within QTAIM framework. The Ag nucleation and formation on α-Ag$_2$WO$_4$ is a result of the order/disorder effects generated in the crystal by the electron-beam irradiation. Both experimental and theoretical results show that this behavior is associated with structural and electronic changes of the [AgO$_2$] and [AgO$_4$] clusters and, to a minor extent, to the [WO$_6$] cluster; these clusters collectively represent the constituent building blocks of α-Ag$_2$WO$_4$.

T
ungstates of transition metals are ternary oxide semiconductors that contain a combination of covalent, ionic and metallic bonding. They have attracted considerable attention due to their unique symmetry-dependent and spontaneous polarization properties, which are technologically important in numerous applications, such as ferroelasticity, ionic conductivity and photoluminescence[1–4]. They show, in the range of a few nanometers, a surprising tendency to evolve into ordered structures of highly sophisticated architectures. Understanding the structural and electronic properties of the materials in these systems is critical to determining their physical/chemical properties and performance.

Ag$_2$WO$_4$ is a member of the tungstate family that crystallizes in an orthorhombic structure (α-Ag$_2$WO$_4$) with a space group of *Pn2n*. α-Ag$_2$WO$_4$ has been the focus of investigations by our group; we have synthesised this material using different methods (coprecipitation, sonochemistry and hydrothermal synthesis) and have studied its photoluminescence (PL) properties[5]. More recently, the formation of Ag filaments on α-Ag$_2$WO$_4$ crystal, via irradiation of electrons by an accelerated electron beam from an electron microscope under high *vacuum*, was reported[6], and the corresponding potential applications[7] were investigated. Our current investigation is motivated by our incomplete understanding of the underlying fundamental phenomena and mechanisms driving the nucleation and growth of Ag filaments.

While the concept of a crystalline solid as a perfect, periodic structure is at the core of our understanding of a wide range of material properties, in reality, disorder is ubiquitous and is capable of drastically influencing various properties[8]. α-Ag$_2$WO$_4$ is expected to exhibit interesting forms of structural and electronic disorder that play a central role in driving function. α-Ag$_2$WO$_4$ represents a class of inorganic compounds that exhibit unmatched structural versatility and unique intrinsic properties due to the fundamental characteristics of the interactions between its octahedral WO$_6$ and [AgO$_x$] (x = 2, 4, 6, and 7) clusters, which are its basic building blocks. These

clusters are excellent candidates to study to explore the nature of the chemical bond and the influence of the so-called finite-size effects on the physical and electronic structures of such compounds.

Our emphasis is on highlighting how the structural and electronic disorder lead to interesting and unusual physical/chemical properties in this long-established class of materials. First, because this structure exhibits different types of coordination $[AgO_x]$ and because its synergistic coordination mode facilitates the formation of several types of clusters with low and high coordination numbers, the nature of the $[WO_6]$ and $[AgO_x]$ clusters and the interactions between them are inherently predisposed to the formation of flexible materials with open structures. Second, the O-Ag-O and O-W-O bonds in the clusters, which have a weak interaction between the basic units, may also be chemically modified using electron irradiation, as will be shown. Consequently, the stability of the lattice is dependent on the local bonding, and the enthalpic difference between the crystalline and amorphous forms may be very small because the local bonding arrangements are similar in both. This behavior is well established in the study of conventional glass-forming materials, and the network topology and connectivity play a critical role in stabilizing disordered states[5]. Thus, not only might these systems be somewhat predisposed to disorder, but this disorder might readily be tuned by exploiting the versatile structural chemistry of this broad family.

The goal of this work is to understand the basis of the early-nucleation and -growth of Ag filaments after the irradiation process. To investigate the *in situ* growth of Ag filaments in the α-AgWO$_4$ crystal, information on the structural and electronic evolution, as defined by the changes in the electron density, was obtained by density functional theory (DFT) calculations using the quantum theory of atoms in molecules (QTAIM). Experimental techniques such as transmission electron microscopy (TEM) with a high-angle annular dark field (HAADF), energy-dispersive X-ray spectroscopy (EDS), and X-ray photoelectron spectroscopy (XPS) were also employed. The results provide a valuable probe into the relationship between atomic-scale structural and electronic perturbations and their macroscopic consequences.

We focus primarily on the structural and electronic properties to answer three central questions: (i) What happens with the excess electron density, simulating the electron beam of TEM, as it approaches the surface and bulk of α–Ag_2WO_4? (ii) How are the electrons distributed in this material, and how does this distribution relate to the structural and electronic evolution? (iii) Can QTAIM properties provide insight into the strength of the bonds after electron irradiation of α–Ag_2WO_4? We studied the geometric and electronic structure of α-Ag$_2$WO$_4$ and derived a mechanism for the early events in the formation and growth of Ag filaments in the scenario of electron irradiation of $[AgO_x]$ (x = 2, 4, 6, and 7) and $[WO_6]$ clusters, which are the constituent polyhedra of α-Ag$_2$WO$_4$. We shall discuss how the analysis, provided by both the experimental and theoretical results, of the physical and electronic structure of α-Ag$_2$WO$_4$ allows us to explain the Ag-nucleation process. The discussion will address the details of image acquisition and analysis and will provide a guide to interpret the experimental results. All technical details are provided in the Supplementary Information (SI).

Results

A graphical representation of α-Ag$_2$WO$_4$ using polyhedra is presented in Fig. S1 (SI) to show $[WO_6]$ and $[AgO_x]$ (x = 2, 4, 6 and 7) as the building blocks of this material. The crystallographic structural characteristics of the as-prepared products investigated by XRD analysis are also presented in the Supplementary Information (Fig. S2). All of the diffraction peaks of the samples reflect an orthorhombic structure without any deleterious phases and with a space group of *Pn2n* and a point-group symmetry of C$_{2v}$[9,10]; these results are in agreement with the standard values listed in the Inorganic Crystal

Structure Database (ICSD) no. 4165[10] and with those reported in the literature[5,11]. Optimised lattice parameters and atomic positions are listed in Table S1 (SI).

The first step is the growth of metallic Ag on the α-Ag$_2$WO$_4$ crystal; this part of the process is accompanied by *in situ* TEM. A detailed characterisation of the chemical reactions and physical interactions involving nanomaterials requires simultaneous measurement of atomic structure and chemical composition at the nanoscale level. However, the ability to observe the formation and growth of a crystal in real time is reshaping our understanding of these molecular processes, revealing subtleties previously hidden in ensemble averages. *In situ* TEM is an elegant method for uncovering the dynamic processes in the growth of nanocrystals[12]. These recent technological advancements in conjunction with high-resolution imaging provide a new opportunity to view nanoscale processes and nanocrystal growth by aggregation and coalescence has been directly observed in real time by *in situ* TEM studies[12–21]. The injection of electrons can also be used to modify the properties of different materials[16,22–25]; for example, the localised electron probes used in TEM can be used to foster electron-induced processes on a nanometre or subnanometre scale[26–32].

TEM provides a foundation for such atomic resolution studies and is an appropriate tool for monitoring nanoparticle growth in real time[12,18,33–36]. This *in situ* imaging allows the study of materials processes and biological, multistage reactions[12,14,37–40]. However, the studies to date have typically been performed on samples in solution, and the environment around nanoparticles is known to change their physical and chemical properties. The formation and growth conditions of nanoparticles in solution differ markedly from those of nanoparticles in a high-vacuum environment because the surface of nanoparticles adapts to its environment. This difference has been demonstrated using *in situ* spectroscopy and microscopy techniques[12,39,41–53].

In a recent study[6], we observed the growth of Ag on the α-Ag$_2$WO$_4$ structure. In the early steps of the process, the structure of α-Ag$_2$WO$_4$ was clean and smooth (Fig. 1a); a broader view of the same sample is shown in Fig. 1b. With a longer exposure (on the order of a fraction of a second) of electron irradiation, the nucleation process of several Ag nanoparticles occurred throughout the bulk structure (Fig. 1c). A greater density of Ag was observed at the end of the matrix structure, which resulted in the nucleation and growth of a thicker filament (Fig. 1d) that grew further, as shown in Figs. 1e and 1f.

A detailed EDS analysis was performed to elucidate the composition of the nanostructures. Fig. 2a presents a HAADF image of a single nanostructure on which elemental EDS analysis was performed. This structure contains nanofilaments whose growth was stimulated by the electron-beam irradiation on the α-Ag$_2$WO$_4$ surface[6]. The EDS analyses performed on regions 1 to 4 confirmed that the filaments were mainly composed of Ag (Fig. 2b). However, in the nanostructure, mainly Ag, W, and O and mainly W and O were clearly identified in regions 3 and 4, respectively. A small amount of Cu atoms was also observed, which is related to the grid.

XPS measurements were performed on the irradiated and non-irradiated α-Ag$_2$WO$_4$ materials to compare the purity of the surface and the degree of oxidation, to gain insight into the shape evolution, and to unravel the formation mechanism of the samples. The wide-range spectrum is shown in Fig. 3. The results show the presence of a large amount of carbon, and the peaks of Ag, W, and O are clearly visible, indicating that the samples were highly pure. The core-level binding energies (BEs) of O 1 s, Ag 3 d, and W 4f, which have been corrected for the surface charging effect, were determined from the respective XPS spectra and are presented in Table S2 (SI). These results are consistent with the BE values reported in the literature[54,55].

High-resolution C 1 s, O 1 s, Ag 3 d, and W 4f XPS spectra of the as-synthesised and irradiated samples are included for comparison purposes (see Figs. S3 (a–d) (SI) and Table S3 (SI)). An analysis of the
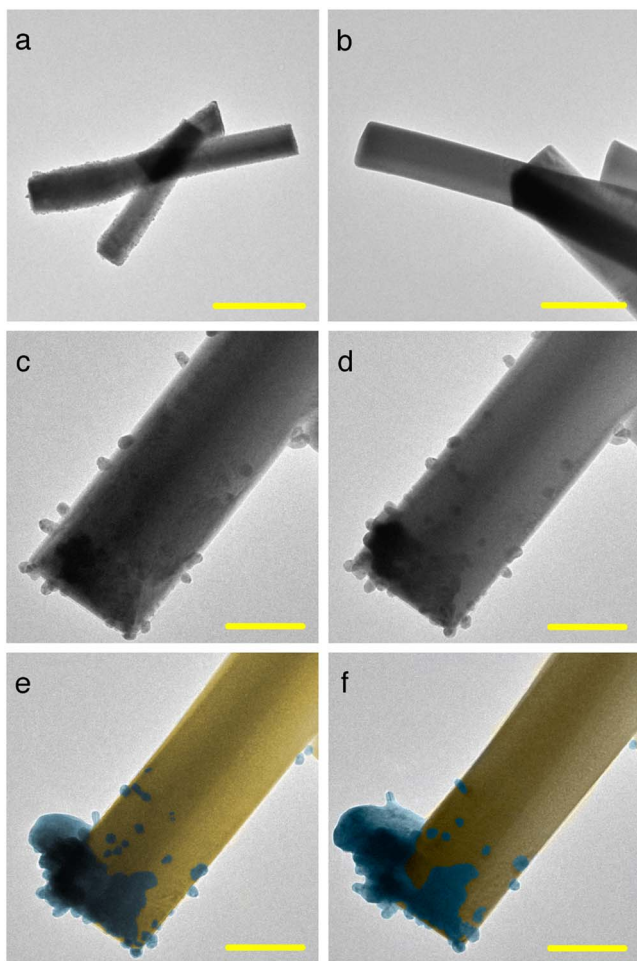
Figure 1 | TEM images of the formation of Ag filaments from the a-Ag₂WO₄ bulk. (a) and (b) TEM images obtained at different magnifications indicate a smooth and clear surface. (c)–(f) Thick Ag filaments grow at the edge of the sample, whereas other Ag nanoparticles are absorbed by the matrix. (Scale bar = 500 nm in a, 200 nm in b and, 100 nm in (c–f).

Figure 2 | (a) HAADF image of an isolated nanostructure. (b) EDS performed in different regions, which are illustrated in Fig. 2a. (Scale bar = 50 nm in a).
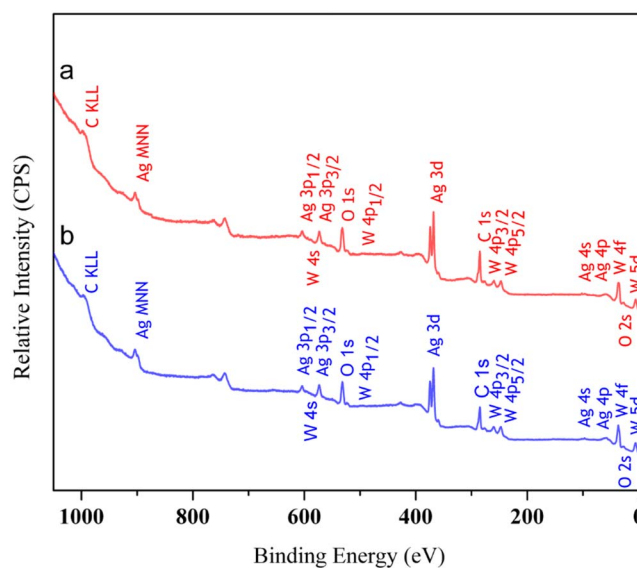
Figure 3 | XPS survey spectrum of the irradiated in (a), and non-irradiated a-Ag₂WO₄ material in (b).

XPS results shows a strong effect on both the Ag and W atoms. The irradiated sample has a larger amount of W$^{(V)}$, which indicates greater disorder of the structure, in accordance with previous HRTEM results. The Ag $3d_{5/2}$ peak is identified at 368.10 and 367.80 eV in the spectra of the as-synthesised and irradiated samples, respectively, which suggests the presence of metallic Ag[56,57]. To confirm the presence of metallic Ag from the XPS data, the asymmetric peaks observed in the Ag $3d_{5/2}$ core-level region and the Auger $M_4N_{45}N_{45}$ peaks of α-Ag₂WO₄ and of irradiated α-Ag₂WO₄ were analysed (see Fig. S4 (SI)).

Our findings confirm the presence of metallic Ag, and the corresponding results agree with the results reported in the *Handbook of Monochromatic XPS Spectra*[58]. a The XPS spectra are also very similar to the spectrum of Ag $M_4N_{45}N_{45}$ of α-Ag₂WO₄ published by Ho et al[55]. These results represent a valuable contribution to the XPS analysis of the *in situ* atomic-scale nucleation of Ag filaments on α-Ag₂WO₄.

Because the formation of metallic Ag after the electron irradiation of α-Ag₂WO₄ is a quantum phenomenon, we performed quantum mechanical calculations to understand the structural and electronic modifications of α-Ag₂WO₄ that were observed experimentally. In the calculations, electrons were introduced one by one up to ten in the orthorhombic unit cell of α-Ag₂WO₄, and a redistribution of these extra electrons takes place by means of a simultaneously

geometry optimization on both the lattice parameters and the atomic positions. The change of lattice constants (a, b, and c) as a function of the number of added electrons are presented in Fig. S5 (SI). In Fig. 4a, the values of the bond distances of Ag-O and W-O in [AgO₂], [AgO₄], and [WO₆] clusters are shown as a function of electrons added. An analysis and a comparison of the geometries for a neutral (N = 0) and charged (N = 10) structures show a pronounced increase in the corresponding Ag-O distances with the addition of electrons. In the [AgO₂] cluster, the Ag-O distance increases from 2.15 to 2.75 Å (in blue). In the [AgO₄] cluster, two different distances are observed: one pair (in red) exhibits behaviour similar to that of the bonds in the [AgO₂] cluster and has an O-Ag-O angle of approximately 170°; the other pair (in garnet) has an O-Ag-O angle of approximately 108° and a longer Ag-O distance, which indicates that the atoms detach as the electrons are added. In fact, when N = 10, the first pair of O atoms forms an O-Ag-O angle of approximately 178°, whereas the angle of the second pair is reduced to approximately 90°, as shown in Fig. 4b. In the two types of [WO₆] clusters, we find that the W-O distances corresponding to the W2 and W3 atoms remain almost unaltered, whereas the distance of the W-O bond corresponding to W1 decreases smoothly with the addition of electrons. These results show that during electron irradiation, electronic and structural disorder was introduced into the material, thus illustrating the fundamental role of cluster concepts in the formation and growth of Ag filaments.

QTAIM, which was developed by Bader and collaborators[59–61], allows the analysis of the experimental and theoretical electron density distributions, ρ(r), in a molecule or solid as well as the study of the properties of ρ(r); these analyses reveal the bonding interactions in a molecular or crystal system and the nature of these interactions. The electronic charge of each atom is evaluated using Bader charge analysis within the QTAIM framework, which is a way of dividing molecules or solids into atoms on the basis of electronic charge density. Finding zero flux surfaces between two atoms allows the charge of each atom to be calculated. In Fig. 5, the charge density of the Ag and W centres of the [AgO₂], [AgO₄], and [WO₆] clusters is depicted as a function of the number of electrons added. Atomic charges were calculated using integrations of the charge density

within the atomic basins, Ω, and subtracting the nuclear charge, Z, of the corresponding atom.

$$q(\Omega) = Z_{\Omega} - N(\Omega) \text{ with } N(\Omega) = \int_{\Omega} \rho(\Omega) dr \qquad (1)$$

The average bond distances of Ag-Ag as a function of the number of electrons added are presented in Fig. 5a, and electron density contours on the (100) plane for the neutral (N = 0) structure and charged (N = 10) structures are depicted in Fig. 5b. Isodensity lines less than 0.02 a.u. are coloured white to highlight the differences between them. An analysis of the results presented in Fig. 5b reveals that the electron density distribution is enhanced between Ag4 and Ag5 at the same time that the Ag4–Ag5 contact distance is shortened when the number of added electrons is increased from N = 0 to N = 10. In addition, there is an electronic charge density enlargement in the vicinity of Ag6 atoms on going from N = 0 to N = 10.

An analysis of the results presented in Fig. 5c reveals that the Ag6 atoms of the [AgO₂] clusters are the atoms most prone to reduction. At N = 7, the Ag6 atoms are practically reduced, whereas the Ag4/Ag5 centres require at least 10 electrons to reach the same state. This behaviour implies the existence of two different paths to obtaining metallic Ag, which are associated with the [AgO₂] and [AgO₄] clusters. In the case of W atoms that form [WO₆] clusters, W1 atoms behave differently than W2 and W3 atoms, and a minor decrease in electron density relative to that of Ag centres is observed (a decrease of 0.2 units at N = 10). Therefore, the extra electron density added to the material is transferred from one cluster to another through the lattice network, and the Ag-formation process involves both adjacent [AgO₂] and [AgO₄] clusters and, to a minor extent, [WO₆] clusters. During electron irradiation, electronic and structural disorder is introduced into the material, indicating the fundamental role that cluster concepts play in the formation and growth of Ag filaments.

The results of the calculations of the Laplacian, $\nabla^2 \rho_{bcp}$, and the charge density, ρ_{bcp}, at the (3,−1) bond critical points (BCP) in Ag-O bonds in the [AgO₂] and [AgO₄] clusters are shown in Table 1. The effect of adding electrons to the material produces striking differences in the values of the Laplacian and the charge density at the (3,−1) BCP. Notably, the Laplacian and charge density values of the
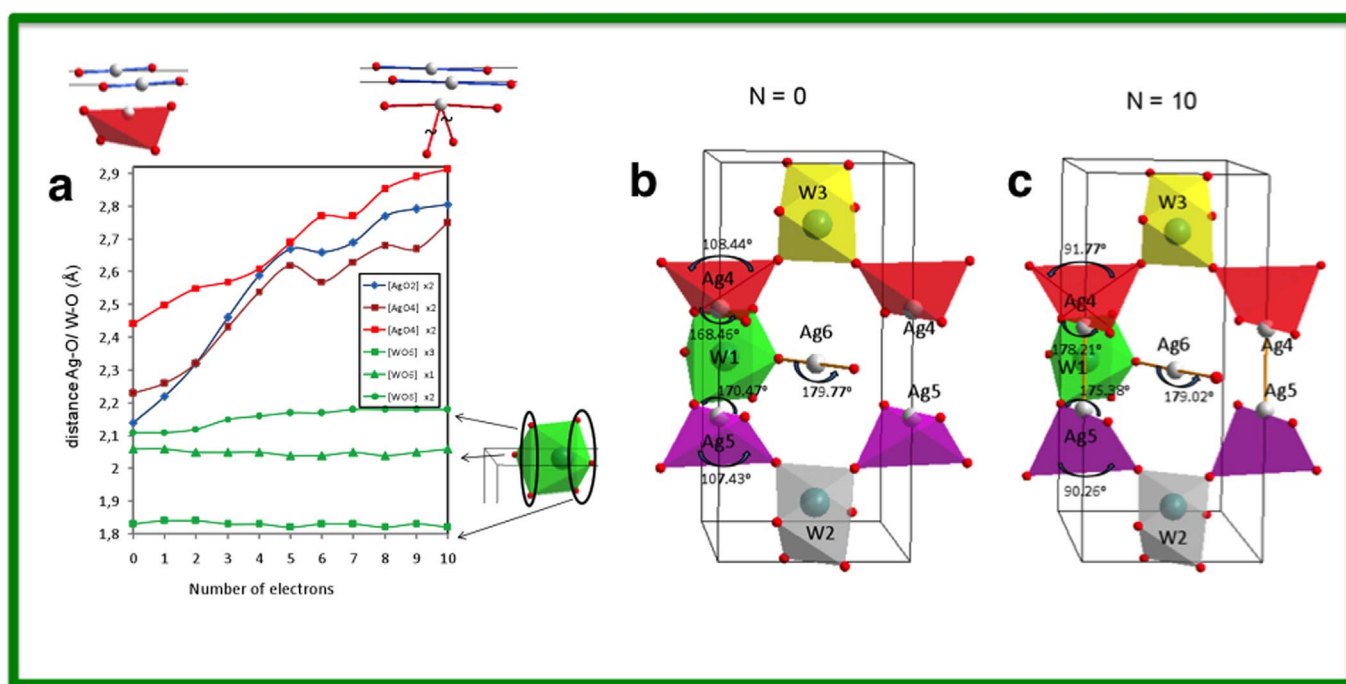
Figure 4 | (a) Values of Ag-O and W-O bond distances in the [AgO₂], [AgO₄], and [WO₆] clusters as a function of the number of electrons added. (b) Geometry of neutral (N = 0) and charged (N = 10) structures.
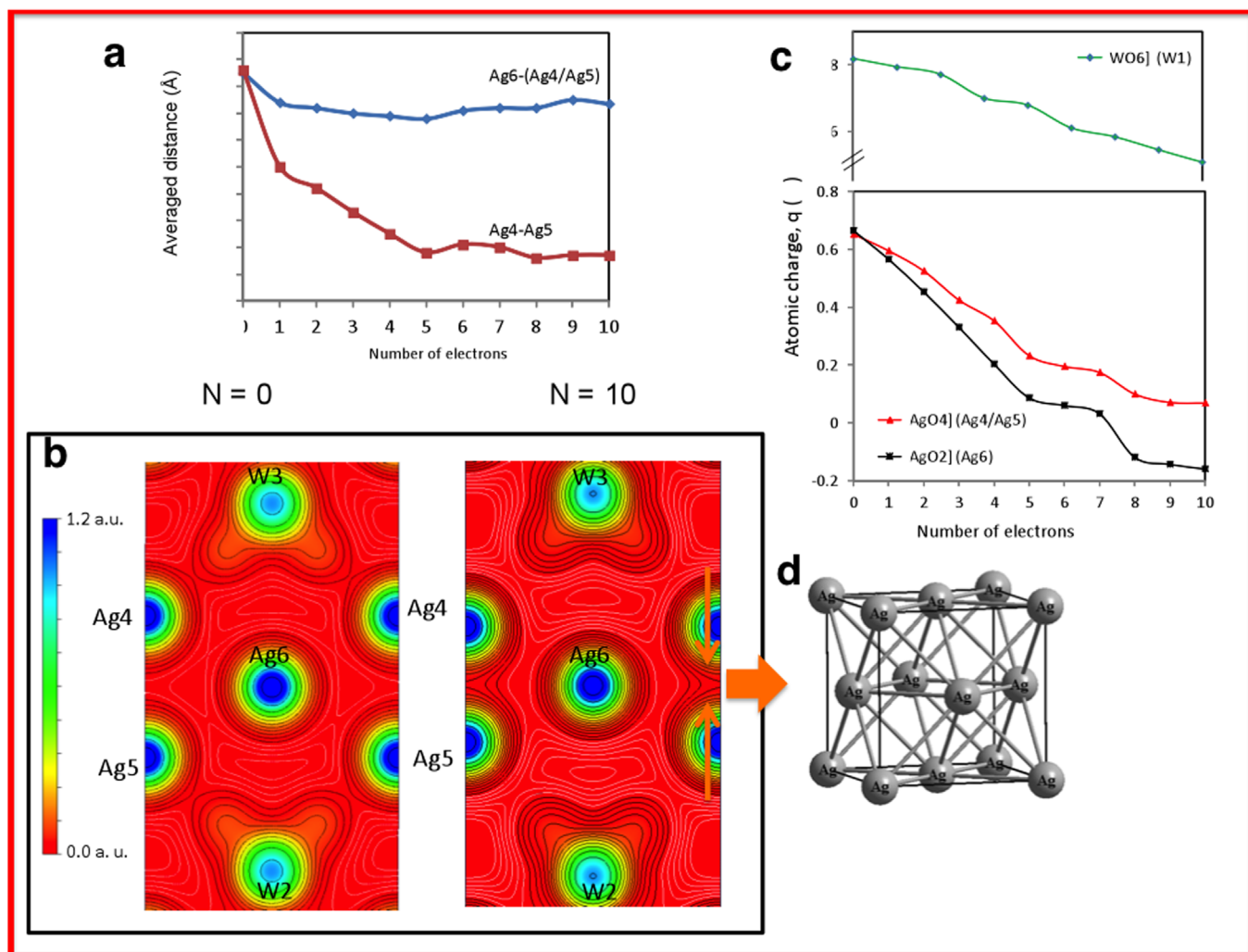
Figure 5 | (a) Average Ag-Ag distances as a function of the number of electrons added. (b) Electron density contours on the (100) plane for a neutral (N = 0) structure and a charged (N = 10) structure. Isodensity lines less than 0.02 a.u. are coloured white. (c) Charge density of the Ag and W centres in $[AgO_2]$, $[AgO_4]$, and $[WO_6]$ clusters as a function of the number of electrons added. q(Ω) represents the number of valence electrons minus the calculated charge density. (d) Structure of metallic Ag.

Ag-O bonds decrease considerably as electrons are added, which indicates that these bonds become weaker in favour of the formation of metallic Ag from both the $[AgO_2]$ and $[AgO_4]$ clusters.

Finally, we have calculated the total and projected density of states (DOS) on atoms and orbitals in order to complement the Bader charge analysis. For neutral Ag_2WO_4 (N = 0), there is essentially no visible difference in orbital character between PBE and PBE + U, however up to U = 6, the band gap values are maintained nearly constant to 2.0 eV which conveys the most satisfactory picture for both the occupied and unoccupied states. The DOS plots depicted in Fig. S6 (SI) are focused on the upper part of the valence band (VB) and the lower part of the conduction band (CB) for different Ag atoms as the number of electrons is added, for N = 0, 2, 4 and 8. For the DOS evaluation, from a total of 16 Ag atoms in the unit cell, three different types of Ag atoms have been classified according to previous results of the electron density distribution: "Ag1/2/3" (10 atoms), "Ag4/5" (4 atoms) and "Ag6" (2 atoms). An analysis of the plots shows a 50% of reduction of the band gap energy for N = 2, with a high contribution of s orbitals in the lower part of CB from Ag4/5 and Ag6. When the number of electrons is increased to 3 and up to 8 the system becomes a conductor. For N = 4 and N = 8 the DOS images have been also depicted in Fig. S6, highlighting the same contribution around 0.0 eV for N = 4 and in the energy range −1.5–1.0 eV for N = 8. It is worth noting that the Fermi level is

placed at energy of 0 eV. Therefore, a shift of the s band (and the d band as a minor contribution) of Ag4/5 and Ag6 atoms is possibly induced by the interaction of the sample with the electron beam, and

Table 1 | Laplacian and charge density at the (3,−1) BCPs in Ag-O bonds for $[AgO_2]$ and $[AgO_4]$ clusters as a function of the number of electrons added, N

| | BCP $[AgO_2]$ | | BCP $[AgO_4]$ | | | |
| | Ag-O | | Ag-O1 | | Ag-O2 | |
N	ρ_{bcp}	$\nabla^2\rho_{bcp}$	ρ_{bcp}	$\nabla^2\rho_{bcp}$	ρ_{bcp}	$\nabla^2\rho_{bcp}$
0	0.49	6.80	0.26	3.29	0.42	4.91
1	0.42	4.56	0.23	2.93	0.39	4.35
2	0.34	3.88	0.21	2.67	0.35	3.86
3	0.26	3.10	0.20	2.56	0.28	3.10
4	0.20	2.26	0.19	2.35	0.22	2.56
5	0.17	1.84	0.16	1.96	0.19	2.17
6	0.17	1.76	0.15	1.83	0.19	2.08
7	0.16	1.71	0.13	1.65	0.19	2.12
8	0.14	1.55	0.12	1.39	0.17	1.80
9	0.14	1.47	0.10	1.23	0.17	1.76
10	0.13	1.40	0.10	1.14	0.16	1.51

predicted by XPS analysis. Consequently, a structural rearrangement is caused related to the shortening of the distance Ag4–Ag5 and the Ag-Ag metallic bond formation when the number of added electrons is increased in accordance with the dynamics results measured *in situ* using TEM.

Discussion

Understanding the *in situ* atomic-scale nucleation induced by the electron irradiation of Ag filaments on α-Ag$_2$WO$_4$ can be achieved through a combination of experimental and theoretical analyses. We used experimental techniques (TEM, EDS, and XPS) and first-principle calculations based on the QTAIM framework to study the geometric and electronic structure of α-Ag$_2$WO$_4$. We then derived a mechanism on the basis of the electron irradiation of [AgO$_x$] (x = 2, 4, 6, and 7) and [WO$_6$] clusters, which are the constituent polyhedra of α-Ag$_2$WO$_4$. The mechanism is relevant to the nucleation and growth of Ag filaments that occurs when α-Ag$_2$WO$_4$ is irradiated using an accelerated electron beam from an electron microscope under high vacuum. Our model allows us to better understand the atomic events in this process, and we are currently pursuing this relevant area of investigation. The results of the present work provide an atomic-scale picture of the formation of metallic Ag as well as an initial glimpse into how [WO$_6$] and [AgO$_x$] clusters behave in this material when it is irradiated with electrons from an external source. The strategy reported here for retrospective mapping of the growth of metallic Ag has the potential to yield valuable insights into the mechanistic aspects of the clusters, particularly when the experimental results are considered in conjunction with first-principles calculations.

Our main conclusions are as follows: During the electron irradiation process, electronic and structural disorder is introduced into the material, showing the fundamental role of clusters in the nucleation and growth of Ag filaments. Extra electrons added to the material are transferred from one cluster to another through the lattice network, and Ag formation occurs via the reduction of both [AgO$_2$] and [AgO$_4$] clusters that are adjacent and, to a lesser extent, through the reduction of the [WO$_6$] cluster. These findings provide a valuable probe into the relationship between atomic-scale structural and electronic perturbations and their macroscopic consequences. The broader significance of this work lies in the direct and visually impressive demonstration of the conversion of electron irradiation into structural and electronic order/disorder effects to cause the formation of Ag on α-Ag$_2$WO$_4$. Therefore, the Ag nucleation mechanisms observed here can provide deep insight into the physical and electronic structure of other silver-metal-oxide-based materials under electron irradiation conditions. The present work leads to a unified understanding of the complex behaviour of these materials and opens a new direction for the rational design of materials with exciting properties.

Methods

Experimental details. The α-Ag$_2$WO$_4$ samples were synthesised at 90°C in 1 min by the injection of precursor ions into hot aqueous solutions according to the method reported in our previous work[6]. TEM analysis was performed on a CM200-Philips and JEOL JEM 2100F TEM/STEM microscope operated at 200 kV. Specimens for TEM images were obtained by drying droplets of as-prepared samples from an acetone dispersion that had been sonicated for 10 min and deposited on 300-mesh Cu grids. The chemical analyses of the samples were performed by EDS using a Thermo-Noran EDS attached to the JEM 2100F and equipped with a Si detector.

XPS spectra were collected using a commercial spectrometer (UNI-SPECS-UHV). To analyse the near-surface composition and the chemical environment in the α-Ag$_2$WO$_4$ nanocrystals, the measurements were performed in a small area of each sample using the Mg Kα line (hν = 1253.6 eV); the analyser pass energy was set to 10 eV. In particular, the inelastic background of the C 1 s, O 1 s, W 4f, and Ag 3 d electron core-level spectra and the Auger Ag MNN peak were subtracted using Shirley's method[62]; the BEs were corrected using the hydrocarbon component of adventitious carbon fixed at 285.0 eV.

The X-ray diffraction measurements were performed on a D/Max-2500PC diffractometer (Rigaku, Japan) using Cu Kα radiation (λ = 1.5406 Å) in the 2θ range from 10° to 70° in the normal routine with a scanning velocity of 2°/min and a step of 0.02°.

Calculation details. First-principles total-energy calculations were performed within the periodic DFT framework using the VASP program[63,64]. The Kohn-Sham equations were solved by means of the Perdew, Burke, and Ernzerhof exchange-correlation functional[64], and the electron-ion interaction was described by the projector-augmented-wave pseudopotentials[65,66]. Because of the well-known limitations of standard DFT in describing the electronic structure of "strongly-correlated" compounds, a correction to the PBE wavefunctions was made (PBE + U) by including a repulsive on-site Coulomb interaction, U, according to the formula of Dudarev et al[67]. PBE + U scheme contains the same PBE approximate correlation, but takes into account orbital dependence (applied to the d states of silver) of the Coulomb and exchange interactions. The value of the Hubbard parameter was tested, and a value of U = 6 eV for the Ag element was used. The plane-wave expansion was truncated at a cut-off energy of 400 eV, and the Brillouin zones were sampled through Monkhorst-Pack special k-points grids (6 $\times$ 6 $\times$ 6) that ensure geometrical and energetic convergence for the Ag$_2$WO$_4$ structures considered in this work. The keyword NELECT was used to increase the number of electrons in the bulk structure, and all the crystal structures were optimised simultaneously on both the volume of the unit-cell and the atomic positions. Further information, as well as details of the ab initio quantum chemical calculations, is given in the Supplementary Information.

1. Heyer, O. *et al.* A new multiferroic material: MnWO$_4$. *J. Phys.-Condens. Matter* **18**, L471–L475 (2006).
2. Zhang, L., Lu, C., Wang, Y. & Cheng, Y. Hydrothermal synthesis and characterization of MnWO$_4$ nanoplates and their ionic conductivity. *Mater. Chem. Phys.* **103**, 433–436 (2007).
3. Song, X. C. *et al.* Hydrothermal preparation and photoluminescence of bundle-like structure of ZnWO$_4$ nanorods. *Appl. Phys. A* **94**, 185–188 (2009).
4. Xing, Y. *et al.* Microemulsion-mediated solvothermal synthesis and photoluminescent property of 3D flowerlike MnWO$_4$ micro/nanocomposite structure. *Solid State Sci.* **10**, 1299–1304 (2008).
5. Cavalcante, L. S. *et al.* Cluster Coordination and Photoluminescence Properties of alpha-Ag$_2$WO$_4$ Microcrystals. *Inorg. Chem.* **51**, 10675–10687 (2012).
6. Longo, E. *et al.* Direct in situ observation of the electron-driven synthesis of Ag filaments on alpha-Ag$_2$WO$_4$ crystals. *Sci. Rep.* **3**, 1676 (2013).
7. Longo, E. *et al.* Toward an Understanding of the Growth of Ag Filaments on α-Ag2WO4 and their Photoluminescent Properties: A Combined Experimental and Theoretical Study. *J. Phys. Chem. C* doi:10.1021/jp408167v (2014).
8. Ziman, J. M. *Models of disorder: the theoretical physics of homogeneously disordered systems* (Cambridge University Press, Cambridge Eng.; New York, 1979).
9. Cui, X. J. *et al.* Selective synthesis and characterization of single-crystal silver molybdate/tungstate nanowires by a hydrothermal process. *Chem.-a Eur. J.* **10**, 218–223 (2004).
10. Skarstad, P. M. & Geller, S. (W$_4$O$_{16}$)$^{8-}$ Polyion in High-Temperature Modification of Silver Tungstate. *Mater. Res. Bull.* **10**, 791–799 (1975).
11. Stone, D. *et al.* Layered atomic structures of double oxides for low shear strength at high temperatures. *Scripta Mater.* **62**, 735–738 (2010).
12. Zheng, H. M. *et al.* Observation of Single Colloidal Platinum Nanocrystal Growth Trajectories. *Science* **324**, 1309–1312 (2009).
13. Chai, J., Liao, X., Giam, L. R. & Mirkin, C. A. Nanoreactors for Studying Single Nanoparticle Coarsening. *J. Am. Chem. Soc.* **134**, 158–161 (2012).
14. Evans, J. E., Jungjohann, K. L., Browning, N. D. & Arslan, I. Controlled Growth of Nanoparticles from Solution with In Situ Liquid Transmission Electron Microscopy. *Nano Lett.* **11**, 2809–2813 (2011).
15. Liao, H. G., Cui, L. K., Whitelam, S. & Zheng, H. M. Real-Time Imaging of Pt$_3$Fe Nanorod Growth in Solution. *Science* **336**, 1011–1014 (2012).
16. Papageorgiou, A. C., Pang, C. L., Chen, Q. & Thornton, G. Low-dimensional, reduced phases of ultrathin TiO$_2$. *ACS Nano* **1**, 409–414 (2007).
17. Xin, H. L. L. & Zheng, H. M. In Situ Observation of Oscillatory Growth of Bismuth Nanoparticles. *Nano Lett.* **12**, 1470–1474 (2012).
18. Yuk, J. M. *et al.* High-Resolution EM of Colloidal Nanocrystal Growth Using Graphene Liquid Cells. *Science* **336**, 61–64 (2012).
19. Kraus, T. & de Jonge, N. Dendritic Gold Nanowire Growth Observed in Liquid with Transmission Electron Microscopy. *Langmuir* **29**, 8427–8432 (2013).
20. Sun, M., Liao, H.-G., Niu, K. & Zheng, H. Structural and Morphological Evolution of Lead Dendrites during Electrochemical Migration. *Sci. Rep.* **3**, 3227 (2013).
21. Yuk, J. M. *et al.* In situ atomic imaging of coalescence of Au nanoparticles on graphene: rotation and grain boundary migration. *Chem. Commun.* **49**, 11479–11481 (2013).
22. Hamann, T., Bohler, E. & Swiderek, P. Low-Energy-Electron-Induced Hydroamination of an Alkene. *Angew. Chem.-Int. Edit.* **48**, 4643–4645 (2009).
23. Ramsier, R. D. & Yates, J. T. Electron-Stimulated Desorption - Principles and Applications. *Surf. Sci. Rep.* **12**, 243–378 (1991).
24. Turchanin, A. *et al.* One Nanometer Thin Carbon Nanosheets with Tunable Conductivity and Stiffness. *Adv. Mater.* **21**, 1233–+ (2009).
25. Xu, W. *et al.* In-situ atomic-scale observation of irradiation-induced void formation. *Nat. Commun.* **4**, 2288 (2013).

26. Randolph, S. J., Fowlkes, J. D. & Rack, P. D. Focused, nanoscale electron-beam-induced deposition and etching. *Crit. Rev. Solid State Mat. Sci.* **31**, 55–89 (2006).

27. Utke, I., Hoffmann, P. & Melngailis, J. Gas-assisted focused electron beam and ion beam processing and fabrication. *J. Vac. Sci. Technol. B* **26**, 1197–1276 (2008).

28. van Dorp, W. F. & Hagen, C. W. A critical literature review of focused electron beam induced deposition. *J. Appl. Phys.* **104**, 081301 (2008).

29. van Dorp, W. F., Hagen, C. W., Crozier, P. A. & Kruit, P. Growth behavior near the ultimate resolution of nanometer-scale focused electron beam-induced deposition. *Nanotechnology* **19**, 225305 (2008).

30. van Dorp, W. F., van Someren, B., Hagen, C. W. & Kruit, P. Approaching the resolution limit of nanometer-scale electron beam-induced deposition. *Nano Lett.* **5**, 1303–1307 (2005).

31. van Kouwen, L., Botman, A. & Hagen, C. W. Focused Electron-Beam-Induced Deposition of 3 nm Dots in a Scanning Electron Microscope. *Nano Lett.* **9**, 2149–2152 (2009).

32. Walz, M. M. *et al.* Electrons as "Invisible Ink": Fabrication of Nanostructures by Local Electron Beam Induced Activation of SiOx. *Angew. Chem.-Int. Edit.* **49**, 4669–4673 (2010).

33. Yagi, K., Takayanagi, K., Kobayashi, K. & Honjo, G. Insitu Observations of Growth Processes of Multiply Twinned Particles. *J. Cryst. Growth* **28**, 117–124 (1975).

34. de Jonge, N. & Ross, F. M. Electron microscopy of specimens in liquid. *Nat. Nanotechnol.* **6**, 695–704 (2011).

35. Kim, J. U., Cha, S. H., Shin, K., Jho, J. Y. & Lee, J. C. Synthesis of gold nanoparticles from gold(I)-alkanethiolate complexes with supramolecular structures through electron beam irradiation in TEM. *J. Am. Chem. Soc.* **127**, 9962–9963 (2005).

36. Sohn, J. H. *et al.* Preparation of conducting silver paste with Ag nanoparticles prepared by e-beam irradiation. *Rad. Phys. Chem.* **79**, 1149–1153 (2010).

37. de Jonge, N., Peckys, D. B., Kremers, G. J. & Piston, D. W. Electron microscopy of whole cells in liquid with nanometer resolution. *Proc. Natl. Acad. Sci. U. S. A.* **106**, 2159–2164 (2009).

38. Klein, K. L., Anderson, I. M. & De Jonge, N. Transmission electron microscopy with a liquid flow cell. *J. Microsc.* **242**, 117–123 (2011).

39. Tao, F. & Salmeron, M. In Situ Studies of Chemistry and Structure of Materials in Reactive Environments. *Science* **331**, 171–174 (2011).

40. Williamson, M. J., Tromp, R. M., Vereecken, P. M., Hull, R. & Ross, F. M. Dynamic microscopy of nanoscale cluster growth at the solid-liquid interface. *Nat. Mater.* **2**, 532–536 (2003).

41. Altman, M. S. CO Prefers the Aisle Seat. *Science* **327**, 789–790 (2010).

42. de Smit, E. *et al.* Nanoscale chemical imaging of a working catalyst by scanning transmission X-ray microscopy. *Nature* **456**, 222–U239 (2008).

43. Friebel, D., Miller, D. J., Nordlund, D., Ogasawara, H. & Nilsson, A. Degradation of Bimetallic Model Electrocatalysts: An In Situ X-Ray Absorption Spectroscopy Study. *Angew. Chem.-Int. Edit.* **50**, 10190–10192 (2011).

44. Hansen, P. L. *et al.* Atom-resolved imaging of dynamic shape changes in supported copper nanocrystals. *Science* **295**, 2053–2055 (2002).

45. Ketteler, G. *et al.* In situ spectroscopic study of the oxidation and reduction of Pd(111). *J. Am. Chem. Soc.* **127**, 18269–18273 (2005).

46. Nguyen, L., Cheng, F., Zhang, S. R. & Tao, F. Visualization of Surfaces of Pt and Ni Model Catalysts in Reactive Environments Using Ambient Pressure High Temperature Scanning Tunneling Microscopy and Understanding the Restructurings of Surfaces of Model Metal Catalysts under Reaction Conditions at Near Ambient Pressure. *J. Phys. Chem. C* **117**, 971–977 (2013).

47. Park, J. *et al.* Direct Observation of Nanoparticle Superlattice Formation by Using Liquid Cell Transmission Electron Microscopy. *ACS Nano* **6**, 2078–2085 (2012).

48. Rodriguez, J. A. *et al.* Activity of CeOx and TiOx nanoparticles grown on Au(111) in the water-gas shift reaction. *Science* **318**, 1757–1760 (2007).

49. Tao, F. *et al.* Break-Up of Stepped Platinum Catalyst Surfaces by High CO Coverage. *Science* **327**, 850–853 (2010).

50. Tao, F., Tang, D., Salmeron, M. & Somorjai, G. A. A new scanning tunneling microscope reactor used for high-pressure and high-temperature catalysis studies. *Rev. Sci. Instrum.* **79**, 084101 (2008).

51. Thostrup, P. *et al.* Adsorption-induced step formation. *Phys. Rev. Lett.* **87**, 126102 (2001).

52. Vestergaard, E. K. *et al.* Adsorbate-induced alloy phase separation: A direct view by high-pressure scanning tunneling microscopy. *Phys. Rev. Lett.* **95**, 126101 (2005).

53. Wachs, I. E. & Roberts, C. A. Monitoring surface metal oxide catalytic active sites with Raman spectroscopy. *Chem. Soc. Rev.* **39**, 5002–5017 (2010).

54. Wagner, C. D. W. W., Riggs, W. W., Davis, L. E., Moulder, J. F. & Muilenberg, G. E. *Handbook of X-ray Photoeclectron Spectroscopy* (Physical Electronics Division, Perkin–Elmer Corporation, Wellesley, MA, 1979).

55. Ho, S. F., Contarini, S. & Rabalais, J. W. Ion-Beam-Induced Chemical-Changes in the Oxyanions (CrOYN-, MoOYN-, WOYN-, VOYN-, NbOYN-, and TaOYN-) and Oxides (CrOX, MoOX, WOX, VOX, NbOX, and TaOX). *J. Phys. Chem.* **91**, 4779–4788 (1987).

56. Wang, D., Xue, G., Zhen, Y., Fu, F. & Li, D. Monodispersed Ag nanoparticles loaded on the surface of spherical Bi_2WO_6 nanoarchitectures with enhanced photocatalytic activities. *J. Mater. Chem.* **22**, 4751–4758 (2012).

57. Zhang, L. S. *et al.* AgBr-Ag-Bi_2WO_6 nanojunction system: A novel and efficient photocatalyst with double visible-light active components. *Appl. Catal. A* **363**, 221–229 (2009).

58. Crist, V. *Handbook of Monochromatic XPS spectra. The Elements and Native Oxides.* (John Wiley & Sons Ltd., New York 2000).

59. Bader, R. F. W. *Atoms in molecules: a quantum theory* (Clarendon Press Oxford New York, 1990).

60. Matta, C. F. & Boyd, R. J. *The quantum theory of atoms in molecules* (Wiley-VCH, Weinheim, 2007).

61. Popelier, P. L. A. *Atoms in molecules: an introduction* (Prentice Hall, Harlow, 2000).

62. Shirley, D. A. High-Resolution X-Ray Photoemission Spectrum of Valence Bands of Gold. *Phys. Rev. B* **5**, 4709– (1972).

63. Kresse, G. & Hafner, J. ab-initio Molecular-Dynamics Simulation Of The Liquid-Metal Amorphous-Semiconductor Transition In Germanium. *Phys. Rev. B* **49**, 14251–14269 (1994).

64. Kresse, G. & Furthmuller, J. Efficiency of ab-initio total energy calculations for metals and semiconductors using a plane-wave basis set. *Comput. Mater. Sci.* **6**, 15–50 (1996).

65. Perdew, J. P., Burke, K. & Ernzerhof, M. Generalized gradient approximation made simple. *Phys. Rev. Lett.* **77**, 3865–3868 (1996).

66. Kresse, G. & Joubert, D. From ultrasoft pseudopotentials to the projector augmented-wave method. *Phys. Rev. B* **59**, 1758–1775 (1999).

67. Dudarev, S. L., Botton, G. A., Savrasov, S. Y., Humphreys, C. J. & Sutton, A. P. Electron-energy-loss spectra and the structural stability of nickel oxide: An LSDA + U study. *Phys. Rev. B* **57**, 1505–1509 (1998).

Acknowledgments

Author contributions

L.G., P.G.-N. and V.M.L. have been carried the calculations and the theoretical part. M.F. and P.S.L. prepared the samples and performed the structural analysis; D.P.V. and W.A. performed the electron microscopy data collection. F.A.L.P. has been carried out the XPS analysis. J.A., A.C.H. and E.L. conceived the project. All of the authors participated in writting the manuscript and discussion of the results.

Additional information

Supplementary information accompanies this paper at http://www.nature.com/scientificreports

Competing financial interests: The authors declare no competing financial interests.

How to cite this article: Andrés, J. *et al.* Structural and electronic analysis of the atomic scale nucleation of Ag on α-Ag_2WO_4 induced by electron irradiation. *Sci. Rep.* **4**, 5391; DOI:10.1038/srep05391 (2014).

2.3 – **Toward an Understanding of the Growth of Ag Filaments on *α-Ag₂WO₄* *and* *Their* *Photoluminescent* *Properties:* *A* *Combined* *Experimental and Theoretical Study***

Toward an Understanding of the Growth of Ag Filaments on α-Ag₂WO₄ and Their Photoluminescent Properties: A Combined Experimental and Theoretical Study

Elson Longo,[†] Diogo P. Volanti,*[,‡] Valéria M. Longo,[†] Lourdes Gracia,[§] Içamira C. Nogueira,[⊥] Marcio A. P. Almeida,[†] Antonio N. Pinheiro,[⊥] Mateus M. Ferrer,[⊥] Laécio S. Cavalcante,[∥] and Juan Andrés[§]

[†]Instituto de Química, UNESP−Universidade Estadual Paulista, R. Francisco Degni, 55, Araraquara 14800-900, Brazil

[‡]Departamento de Química e Ciências Ambientais, UNESP−Universidade Estadual Paulista, R. Cristóvão Colombo, 2265, São José do Rio Preto 15054-000, Brazil

[§]Departament de Química Física i Analítica, UJI−Universitat Jaume I, Av. de Vicent Sos Baynat, s/n, Castelló de la Plana 12071, Spain

[⊥]Departamento de Química, UFSCar−Universidade Federal de São Carlos, Rod. Washington Luis, km 235, São Carlos 13565-905, Brazil

[∥]Departamento de Química, UESPI−Universidade Estadual do Piauí, R. João Cabral, 2231, Teresina 64002-150, Brazil

Ⓢ *Supporting Information*

ABSTRACT: A combined experimental and theoretical study was conducted on the structure and electronic properties of α-Ag₂WO₄ to clarify the nucleation and growth processes of Ag filaments on α-Ag₂WO₄ crystals induced by electron beam irradiation under electron microscopy. X-ray diffraction with Rietveld analysis, micro-Raman and Fourier-transform infrared spectroscopy were used to analyze the structural order/disorder of α-Ag₂WO₄ crystals. These complementary techniques indicated that the microwave-assisted hydrothermal method employed in the synthesis of α-Ag₂WO₄ crystals leads to the freezing of distorted [WO₆] and [AgOᵧ] (y = 2, 4, 6 and 7) clusters as the constituent polyhedra of α-Ag₂WO₄. On the basis of the theoretical and experimental results, we provide a complete assignment of the structure of α-Ag₂WO₄ and describe the relationship among the disorder, nucleation growth, rate of Ag formation, and photoluminescence behavior before and after the irradiation of the accelerated electron beam. Density functional theory (DFT) studies indicated significant changes in the order−disorder of the initial α-Ag₂WO₄electronic structure, with a decrease in the band gap value from 3.55 to 2.72 eV. The first stages of the electron irradiation on α-Ag₂WO₄ crystal were investigated by DFT calculations, and we have derived a mechanism to describe the formation and growth of Ag filaments during the electronic excitation of the [AgO₂] cluster.
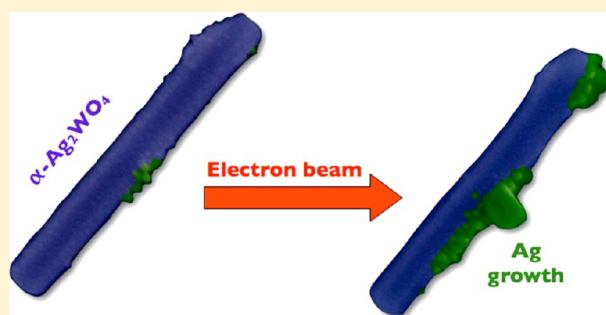
1. INTRODUCTION

Nanoparticle growth mechanisms have received much attention in recent years; controlling the size and morphologies of nanostructures is important for technological application. In this context, *in situ* electron microscopy constitutes an elegant technique that uncovers dynamic processes in the growth of nanocrystals. Recent technological advancements, in conjunction with high-resolution imaging, provide a new opportunity to view nanoscale processes. These advancements have been made possible as a result of the expansion and diffusion of transmission electron microscopy (TEM) heating holders for *in situ* electron microscopy.[1−5] Several studies have reported using the TEM heating holder to monitor the crystal growth of different nanomaterials, such as bismuth,[6] germanium,[7] indium−arsenide,[8] and vanadium oxide,[9] and *in situ* liquid

TEM has been employed to understand the growth process of copper and lead sulfide nanostructures.[10−12] The greatest impact of this new method of investigating the stages of crystal growth is the possibility to observe the step-by-step evolution of the crystal at the nanoscale.[13,14]

The preparation and characterization of noble metal nanoparticles is an interdisciplinary subject and has attracted much attention due to the fundamental and applied scientific value of nanometer-sized metals.[15−20] Among these metals, Ag nanoparticles possess unique properties with a wide range of applications, from surface-enhanced Raman spectroscopy[21,22]

to their use as an antibacterial agent.[23−29] Over the past decade, Ag nanocrystals of myriad shapes have been synthesized using various methods.[18,30−36] In this context, an emerging trend in nanotechnology is the creation of new nanomaterials and the exploration of their novel physical and chemical properties.[37−39] Often, newly identified nanomaterials bring to light previously undiscovered phenomena. One example, which changed the direction of noble metal research, is the first real-time, *in situ* nucleation and growth of Ag filaments on α-Ag_2WO_4 crystals, driven by an accelerated electron beam from an electronic microscope under high vacuum.[40]

In the present paper, a combined experimental and theoretical study was conducted on the structural arrangement that leads to the interesting growth process of Ag filaments on the α-Ag_2WO_4 crystal surface induced by field-emission scanning electron microscopy (FESEM) and complementary transmission electron microscopy (TEM) with selected-area diffraction (SAD) characterization; the photoluminescence (PL) enhancement of the Ag filaments was also investigated. X-ray diffraction (XRD) with Rietveld refinement, micro-Raman (MR) spectroscopy and Fourier transform infrared spectroscopy (FTIR) were used to analyze the structural order and disorder conditions of the α-Ag_2WO_4 structure prior to the Ag growth. The shape evolution and growth process of the α-Ag_2WO_4 crystals synthesized using a microwave-assisted hydrothermal (MAH) method at different temperatures was analyzed. The first stages of the Ag formation on α-Ag_2WO_4 crystal provoked by electron irradiation were simulated by first-principles calculations based on density functional theory (DFT). The order−disorder structural conditions of the growth evolution and photoluminescence (PL) enhancement were inferred based on the theoretical results.

2. EXPERIMENTAL SECTION

2.1. Synthesis of α-Ag_2WO_4. The typical α-Ag_2WO_4 crystal synthesis procedure was followed: 1×10^{-3} mol sodium tungstate dihydrate ($Na_2WO_4 \cdot 2H_2O$, 99.5% purity, Sigma-Aldrich) and 2×10^{-3} mol silver nitrate ($AgNO_3$, 99.8% purity, Sigma-Aldrich) were separately dissolved in test tubes containing 50 mL deionized water. Before the addition of the salts, 0.5 g sodium dodecyl sulfate (SDS) ($C_{12}H_{25}SO_4Na$, 99% purity, Sigma-Aldrich) was dissolved in both of the tubes. The 100-mL combined suspension was transferred into a fluorinated ethylene propylene (PTFE) autoclave without stirring. The autoclave was then sealed and placed in a microwave-aided device for hydrothermal synthesis.[41] α-Ag_2WO_4 samples were prepared at different temperatures (100, 120, 140, and 160 °C) for 1 h. The α-Ag_2WO_4 crystals were obtained as light beige, fine powder. The precipitates were collected and washed several times with acetone and dried at room temperature for 6 h.

2.2. Characterizations. The samples were characterized by XRD using a D/Max-2500PC diffractometer (Rigaku, Japan) with Cu Kα radiation ($\lambda = 1.5406$ Å) in the 2θ range from 10° to 70° in the normal routine with a scanning velocity of 2°/min and from 10° to 110° with a scanning velocity of 1°/min in the Rietveld routine, both with a step of 0.02°. MR measurements were recorded using a LabRAM HR 800 mm model (Horiba, Jobin-Yvon, France). High-resolution Raman spectra were recorded with a He−Ne laser at 632.81 nm (model CCD DU420AOE325) operating at 25−1000 cm^{-1} and keeping its maximum output power at 6 mW. A 50-μm lens was used to prevent sample overheating. FTIR spectra were recorded from 250 to 1000 cm^{-1} using KBr pellets and a Bomem-Michelson spectrophotometer in transmittance mode (model MB-102). UV−vis spectra were recorded using a Varian spectrophotometer (model Cary 5G) in diffuse reflectance mode. The shapes and sizes of the α-Ag_2WO_4 microcrystals were observed with a field-emission scanning electron microscope (model Inspect F50, FEI Company, Hillsboro, OR) operating at 10

kV. TEM analyses were performed with a CM200-Philips microscope operating at 200 kV. The structural characterization of the samples was estimated using SAD. Specimens for TEM images were obtained by drying droplets of as-prepared samples from an acetone dispersion that had been sonicated for 10 min and deposited on 300-mesh Cu grids. PL measurements were performed with a Monospec 27 monochromator (Thermal Jarrel Ash) coupled to an R446 photomultiplier (Hamamatsu Photonics, Japan). A krypton-ion laser (Coherent Innova 90K; $\lambda = 350.7$ nm) was used as the excitation source; its maximum output power was maintained at 500 mW. The laser beam was passed through an optical chopper, and its maximum power on the sample was maintained at 40 mW. PL measurements were performed at room temperature.

2.3. Theoretical Calculation. Calculations for α-Ag_2WO_4 crystal were performed with a CRYSTAL09 program package.[42,43] Tungsten was described by a large-core ECP, derived by Hay and Wadt, and modified by Cora et al.[44] Silver and oxygen centers were described using HAYWSC-311d31G and O (6-31d1G) basis sets, respectively, which were taken from the Crystal Web site.[45] Becke's three-parameter hybrid nonlocal exchange functional,[46] was used in combination with a Lee−Yang−Parr gradient-corrected correlation functional (B3LYP).[47] The diagonalization of the Fock matrix was performed at adequate k-points grids in the reciprocal space. The thresholds controlling the accuracy of the calculation of the Coulomb and exchange integrals were set to 10^{-8} (ITOL1 to ITOL4) and 10^{-14} (ITOL5), and the percent of Fock/Kohn−Sham matrices mixing was set to 40 (IPMIX = 40).[42] The band structure and the density of states (DOS) projected on atoms and orbitals of bulk α-Ag_2WO_4 were constructed along the appropriate high-symmetry directions of the corresponding irreducible Brillouin zone. To take into account the negative charged system, we inserted two additional electrons in the Ag atom of the $[AgO_2]$ clusters, and in order to simulate properly this electron excess an all-electron basis set (9766-3114d1G),[45] was used to describe this Ag center.

3. RESULTS AND DISCUSSION

The XRD patterns (Figure 1) indicate that all prepared α-Ag_2WO_4 crystals have an orthorhombic structure without any deleterious phases and belong to the space group $Pn2n$, with a C_{2v}^{10} symmetry.[48] These crystals have sharp and well-defined
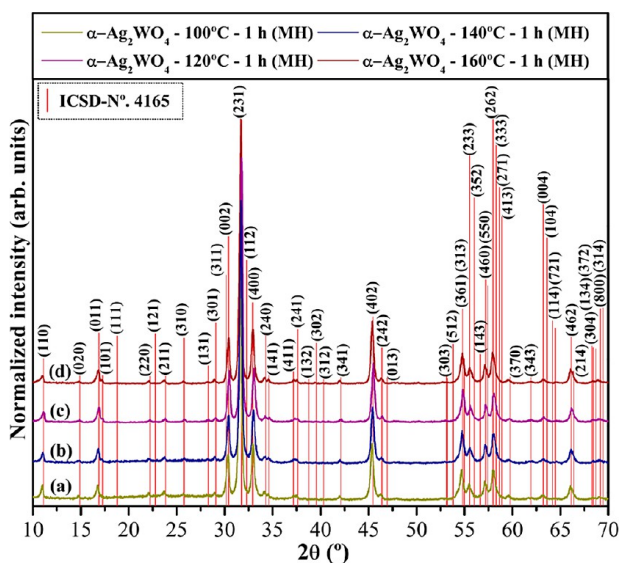
Figure 1. XRD patterns of α-Ag_2WO_4 microcrystals prepared at (a) 100, (b) 120, (c) 140, and (d) 160 °C for 1 h by the MAH method. The vertical lines indicate the position and relative intensity of the data from ICSD No. 4165 for the α-Ag_2WO_4 phase.
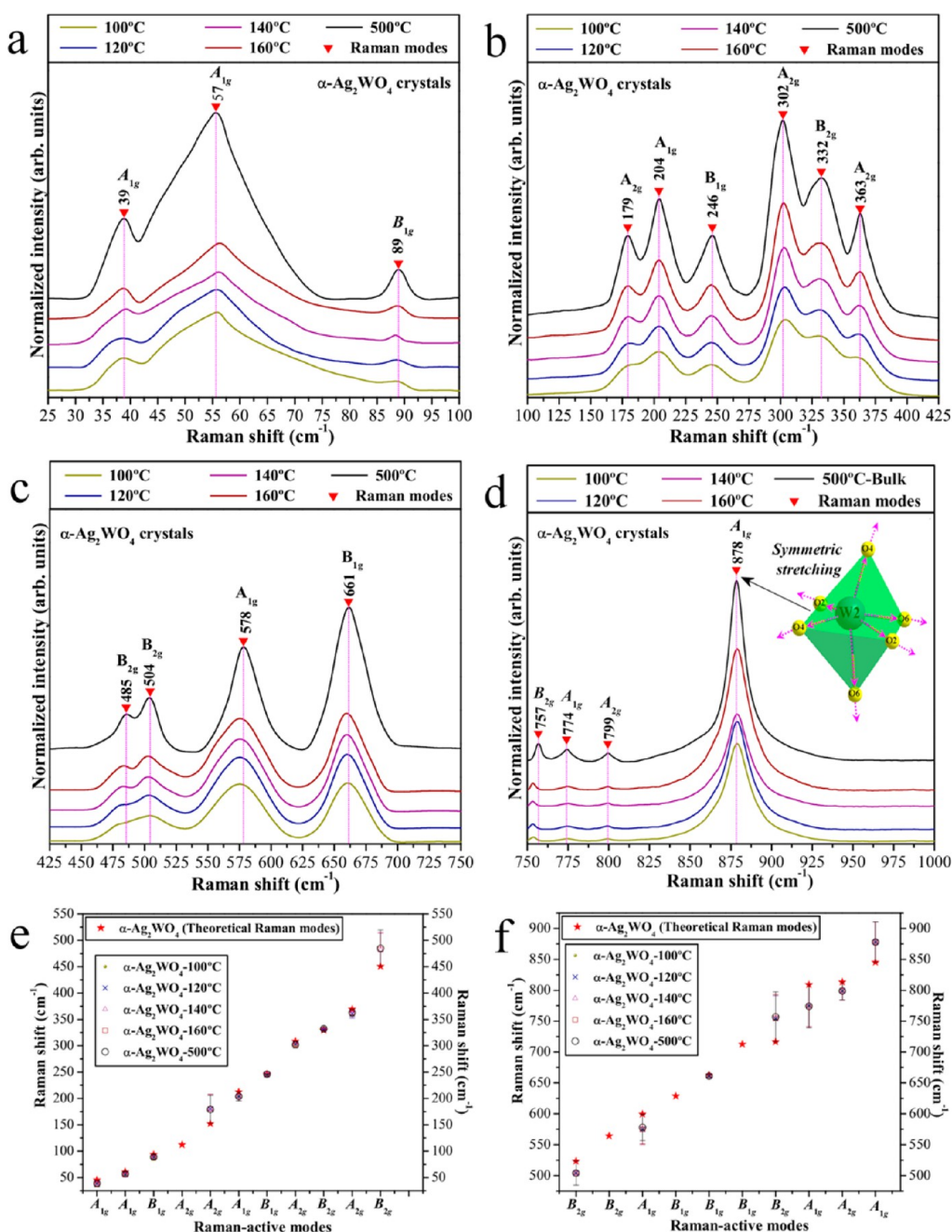
Figure 2. Micro-Raman spectra of α-Ag$_2$WO$_4$ prepared at different temperatures (100, 120, 140, and 160 °C) for 1 h by the MAH method, and by the coprecipitation method heat treated at 500 °C for 1 h (a) from 25 to 100 cm^{-1}, (b) from 100 to 425 cm^{-1}, (c) from 425 to 750 cm^{-1}, and (d) from 750 to 1,000 cm^{-1}. The vertical lines indicate the relative positions of the Raman-active modes. (e, f) Comparison of the theoretical and experimental Raman-active modes from 25 to 550 cm^{-1} and from 500 to 900 cm^{-1}, respectively.

diffraction peaks, which indicate a structural order and crystallinity at long-range. However, it is difficult to confirm the existence of Ag nanoparticles in these crystals based on XRD measurements.[49] Moreover, all diffraction peaks are in close agreement with the inorganic crystal structure database (ICSD) (N°. 416525) and the literature.[50] The Rietveld analysis also corroborates these results (Figures S1 and S2 and Tables S1−S5, Supporting Information).

The MR spectra of the α-Ag$_2$WO$_4$ crystals synthesized using the MAH method, and the relative positions of the theoretical

and experimental Raman-active modes are depicted in Figure 2, including labels for the A$_{1g}$, A$_{2g}$, B$_{1g}$, and B$_{2g}$ modes. The active Raman modes can exhibit a variable intensity because the rotation of the x-, y- and z-axes of the α-Ag$_2$WO$_4$ crystals occurs at different scattering of the tensors and components.[51] As can be observed in Figure 2a−d, the MR spectra revealed the presence of 17 Raman-active vibrational modes. Four additional Raman modes (two B$_{1g}$, one A$_{2g}$ and one B$_{2g}$) were not detectable experimentally because of their low intensities. Raman spectroscopy can be employed as a probe to investigate

the degree of structural order−disorder at short-range in the materials.[52,53] Therefore, 17 well-defined Raman-active vibrational modes can be observed for typical α-Ag$_2$WO$_4$ crystals, indicating a high degree of short-range structural order in the lattice. However, this behavior was not observed in the α-Ag$_2$WO$_4$ crystals synthesized by the MAH method, particularly in the sample treated at 100 °C. It is notable that the MR spectra of the synthesized crystals exhibited broad vibrational modes, indicating structural disorder at short-range. In addition, the disorder increased with the temperature treatment. This characteristic can be related to the very rapid kinetics of the MAH synthetic conditions. The MR spectrum of the sample treated at 100 °C did not present well-defined Raman peaks due to major short-range structural disorder.

Another interesting and important feature is the more pronounced structural local order presented by the lattice in the form of [WO$_6$] clusters (see Figure 2d), as opposed to the lattice modifier assigned to [AgO$_y$] (y = 7, 6, 4 and 2) clusters (Figure 2a−c). Specifically, the α-Ag$_2$WO$_4$ crystals prepared by the MAH method presented more well-defined Raman-active vibrational modes related to the symmetric stretching of ($\leftarrow$O$\leftarrow$W$\rightarrow$O$\rightarrow$) bonds of the octahedral [WO$_6$] clusters than for the external vibrational modes of the distorted [AgO$_y$] (y = 7, 6, 4 and 2) clusters. The theoretical Raman-active modes were calculated through the atomic positions and lattice parameters for the optimized α-Ag$_2$WO$_4$ crystals and are illustrated in Figure 2e and f and presented in Table S6. There is good agreement among the Raman-active modes of the α-Ag$_2$WO$_4$ crystals obtained in our samples, the first-principles calculation and the previously reported results from Turkovic et al.[51] The two B_{1g}, one A_{2g} and one B_{2g} modes that were not experimentally observed (Figure 2e,f) were predicted by the first-principles calculation, suggesting that their intensity may be too low in the Raman spectrum. The slight variations in the positions of the typical vibrational modes of our sample when compared with those reported in the literature can be attributed to the preparation method, average crystal size, distortions of the (O−Ag−O)/(O−W−O) bonds at short-range and/or intermolecular forces between the [AgO$_y$]−[WO$_6$]−[AgO$_y$] clusters at intermediate range. Moreover, our theoretical calculations do not consider the nonharmonic contribution to the crystal-lattice vibration phonons.

Figure 3 shows the FTIR spectra for the α-Ag$_2$WO$_4$ samples and the specific theoretical/experimental infrared modes. Figure 3a indicates that four active IR vibrational modes are possible. According to the literature,[54] the IR spectrum provides information on the degree of structural order−disorder in the metal−oxygen bonds. Figure 3a−d reveals two intense absorption bands at 830 and 862 cm^{-1} for all of the α-Ag$_2$WO$_4$ microcrystals. These modes are ascribed to the asymmetric stretching vibrations of the ($\leftarrow$O$\leftarrow$W$\leftarrow$O$\leftarrow$)/($\rightarrow$O$\rightarrow$W$\rightarrow$O$\rightarrow$) bonds within the distorted octahedral [WO$_6$] clusters (see the inset in Figure 3). The active IR vibrational internal mode at 320 cm^{-1} is related to the symmetric bending vibrations within the distorted [WO$_6$] clusters,[55] and the active IR vibrational external mode at 296 cm^{-1} is assigned to the torsional motion of the distorted octahedral [WO$_6$] clusters.[56] Peak positions refer to the IR-active vibrational modes, which are shown in Table S7 and are compared with other methods as reported in the literature.[55,57] Figure 3b shows the close agreement between the experimental IR-active modes and the theoretically calculated modes, indicated by the ★ symbol. In terms of spectral positions, small deviations in the IR-active
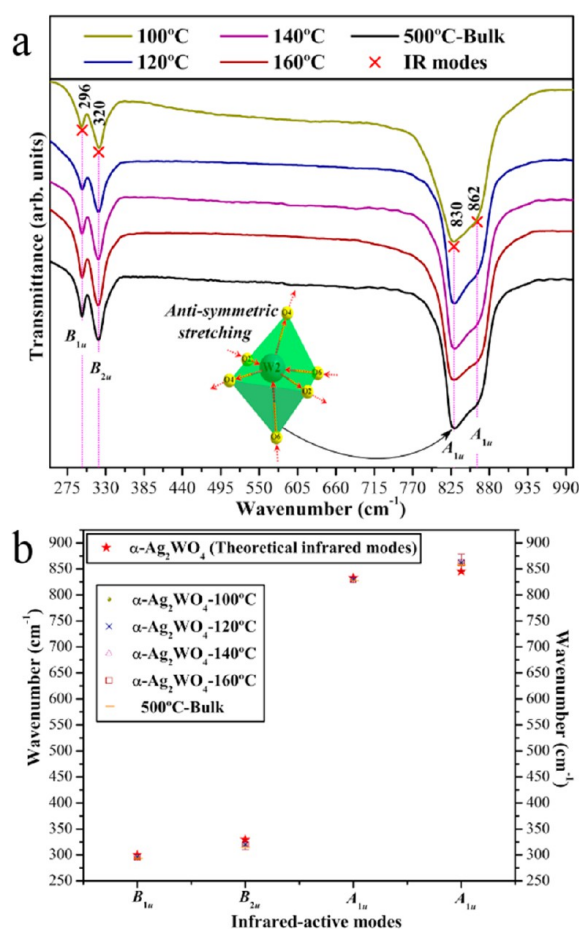
Figure 3. (a) FTIR spectra of α-Ag$_2$WO$_4$ prepared at different temperatures (100, 120, 140, and 160 °C) for 1 h by the MAH method. The vertical lines indicate the relative positions of the infrared-active modes. (b) Comparison between the theoretical and experimental infrared-active modes from 250 to 900 cm^{-1}.

modes of the α-Ag$_2$WO$_4$ crystals can be attributed to different degrees of interaction and modification of the O−Ag−O and O−W−O bond lengths and/or angles within the [AgO$_y$] and [WO$_6$] clusters. The optical band gap energy (E_{gap}) of the α-Ag$_2$WO$_4$ crystals was experimentally investigated using the method proposed by Kubelka and Munk.[58] This methodology is based on the transformation of diffuse reflectance measurements to estimate E_{gap} values with high accuracy within the limits of assumptions when modeled in three dimensions.[59] According to Tang et al.[60] and Kim et al.,[61] silver tungstate crystals exhibit an optical absorption spectrum governed by the direct electronic transitions between the valence and conduction bands; this behavior is supported by the theoretical calculations. In this electronic process, after the electronic excitation, the electrons located in the maximum-energy states in the valence band fall back to the minimum-energy states in the conduction band under the same point in the Brillouin zone.

Figure 4a reveals that the band structures for the optimized bulk α-Ag$_2$WO$_4$ crystal are characterized by well-defined direct electronic transitions, which is typical of crystalline semiconductor materials. Fundamentally, the top of the VB and the bottom of the CB are in the same Γ to Γ point in the Brillouin zone. The value of the theoretically calculated band gap, 3.55
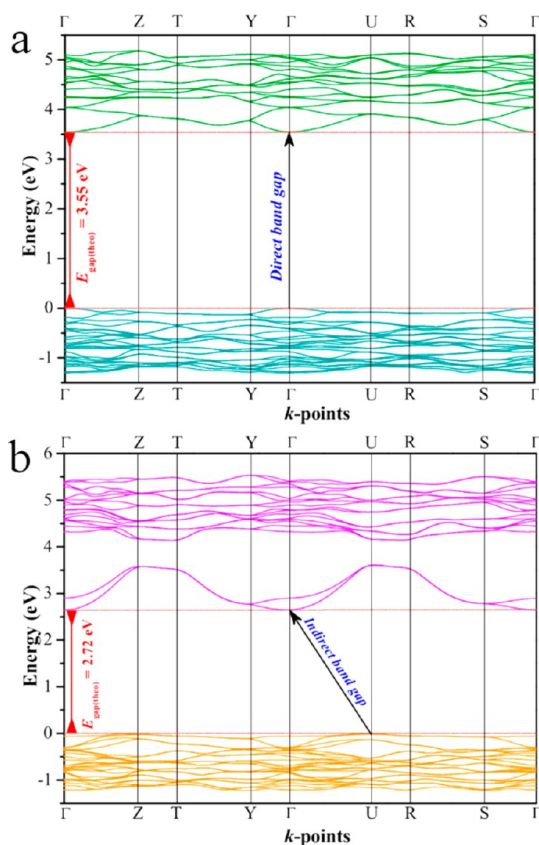
Figure 4. Band structures for optimized bulk α-Ag$_2$WO$_4$ crystal (a) in the neutral state and (b) charged with two electrons on the [AgO$_2$] clusters.

eV, was slightly higher than the experimental value of ~3.2 eV, estimated by UV–vis spectroscopy, for all samples synthesized by the MAH method. This overestimation of the predicted band gap can be due to the fact that it is calculated from the difference between the bottom of the conduction band (CB) and the top of the valence band (VB) within the Kohn–Sham formalism. However, it must be considered that the theoretical calculations estimate the optimized structure with a minimum energy, and the experimental structure derived from the MAH treatment conserves freezing distortions at short and intermediate range, which are not the most stable structures. Moreover, the band structure of this complicated network arrangement of [WO$_6$] and [AgO$_y$] clusters is basically determined by the W 5d orbitals in the conduction band (CB) and a valence band (VB) derived mostly from hybridized O 2p and Ag 4d orbitals. This reduction in the experimentally optical band gap value is most likely linked to distortions of the [WO$_6$]/[AgO$_y$] that are favorable to the formation of intermediate energy levels (photogenerated electron–hole pairs) between the VB and CB.

To simulate the electron absorption process based on the α-Ag$_2$WO$_4$ structure, theoretical calculations were performed while taking into account the incorporation of two electrons in the structure. An analysis of the α-Ag$_2$WO$_4$ structure shows that the [AgO$_2$] cluster presents the largest value of positive Mülliken charge for the Ag moiety, with only two adjacent oxygen anions. Therefore, this cluster was the most appropriate candidate to receive the external electron beam irradiation; in a

sense, we inserted two additional electrons in the Ag atom of the [AgO$_2$] cluster as a starting point and atomic positions were optimized. The resulting geometry is presented in Table S5b. Figure 4b depicts the band structure for optimized neutral bulk α-Ag$_2$WO$_4$ crystal charged with two electrons on the [AgO$_2$] clusters. An analysis of the band structure and the DOS (Figure S3a) for the charged system points out that intermediate levels are formed in the vicinity of the CB, which are composed of 5s orbitals of [AgO$_2$]. Therefore, new energy levels are created in the forbidden region of the band gap, leading to a disordered structure (Figure S3b). The Fermi level is now located at approximately 3.0 eV, considering the VB maximum at the zero-energy level, and the presence of these electron traps reduces the band gap energy to 2.72 eV, becoming indirect from the U point to the Γ point (Figure 4b, Figure S3).

Figure 5 shows the DOS projected on the 4d, 5d, and 2p orbitals of Ag, W and O atoms, respectively, for neutral α-Ag$_2$WO$_4$. The DOS structure of this complex network arrangement can be analyzed in terms of orbitals contribution of the atoms that form [WO$_6$] and [AgO$_y$] (y = 7, 6, 4 and 2) polyhedra. Figure 5a and b show that the projected DOS on the orbitals of the Ag1 and Ag2 atoms, coordinated by seven oxygens ([AgO$_7$]), are basically derived from the 4d$_{xz}$ orbital of the valence band. The same relationship occurs with the Ag3 atom, coordinated by six oxygens ([AgO$_6$]), as depicted in Figure 5c. When the coordination changes to four ([AgO$_4$]), as in the Ag4 and Ag5 atoms, the major contribution is derived from the 4d$_{xz}$ and 4d$_{z^2}$ orbitals (see Figure 5d,e). Finally, in the bicoordinated Ag6 atom ([AgO2]) the VB is mostly composed by 4d$_{xz}$ orbital (see Figure 5f). The projected DOS on the W atom is basically determined by the 5d orbitals in the conduction band (CB) with more important role of 5d$_{z^2}$ orbitals (Figure 5g). The valence band (VB) is primarily derived from hybridized O 2p (Figure 5h) and Ag 4d orbitals.

A study of the growth of Ag on the α-Ag$_2$WO$_4$ surface as a function of exposure time to a scanning electron microscope under an accelerating voltage of 10 kV was carried out. The onset of Ag nanoparticle nuclei on the surface of the α-Ag$_2$WO$_4$ crystals was observed by the FESEM images (Figure 6) as soon as the samples began to be analyzed. This behavior was observed for all the samples synthesized at different temperatures, namely, 100, 120, 140, and 160 °C (Figure 6, parts a, c, e and g, respectively). After 5 min of irradiation, the growth of the initial particles of Ag and the onset of new nuclei growth were observed in all the samples (100, 120, 140, and 160 °C) (Figure 6, parts b, d, f, and h, respectively). It is important to emphasize that the sample prepared at 160 °C (Figure 6h) has a higher number of Ag nuclei as well as a higher absorption of existing particles. This behavior was also demonstrated in our previous work.[40] In this way, the most organized sample (160 °C) favors the nucleation of metallic Ag nanorods. However, the growth process occurs preferentially in samples where the nucleation is smaller. Table S9 (of the Supporting Information) presents the calculated values of the surface energy for (001), (100), (010), (011), (101) and (110) facets of α-Ag$_2$WO$_4$. The surface (100) is the most stable facet, with the higher percentage of the relaxing process. If charged α-Ag$_2$WO$_4$ structure is focused on the plane (100) compared to the equilibrium geometry, it can be see an approaching of Ag4 and Ag5 centers (from 4.0 to3.26 Å) when the system is charged in the vicinity of Ag6 atoms. In addition, Ag6–O distance increases from 2.34 to2.54 Å showing that this situation favors an accumulation of Ag atoms along the most stable (100)
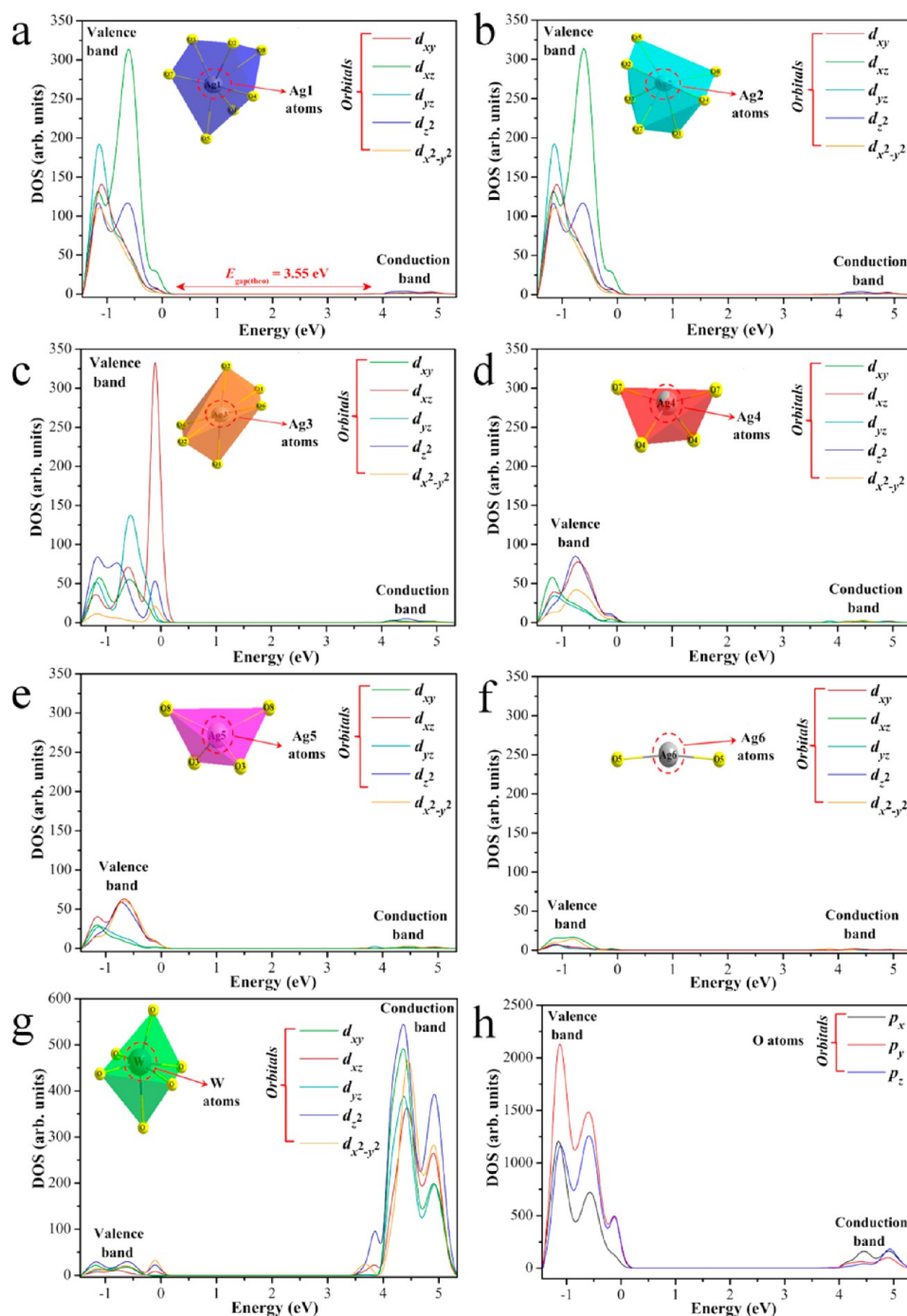
Figure 5. DOS projected on the 4d, 5d, and 2p orbitals of (a−f) Ag, (g) W, and (h) O atoms, respectively.

surface. Therefore, the *ab initio* calculations indicate that the absorption of electrons leads to the disordered structure that facilitates Ag nucleation. It is possible that a more ordered structure has a more homogeneous surface and thus facilitates a more homogeneous nucleation; a more detailed study of this system is necessary to test this possibility. The TEM images of all samples and the structural electron diffraction (SAD) details of the growth process of Ag on the α-Ag_2WO_4 crystals are shown in Figures S4 and S5 and Table S8 in the Supporting Information.

Figure 7 shows the PL spectra recorded at room temperature for the α-Ag_2WO_4 samples, excited by a 350.7 nm line of a krypton ion laser, before and after irradiation by an accelerated electron beam. The PL spectral profiles show typical behavior for multiphonon or multilevel processes, i.e., a solid system where relaxation occurs by several pathways, which involve the participation of numerous energy states within the band gap.[62] It is generally assumed that the blue-green emission of tungstate is due to the charge-transfer transitions within the $[WO_4]^{2-}$ complex in ordered systems,[63−67] or complex cluster vacancies in the former,[68−70] and/or modified lattice.[70] It is
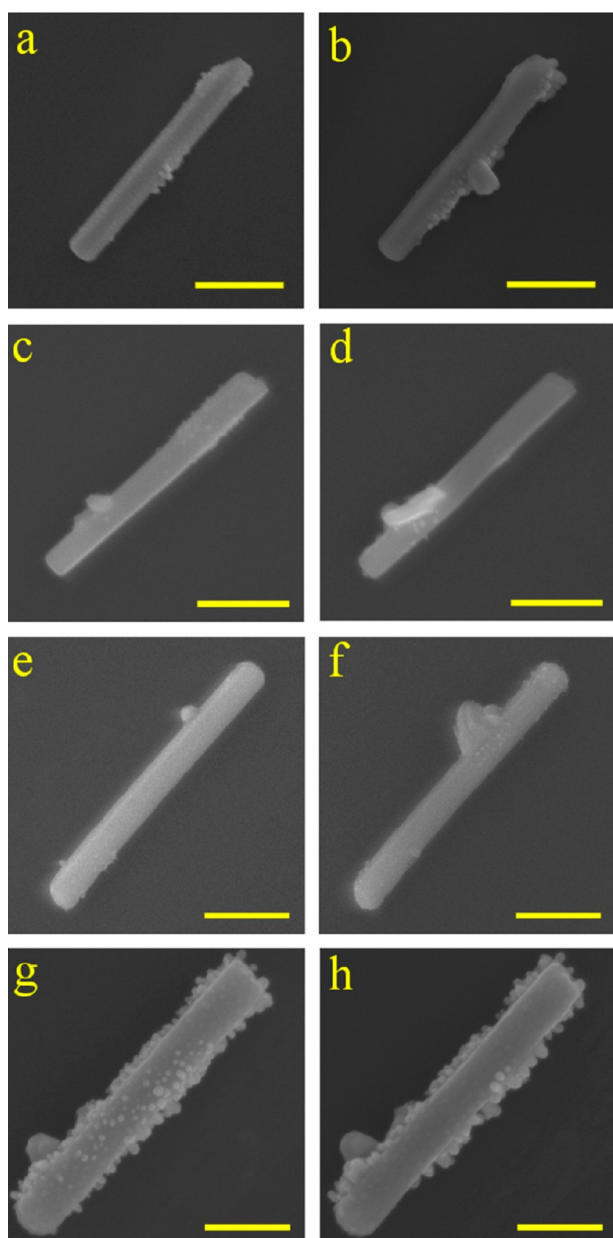
Figure 6. Initial FESEM images of the α-Ag$_2$WO$_4$ samples obtained by the MAH method at (a) 100, (c) 120, (e) 140 and (g) 160 °C. After 5 min, microscopy analyses of the same samples were recorded: (b) 100, (d) 120, (f) 140, and (h) 160 °C. (Scale bar = 400 nm in parts a–f and 200 nm in parts g and h.)

well-known that the physical and chemical properties of materials are strongly correlated with structural factors, primarily the structural order–disorder in the lattice. The materials can be described in terms of the packing of the constituent clusters, which can be considered as the structural motifs. A specific feature of tungstates with a scheelite structure is the existence of $[WO_6]$ and $[AgO_y]$ clusters in a crystal lattice.[71] This orthorhombic structure can also be understood in terms of a network of $[WO_6]$ clusters, linked by strong bonds [...W−O−W...] between the neighboring clusters, whose internal vibration spectra provide information on the structure and order–disorder effects in the crystal lattices.[72,73] Breaking

the symmetry of these clusters through distortions, breathings and tilts creates a large number of different structures with different material properties; this phenomenon can be related to local (short), intermediate and long-range structural order–disorder. Therefore, for α-Ag$_2$WO$_4$, the material properties can be primarily associated with the constituent clusters, and the disparity or mismatch of both clusters can induce structural order–disorder effects, which significantly influence the luminescence properties of the tungstates.[74−76]

Disorder in materials can be manifested in many ways; examples include vibrational, spin and orientation disorder (referenced to a periodic lattice) and topological disorder. Topological disorder is the type of disorder associated with glassy and amorphous solid structures in which the structure cannot be defined in terms of a periodic lattice. PL is a powerful probe of certain aspects of short-range (2−5 Å) and medium-range order (5−20 Å), such as clusters where the degree of local order is such that structurally inequivalent sites can be distinguished due to their different types of electronic transitions which are linked to a specific structural arrangement.[62]

In Figure 7a, the maximum blue PL emission peak is centered at 449 nm for all the samples; however, another diffuse emission in the red region peaking from 621 to 640 nm was also observed. The nucleation−dissolution−recrystallization mechanism favored by the MAH process can be seen as an order−disorder−order process of nature and gives rise to a nonclassical crystallization process.[77] Using density functional calculations, Ghazi et al.[78] noted that growth is an order−disorder−order pattern of cyclic nature. Between two ordered clusters, growth proceeds via disordered clusters, and global order emerges suddenly with the addition of only one or two atoms. In this sense, the different intensities in the emission profiles can be attributed to slight differences in the defect densities linked to the distorted clusters and complex vacancies generated by the MAH heat treatment. The first emission peak can be related to distorted $[WO_6]$ octahedra that are, in the case of our samples, more ordered, in accordance with the MR and IR spectral data and previous reports.[63−67] The emission in the red spectrum region is most likely linked to the $[AgO_y]$ clusters that form complex vacancies, inducing more disorder and deeper defects in the forbidden band gap. However, other factors may also be involved, such as the degree of aggregation and the orientation between particles, the variations in the particle size distribution, the morphology of the particles and surface defects. All these factors have an influence on the intensity of the PL emission.

The PL profile of irradiated α-Ag$_2$WO$_4$ depicted in Figure 7b is quite different from the nonirradiated PL profile (Figure 7a). No blue shift is observed in the emission maximum, indicating that the $[WO_6]$ clusters are unchanged by the irradiation (Figure 7c,f). However, the profile of the PL emission in the red region of the spectra is changed. As discussed above, these changes can be attributed to the $[AgO_y]$ clusters becoming more disordered by the Ag metallic growth on the surface. This process generates complex vacancies of V_{Ag}' and V_O^x (where $V_O^x = V_O^x, V_O^{\bullet}, V_O^{\bullet\bullet}$), but it is clear that the $[WO_6]$ surface clusters should also be slightly disordered as a result of Ag migration and Ag nanorod formation. As predicted by first-principles calculations, in the disordered structure the electronic levels are significantly affected by the inclusion of electrons, as it is observed in the band gap structure, favoring the red emission. The samples prepared at 100 (Figure 7c), 120 (Figure 7d), and
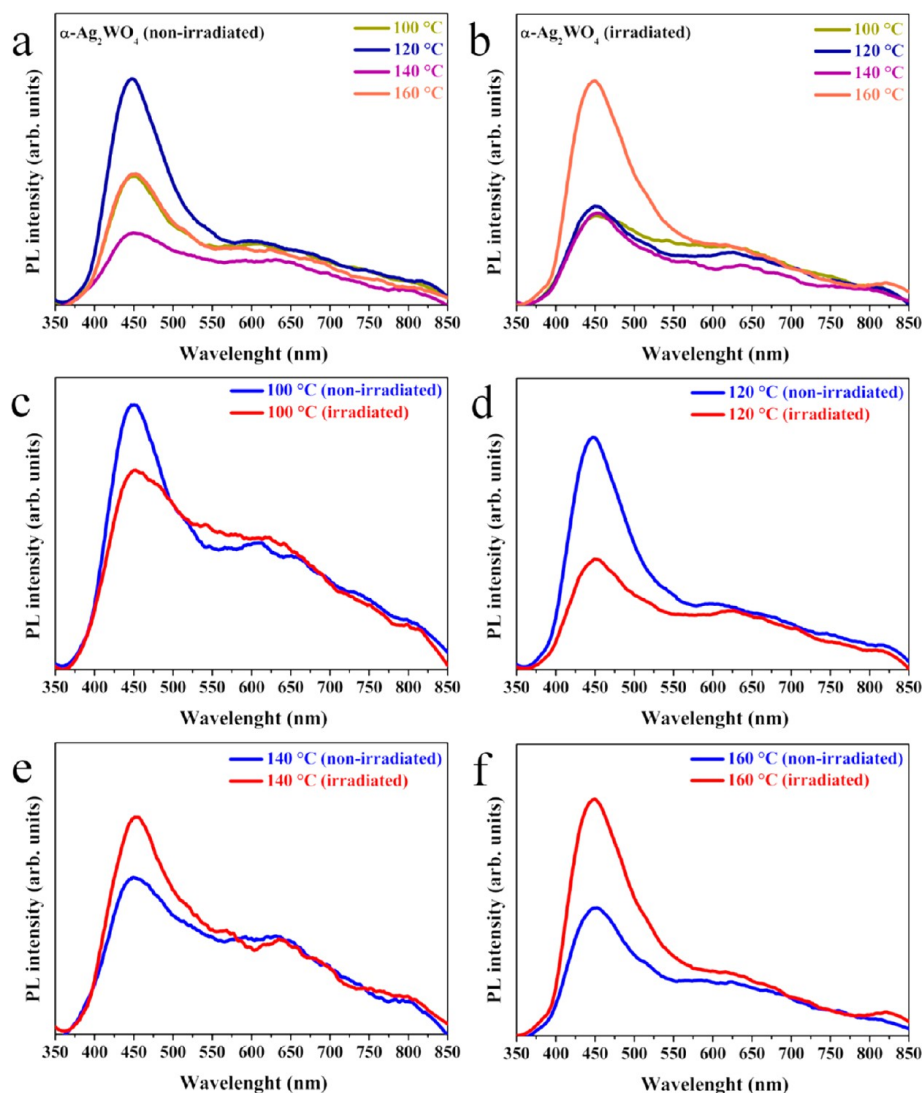
Figure 7. PL spectra recorded at room temperature of the α-Ag$_2$WO$_4$ crystals obtained by the MAH method at 100, 120, 140, and 160 °C, excited by a 350.7 nm line of a krypton ion laser (a) before and (b) after irradiation by an accelerated electron beam. For better visualization, we show the spectrum of each individual sample: (c) 100, (d) 120, (e) 140, and (f) 160 °C irradiated (red) and nonirradiated (blue).

140 °C (Figure 7e) show intermediate PL intensities. The maximum enhancement in PL emission after irradiation was observed in the sample heat-treated at 160 °C (Figure 7f). This sample presents the highest degree of structural order prior to irradiation, as discussed in the MR and FTIR analysis, and the highest nucleation rate after irradiation, as observed by FESEM (Figure 6h). The more abundant and homogeneous nucleation favored by the more ordered structure results in more V'_{Ag} and V''_{O} complex vacancies and a larger effect on the PL enhancement.

4. CONCLUSIONS

In this study, α-Ag$_2$WO$_4$ particles were successfully synthesized by an MAH method; XRD patterns and Rietveld analysis confirmed the orthorhombic structure obtained. The physical/chemical properties and the corresponding performance of the α-Ag$_2$WO$_4$ crystals are closely related to the crystal structure, and in the present case, the local electric fields or polarized fields in the distorted metal−oxygen polyhedra, namely [WO$_6$]

and [AgO$_y$] (y = 7, 6, 4, and 2). MR and FTIR spectroscopy indicate that the MAH method employed in the synthesis of α-Ag$_2$WO$_4$ crystals leads to the freezing of distorted [WO$_6$] and [AgO$_y$] clusters. An external electron beam irradiation induces the formation and crystal growth of Ag filaments on the α-Ag$_2$WO$_4$ crystal and a PL enhancement. This finding is reshaping our understanding of these molecular processes, revealing previously hidden subtleties. A theoretical investigation using density functional theory (DFT) was carried out to understand the introduction of electrons into the α-Ag$_2$WO$_4$ lattice. The results indicate that the electron-induced growth process of Ag on α-Ag$_2$WO$_4$ crystal is closely connected with the structural and electronic properties of the [AgO$_2$] cluster; this process results in a drastic increase of the structural and electronic disorder, as evidenced by the decrease in the band gap from 3.55 to 2.72 eV. Finally, no blue shift of the emission maximum was observed, indicating that the [WO$_6$] clusters were unchanged by the irradiation; however, changes were observed in the red region of the PL profile. These changes

were attributed to unstable $[AgO_y]$ clusters that became disordered by the growth of metallic Ag on the surface, leading to complex vacancies. First-principles calculations predicted that this process would lead to a disordered structure with deep defects inserted in the band gap, favoring the red emission. The results of this research provide fundamental insight into the PL properties of α-Ag$_2$WO$_4$ crystals, the electron-induced synthesis of Ag/α-Ag$_2$WO$_4$ and its relationship with the morphology by controlling surface/bulk defects. We believe that this process may also be applicable for controlling other properties such as microbial activity and photodegradation.

■ ASSOCIATED CONTENT

ⓢ Supporting Information

Figures and tables of Rietveld refinement analyses of the α-Ag$_2$WO$_4$ crystal, DFT analysis. and TEM analysis with the corresponding SAD characterization. This material is available free of charge via the Internet at http://pubs.acs.org.

■ AUTHOR INFORMATION

Corresponding Author

*E-mail: (D.P.V.) volanti@ibilce.unesp.br.

Notes

The authors declare no competing financial interest.

■ ACKNOWLEDGMENTS

■ REFERENCES

(1) Kamino, T.; Sasaki, K.; Saka, H. High Resolution Electron Microscopy in Situ Observation of Dynamic Behavior of Grain Boundaries and Interfaces at Very High Temperatures. *Microsc. Microanal* **1997**, *3*, 393–408.

(2) Saka, H.; Kamino, T.; Arai, S.; Sasaki, K. In Situ Heating Transmission Electron Microscopy. *MRS Bull.* **2008**, *33*, 93–100.

(3) Yaguchi, T.; Kanemura, T.; Shimizu, T.; Imamura, D.; Watabe, A.; Kamino, T. Development of a Technique for in Situ High Temperature Tem Observation of Catalysts in a Highly Moisturized Air Atmosphere. *J. Electron Microsc.* **2012**, *61*, 199–206.

(4) Parent, L. R.; Robinson, D. B.; Woehl, T. J.; Ristenpart, W. D.; Evans, J. E.; Browning, N. D.; Arslan, I. Direct in Situ Observation of Nanoparticle Synthesis in a Liquid Crystal Surfactant Template. *ACS Nano* **2012**, *6*, 3589–3596.

(5) Nam, S.-W.; Chung, H.-S.; Lo, Y. C.; Qi, L.; Li, J.; Lu, Y.; Johnson, A. T. C.; Jung, Y.; Nukala, P.; Agarwal, R. Electrical Wind Force-Driven and Dislocation-Templated Amorphization in Phase-Change Nanowires. *Science* **2012**, *336*, 1561–1566.

(6) Xin, H. L.; Zheng, H. In Situ Observation of Oscillatory Growth of Bismuth Nanoparticles. *Nano Lett.* **2012**, *12*, 1470–1474.

(7) Dayeh, S. A.; Picraux, S. T. Direct Observation of Nanoscale Size Effects in Ge Semiconductor Nanowire Growth. *Nano Lett.* **2010**, *10*, 4032–4039.

(8) Mandl, B.; Stangl, J.; Hilner, E.; Zakharov, A. A.; Hillerich, K.; Dey, A. W.; Samuelson, L.; Bauer, G.; Deppert, K.; Mikkelsen, A. Growth Mechanism of Self-Catalyzed Group III-V Nanowires. *Nano Lett.* **2010**, *10*, 4443–4449.

(9) Sohn, J. I.; Joo, H. J.; Porter, A. E.; Choi, C.-J.; Kim, K.; Kang, D. J.; Welland, M. E. Direct Observation of the Structural Component of the Metal-Insulator Phase Transition and Growth Habits of Epitaxially Grown VO$_2$ Nanowires. *Nano Lett.* **2007**, *7*, 1570–1574.

(10) Radisic, A.; Ross, F. M.; Searson, P. C. In Situ Study of the Growth Kinetics of Individual Island Electrodeposition of Copper. *J. Phys. Chem. B* **2006**, *110*, 7862–7868.

(11) Williamson, M. J.; Tromp, R. M.; Vereecken, P. M.; Hull, R.; Ross, F. M. Dynamic Microscopy of Nanoscale Cluster Growth at the Solid-Liquid Interface. *Nat. Mater.* **2003**, *2*, 532–536.

(12) Evans, J. E.; Jungjohann, K. L.; Browning, N. D.; Arslan, I. Controlled Growth of Nanoparticles from Solution with in Situ Liquid Transmission Electron Microscopy. *Nano Lett.* **2011**, *11*, 2809–2813.

(13) Yuk, J. M.; Park, J.; Ercius, P.; Kim, K.; Hellebusch, D. J.; Crommie, M. F.; Lee, J. Y.; Zettl, A.; Alivisatos, A. P. High-Resolution Em of Colloidal Nanocrystal Growth Using Graphene Liquid Cells. *Science* **2012**, *336*, 61–64.

(14) Park, J.; Zheng, H. M.; Lee, W. C.; Geissler, P. L.; Rabani, E.; Alivisatos, A. P. Direct Observation of Nanoparticle Superlattice Formation by Using Liquid Cell Transmission Electron Microscopy. *ACS Nano* **2012**, *6*, 2078–2085.

(15) Burda, C.; Chen, X. B.; Narayanan, R.; El-Sayed, M. A. Chemistry and Properties of Nanocrystals of Different Shapes. *Chem. Rev.* **2005**, *105*, 1025–1102.

(16) Xia, Y.; Xiong, Y.; Lim, B.; Skrabalak, Sara E. Shape-Controlled Synthesis of Metal Nanocrystals: Simple Chemistry Meets Complex Physics? *Angew. Chem., Int. Ed.* **2009**, *48*, 60–103.

(17) Murphy, C. J.; Gole, A. M.; Stone, J. W.; Sisco, P. N.; Alkilany, A. M.; Goldsmith, E. C.; Baxter, S. C. Gold Nanoparticles in Biology: Beyond Toxicity to Cellular Imaging. *Acc. Chem. Res.* **2008**, *41*, 1721–1730.

(18) Rycenga, M.; Cobley, C. M.; Zeng, J.; Li, W. Y.; Moran, C. H.; Zhang, Q.; Qin, D.; Xia, Y. N. Controlling the Synthesis and Assembly of Silver Nanostructures for Plasmonic Applications. *Chem. Rev.* **2011**, *111*, 3669–3712.

(19) Lim, B.; Jiang, M.; Camargo, P. H. C.; Cho, E. C.; Tao, J.; Lu, X.; Zhu, Y.; Xia, Y. Pd-Pt Bimetallic Nanodendrites with High Activity for Oxygen Reduction. *Science* **2009**, *324*, 1302–1305.

(20) Anker, J. N.; Hall, W. P.; Lyandres, O.; Shah, N. C.; Zhao, J.; Van Duyne, R. P. Biosensing with Plasmonic Nanosensors. *Nat. Mater.* **2008**, *7*, 442–453.

(21) Hutter, E.; Fendler, J. H. Exploitation of Localized Surface Plasmon Resonance. *Adv. Mater.* **2004**, *16*, 1685–1706.

(22) Hao, E.; Schatz, G. C. Electromagnetic Fields around Silver Nanoparticles and Dimers. *J. Chem. Phys.* **2004**, *120*, 357–366.

(23) Liu, J.; Sonshine, D. A.; Shervani, S.; Hurt, R. H. Controlled Release of Biologically Active Silver from Nanosilver Surfaces. *ACS Nano* **2010**, *4*, 6903–6913.

(24) Gunawan, C.; Teoh, W. Y.; Marquis, C. P.; Lifia, J.; Amal, R. Reversible Antimicrobial Photoswitching in Nanosilver. *Small* **2009**, *5*, 341–344.

(25) Kittler, S.; Greulich, C.; Diendorf, J.; Koeller, M.; Epple, M. Toxicity of Silver Nanoparticles Increases During Storage Because of Slow Dissolution under Release of Silver Ions. *Chem. Mater.* **2010**, *22*, 4548–4554.

(26) Sotiriou, G. A.; Teleki, A.; Camenzind, A.; Krumeich, F.; Meyer, A.; Panke, S.; Pratsinis, S. E. Nanosilver on Nanostructured Silica: Antibacterial Activity and Ag Surface Area. *Chem. Eng. J.* **2011**, *170*, 547–554.

(27) Christopher, P.; Xin, H.; Linic, S. Visible-Light-Enhanced Catalytic Oxidation Reactions on Plasmonic Silver Nanostructures. *Nat. Chem.* **2011**, *3*, 467–472.

(28) Kumar, A.; Vemula, P. K.; Ajayan, P. M.; John, G. Silver-Nanoparticle-Embedded Antimicrobial Paints Based on Vegetable Oil. *Nat. Mater.* **2008**, *7*, 236–241.

(29) Chernousova, S.; Epple, M. Silver as Antibacterial Agent: Ion, Nanoparticle, and Metal. *Angew. Chem., Int. Ed.* **2013**, *52*, 1636–1653.

(30) Jin, R. C.; Cao, Y. W.; Mirkin, C. A.; Kelly, K. L.; Schatz, G. C.; Zheng, J. G. Photoinduced Conversion of Silver Nanospheres to Nanoprisms. *Science* **2001**, *294*, 1901–1903.

(31) Jana, N. R.; Gearheart, L.; Murphy, C. J. Wet Chemical Synthesis of Silver Nanorods and Nanowires of Controllable Aspect Ratio. *Chem. Commun.* **2001**, 617−618.

(32) Tao, A.; Sinsermsuksakul, P.; Yang, P. Polyhedral Silver Nanocrystals with Distinct Scattering Signatures. *Angew. Chem., Int. Ed.* **2006**, *45*, 4597−4601.

(33) Pietrobon, B.; Kitaev, V. Photochemical Synthesis of Monodisperse Size-Controlled Silver Decahedral Nanoparticles and Their Remarkable Optical Properties. *Chem. Mater.* **2008**, *20*, 5186−5190.

(34) Zhang, J.; Li, S.; Wu, J.; Schatz, G. C.; Mirkin, C. A. Plasmon-Mediated Synthesis of Silver Triangular Bipyramids. *Angew. Chem., Int. Ed.* **2009**, *48*, 7787−7791.

(35) Coskun, S.; Aksoy, B.; Unalan, H. E. Polyol Synthesis of Silver Nanowires: An Extensive Parametric Study. *Cryst. Growth Des.* **2011**, *11*, 4963−4969.

(36) Lee, J.; Lee, P.; Lee, H.; Lee, D.; Lee, S. S.; Ko, S. H. Very Long Ag Nanowire Synthesis and Its Application in a Highly Transparent, Conductive and Flexible Metal Electrode Touch Panel. *Nanoscale* **2012**, *4*, 6408−6414.

(37) Ariga, K.; Vinu, A.; Yamauchi, Y.; Ji, Q. M.; Hill, J. P. Nanoarchitectonics for Mesoporous Materials. *Bull. Chem. Soc. Jpn.* **2012**, *85*, 1−32.

(38) Xiang, Q.; Yu, J.; Jaroniec, M. Graphene-Based Semiconductor Photocatalysts. *Chem. Soc. Rev.* **2012**, *41*, 782−796.

(39) Saha, K.; Agasti, S. S.; Kim, C.; Li, X.; Rotello, V. M. Gold Nanoparticles in Chemical and Biological Sensing. *Chem. Rev.* **2012**, *112*, 2739−2779.

(40) Longo, E.; Cavalcante, L. S.; Volanti, D. P.; Gouveia, A. F.; Longo, V. M.; Varela, J. A.; Orlandi, M. O.; Andres, J. Direct in Situ Observation of the Electron-Driven Synthesis of Ag Filaments on α-Ag$_2$WO$_4$ Crystals. *Sci. Rep.* **2013**, *3*.

(41) Longo da Silva, E.; Arana Varela, J.; de Araujo Almeida, D. K.; Paschoalini Volanti, D. Microwave Aided Device for Hydrothermal Synthesis of Nanostructured Oxides, Particularly Obtaining Particles of Metal Oxides, Comprises Container, in which Hydrothermal Reaction Takes Place, and Lid for Container. BR200815393-A2, 07 Dec 2010.

(42) Dovesi, R.; Saunders, V. R. R. C.; Orlando, R.; Zicovich-Wilson, C. M.; Pascale, F.; Civalleri, B.; Doll, K.; Harrison, N. M.; Bush, I. J.; D'Arco, P.; Llunell, M., *Crystal09 User's Manual*. University of Torino: Torino, Italy, 2009.

(43) Dovesi, R.; Orlando, R.; Civalleri, B.; Roetti, C.; Saunders, V. R.; Zicovich-Wilson, C. M. Crystal: A Computational Tool for the Ab Initio Study of the Electronic Properties of Crystals. *Z. Kristallogr.* **2005**, *220*, 571−573.

(44) Cora, F.; Patel, A.; Harrison, N. M.; Dovesi, R.; Catlow, C. R. A. An Ab Initio Hartree-Fock Study of the Cubic and Tetragonal Phases of Bulk Tungsten Trioxide. *J. Am. Chem. Soc.* **1996**, *118*, 12174−12182.

(45) Pileni, M. P. Supracrystals of Inorganic Nanocrystals: An Open Challenge for New Physical Properties. *Acc. Chem. Res.* **2008**, *41*, 1799−1809.

(46) Becke, A. D. Density-Functional Thermochemistry. 3. The Role of Exact Exchange. *J. Chem. Phys.* **1993**, *98*, 5648−5652.

(47) Lee, C. T.; Yang, W. T.; Parr, R. G. Development of the Colle-Salvetti Correlation-Energy Formula into a Functional of the Electron-Density. *Phys. Rev. B* **1988**, *37*, 785−789.

(48) Skarstad, P. M.; Geller, S. (W$_4$O$_{16}$)$_8$- Polyion in High-Temperature Modification of Silver Tungstate. *Mater. Res. Bull.* **1975**, *10*, 791−799.

(49) Wang, P.; Huang, B.; Qin, X.; Zhang, X.; Dai, Y.; Whangbo, M.-H. Ag/AgBr/WO$_3$ Center Dot H$_2$O: Visible-Light Photocatalyst for Bacteria Destruction. *Inorg. Chem.* **2009**, *48*, 10697−10702.

(50) Stone, D.; Liu, J.; Singh, D. P.; Muratore, C.; Voevodin, A. A.; Mishra, S.; Rebholz, C.; Ge, Q.; Aouadi, S. M. Layered Atomic Structures of Double Oxides for Low Shear Strength at High Temperatures. *Scr. Mater.* **2010**, *62*, 735−738.

(51) Turkovic, A.; Fox, D. L.; Scott, J. F.; Geller, S.; Ruse, G. F. High-Temperature Raman-Spectroscopy of Silver Tetra-Tungstate, Ag$_8$W$_4$O$_{16}$. *Mater. Res. Bull.* **1977**, *12*, 189−195.

(52) Marques, A. P. A.; Motta, F. V.; Leite, E. R.; Pizani, P. S.; Varela, J. A.; Longo, E.; de Melo, D. M. A. Evolution of Photoluminescence as a Function of the Structural Order or Disorder in CaMoO$_4$ Nanopowders. *J. Appl. Phys.* **2008**, *104*.

(53) Pereira, P. F. S.; de Moura, A. P.; Nogueira, I. C.; Lima, M. V. S.; Longo, E.; de Sousa Filho, P. C.; Serra, O. A.; Nassar, E. J.; Rosa, I. L. V. Study of the Annealing Temperature Effect on the Structural and Luminescent Properties of SrWO$_4$:Eu Phosphors Prepared by a Non-Hydrolytic Sol-Gel Process. *J. Alloys Compd.* **2012**, *526*, 11−21.

(54) Cavalcante, L. S.; Batista, F. M. C.; Almeida, M. A. P.; Rabelo, A. C.; Nogueira, I. C.; Batista, N. C.; Varela, J. A.; Santos, M. R. M. C.; Longo, E.; Siu Li, M. Structural Refinement, Growth Process, Photoluminescence and Photocatalytic Properties of (Ba$_{1-x}$Pr$_{2x/3}$)WO$_4$ Crystals Synthesized by the Coprecipitation Method. *RSC Adv.* **2012**, *2*, 6438−6454.

(55) Clark, G. M.; Doyle, W. P. Infra-Red Spectra of Anhydrous Molybdates and Tungstates. *Spectrochim. Acta* **1966**, *22*, 1441.

(56) Siriwong, P.; Thongtem, T.; Phuruangrat, A.; Thongtem, S. Hydrothermal Synthesis, Characterization, and Optical Properties of Wolframite ZnWO$_4$ Nanorods. *CrystEngComm* **2011**, *13*, 1564−1569.

(57) McKechnie, J. S.; Turner, L. D. S.; Vincent, C. A.; Bonino, F.; Lazzari, M.; Rivolta, B. Silver Monotungstates, Ditungstates and Tetratungstates. *J. Inorg. Nucl. Chem.* **1979**, *41*, 177−179.

(58) Kubelka, P.; Munk, F. Ein Beitrag Zur Optik Der Farbanstriche. *Z. Tech. Phys.* **1931**, *12*, 593−601.

(59) Myrick, M. L.; Simcock, M. N.; Baranowski, M.; Brooke, H.; Morgan, S. L.; McCutcheon, J. N. The Kubelka-Munk Diffuse Reflectance Formula Revisited. *Appl. Spectrosc. Rev.* **2011**, *46*, 140−165.

(60) Tang, J. W.; Ye, J. H. Correlation of Crystal Structures and Electronic Structures and Photocatalytic Properties of the W-Containing Oxides. *J. Mater. Chem.* **2005**, *15*, 4246−4251.

(61) Kim, D. W.; Cho, I.-S.; Lee, S.; Bae, S.-T.; Shin, S. S.; Han, G. S.; Jung, H. S.; Hong, K. S. Photophysical and Photocatalytic Properties of Ag$_2$M$_2$O$_7$ (M = Mo, W). *J. Am. Ceram. Soc.* **2010**, *93*, 3867−3872.

(62) Longo, V. M.; Cavalcante, L. S.; Paris, E. C.; Sczancoski, J. C.; Pizani, P. S.; Li, M. S.; Andres, J.; Longo, E.; Varela, J. A. Hierarchical Assembly of CaMoO$_4$ Nano-Octahedrons and Their Photoluminescence Properties. *J. Phys. Chem. C* **2011**, *115*, 5207−5219.

(63) Yin, Y.; Gao, Y.; Sun, Y.; Zhou, B.; Ma, L.; Wu, X.; Zhang, X. Synthesis and Photoluminescent Properties of Camoo4 Nanostructures at Room Temperature. *Mater. Lett.* **2010**, *64*, 602−604.

(64) Groenink, J. A.; Hakfoort, C.; Blasse, G. Luminescence of Calcium Molybdate. *Phys Status Solidi A* **1979**, *54*, 329−336.

(65) Ryu, J. H.; Yoon, J. W.; Lim, C. S.; Oh, W. C.; Shim, K. B. Microwave-Assisted Synthesis of Camoo4 Nano-Powders by a Citrate Complex Method and Its Photoluminescence Property. *J. Alloys Compd.* **2005**, *390*, 245−249.

(66) Campos, A. B.; Simoes, A. Z.; Longo, E.; Varela, J. A.; Longo, V. M.; de Figueiredo, A. T.; de Vicente, F. S.; Hernandes, A. C. Mechanisms Behind Blue, Green, and Red Photoluminescence Emissions in CaWO$_4$ and CaMoO$_4$ Powders. *Appl. Phys. Lett.* **2007**, *91*.

(67) Xu, C.; Zou, D.; Guo, H.; Jie, F.; Ying, T. Luminescence Properties of Hierarchical CaMoO$_4$ Microspheres Derived by Ionic Liquid-Assisted Process. *J. Lumin.* **2009**, *129*, 474−477.

(68) Liu, T.; Chen, J.; Yan, F. Optical Polarized Properties Related to the Oxygen Vacancy in the CaMoO$_4$ Crystal. *J. Lumin.* **2009**, *129*, 101−104.

(69) Pu, C.; Liu, T.; Zhang, Q. Study of the Electronic Structures of CaMoO$_4$ Crystal Related to Oxygen Vacancy. *Phys. Status Solidi B* **2008**, *245*, 1586−1589.

(70) Longo, V. M.; de Figueiredo, A. T.; Campos, A. B.; Espinosa, J. W. M.; Hernandes, A. C.; Taft, C. A.; Sambrano, J. R.; Varela, J. A.; Longo, E. Different Origins of Green-Light Photoluminescence

1238

dx.doi.org/10.1021/jp408167v | *J. Phys. Chem. C* 2014, 118, 1229−1239

Emission in Structurally Ordered and Disordered Powders of Calcium Molybdate. *J. Phys. Chem. A* **2008**, *112*, 8920−8928.

(71) Wyckoff, R. W. G., *Crystal Structures*. Wiley: New York, 1948; Vol. *II*.

(72) Phuruangrat, A.; Thongtem, T.; Thongtem, S. Synthesis of Lead Molybdate and Lead Tungstate Via Microwave Irradiation Method. *J. Cryst. Growth* **2009**, *311*, 4076−4081.

(73) Phuruangrat, A.; Thongtem, T.; Thongtem, S. Barium Molybdate and Barium Tungstate Nanocrystals Synthesized by a Cyclic Microwave Irradiation. *J. Phys. Chem. Solids* **2009**, *70*, 955−959.

(74) Itoh, M.; Fujita, M. Optical Properties of Scheelite and Raspite Pbwo4 Crystals. *Phys. Rev. B* **2000**, *62*, 12825−12830.

(75) Nikl, M.; Bohacek, P.; Mihokova, E.; Kobayashi, M.; Ishii, M.; Usuki, Y.; Babin, V.; Stolovich, A.; Zazubovich, S.; Bacci, M. Excitonic Emission of Scheelite Tungstates AWO_4 (A = Pb, Ca, Ba, Sr). *J. Lumin.* **2000**, *87−9*, 1136−1139.

(76) Gracia, L.; Longo, V. M.; Cavalcante, L. S.; Beltran, A.; Avansi, W.; Li, M. S.; Mastelaro, V. R.; Varela, J. A.; Longo, E.; Andres, J. Presence of Excited Electronic State in $CaWO_4$ Crystals Provoked by a Tetrahedral Distortion: An Experimental and Theoretical Investigation. *J. Appl. Phys.* **2011**, *110*.

(77) Luo, Z. J.; Li, H. M.; Shu, H. M.; Wang, K.; Xia, J. X.; Yan, Y. S. Synthesis of $BaMoO_4$ Nestlike Nanostructures under a New Growth Mechanism. *Cryst. Growth Des.* **2008**, *8*, 2275−2281.

(78) Ghazi, S. M.; Zorriasatein, S.; Kanhere, D. G. Building Clusters Atom-by-Atom: From Local Order to Global Order. *J. Phys. Chem. A* **2009**, *113*, 2659−2662.

1239

dx.doi.org/10.1021/jp408167v | *J. Phys. Chem. C* 2014, 118, 1229−1239

2.4 – A Combined Experimental and Theoretical Study on the Formation of Ag Filaments on β-Ag$_2$MoO$_4$ Induced by Electron Irradiation

FULL PAPER

A Combined Experimental and Theoretical Study on the Formation of Ag Filaments on β-Ag₂MoO₄ Induced by Electron Irradiation

Juan Andrés,* Mateus M. Ferrer, Lourdes Gracia, Armando Beltran, Valeria M. Longo, Guilherme H. Cruvinel, Ricardo L. Tranquilin, and Elson Longo

A combined experimental and theoretical study is presented to understand the novel observed nucleation and early evolution of Ag filaments on β-Ag₂MoO₄ crystals, driven by an accelerated electron beam from an electronic microscope under high vacuum. The growth process, chemical composition, and the element distribution in these filaments are analyzed in depth at the nanoscale level using field-emission scanning electron microscopy (FE-SEM) and transmission electron microscopy (TEM) with energy-dispersive spectroscopy (EDS) characterization. To complement experimental results, chemical stability, structural and electronic aspects have been studied systematically using first-principles electronic structure theory within a quantum theory of atoms in molecules (QTAIM) framework. The Ag nucleation and formation on β-Ag₂MoO₄ are a result of structural and electronic changes of the AgO₄ tetrahedral cluster as a constituent building block of β-Ag₂MoO₄, consistent with Ag metallic formation. The formation of Ag filament transforms the β-Ag₂MoO₄ semiconductor from *n*- to *p*-type concomitant with the appearance of Ag defects.

1. Introduction

Metal tungstates and molybdates form a family of multicomponent metal oxide compounds, and many studies have been made regarding their interesting structures, intriguing physical and chemical properties, as well as a wide range of applications in photoluminescence, optical fibers, scintillator materials,

photochromism, humidity sensors, multiferroic materials, and catalysts.[1–19]

One member of the molybdate family, silver molybdate (Ag_2MoO_4) has been a target of intense investigation for its chemical stability at elevated temperatures and subsequent high-temperature lubricating properties[20] as well as its potential applications in electrochemical devices and gas-sensing,[20–24] and in surface-enhanced Raman scattering techniques.[23,25] Several studies have been made to obtain Ag_2MoO_4-based materials as flower-like,[26] nanoparticles[21] and wire-like nanostructures.[22] Low-dimensional Ag_2MoO_4 nanostructures have been obtained by Nagaraju et al.[27] who reported the synthesis of nanorods/nanowires/multipods and the photoluminescence of microrods; while Feng et al.[28] have been synthesized as ultra long orthorhombic silver trimolybdate nanowires. Qian et al.[29] have reported the microwave-assisted hydrothermal synthesis of cube-like $Ag-Ag_2MoO_4$ with visible-light photocatalytic activity. Bao et al.[30] reported on a room-temperature synthesis of Ag nanoparticles decorated with silver molybdate nanowires using a solution-based chemical reaction method. Fodjo et al.[25] have published a facile hydrothermal technique to synthesize Ag_2MoO_4 at relatively low temperatures (80 and 20 °C). Tang et al.[31] have obtained $Ag_2Mo_2O_7$/chitin composite gel-membranes, which were fabricated incorporating $Ag_2Mo_2O_7$ in the regenerated chitin gel-membranes via a green pathway. Cheng et al.[22] studied photoswitches of 1D Ag_2MO_4 (M = Cr, Mo, and W) and noticed the formation of silver nanoparticles at the surface of Ag_2MoO_4 under electron beam irradiation, as already previously reported during transmission electron microscopy (TEM) observation of other silver nanowires.[32]

The ability of chemists and physicists to interact with atoms, molecules, and solids at the quantum level, and the spatial scales of atoms and chemical bonds and on temporal scales of electron and nuclear motion has gained increasing sophistication through the development of precise photon and electron probes. In particular, electron probes have precise spatial resolution, which has enabled imaging of single atoms and atomic lattice contrast on surfaces and in solids. Scanning electron microscopy (SEM), scanning transmission electron microscopy

J. Andrés, Dr. L. Gracia, Prof. A. Beltran
Departament de Química Física i Analítica
Universitat Jaume I
12071 Castelló de la Plana, Spain
E-mail: andres@qfa.uji.es
M. M. Ferrer, R. L. Tranquilin
INCTMN-UFSCar
Universidade Federal de São Carlos
P.O. Box 676, 13565-905 São Carlos, SP, Brazil
L. Gracia, Prof. E. Longo
INCTMN-UNESP, Universidade Estadual Paulista
P.O. Box 355, CEP. 14801-907 Araraquara, SP, Brazil
V. M. Longo, G. H. Cruvinel
INCTMN-USP, Universidade de São Paulo
Instituto de Física de São Carlos
13560-970 São Carlos, SP, Brazil

(STEM), and TEM are well-recognized techniques that provide unique capabilities for in situ imaging and control of nanoscale phenomena.[33–37]

In recent years, papers on monitoring local structural and electronic changes generated by the electron beam within TEM have been started to appear, and TEM is a very powerful tool for the observation, fabrication, and manipulation of nanostructures with the advantages of precise nanoscale control,[38,39] in which high- energy electrons transmit through the specimen and provide useful electronic structure information of the samples based on a variety of electron–solid interactions.[40] Applying this technique, novel phenomena have been discovered in the process of TEM observation, such as nanoscale phase/shape transformation,[41] inorganic nanostructure modification,[42] colloid nanocrystal growth and self assembly,[36,43–47] lithium encapsulation and release in LiCl nanoshells and nanotubes,[48] nanostructure fabrication,[49] coalescence,[50] nanoscale crystallization, and some growth processes, which occur only in the beam's presence.[36,44,46,47,51,52] Different studies have quantified the role of the electron beam in affecting the chemical reactions being characterized.[44,52]

In particular, electron beam irradiation allows the preparation of noble and transition metal nanoparticles.[43,53] Pattabi et al.[54] have synthesized silver nanoparticles with enhanced antibacterial activity by using electron beam irradiation. During imaging, the electron beam interacts with the sample causing a novel phenomenon that occurs only in the beam's presence. In particular, an accurate understanding of the interactions between the electron beam and the material is essential to account for, suppress, and exploit the beam effects. First-principle calculations are essential in supporting the experimental observation to provide a deeper understanding of atomic and electronic structure that is already being exploited to explain their innovative properties and allow efficient exploration of new materials. In this context, very recently, the formation of Ag filaments on α-Ag$_2$WO$_4$ induced by electron irradiation[55] and their bactericidal[56] and photoluminescent applications,[57] as well their application as an efficient ozone sensor, have been reported.[58]

The crystal structure Ag$_2$MoO$_4$ obtained by Wyckoff[59] can be found in two forms: α-Ag$_2$MoO$_4$ has a tetragonal structure while β-Ag$_2$MoO$_4$ is cubic with a spinel structure.[59–61] The α-phase irreversibly transforms to the most stable β-phase upon heating above ambient temperature. Arora et al.[60] have studied the behavior of the cubic spinel phase of Ag$_2$MoO$_4$ at high pressure as characterized by X-ray diffraction and Raman spectroscopy, and, in this context, our group has studied the effect of pressure on β-Ag$_2$MoO$_4$[62] as a continuation of previous articles on the MgAl$_2$O$_4$ normal spinel and Zn$_2$SnO$_4$ inverse spinel structures.[63,64] Very recently, we have investigated a correlation between theoretical calculations and experimental data to explain the electronic structure and optical properties of β-Ag$_2$MoO$_4$ microcrystals.[65]

A novelty associated to the observed nucleation and early evolution of Ag filaments on β-Ag$_2$MoO$_4$ crystals is shown, driven by an accelerated electron beam from an electronic microscope under high vacuum. Here, we report on a comprehensive and combined experimental and theoretical work to understand the observed nucleation and early evolution of

Ag filaments on β-Ag$_2$MoO$_4$ crystals. We have studied the geometric and electronic structure of β-Ag$_2$MoO$_4$, and have derived a mechanism sequence using electron irradiation as relevant to early events for the formation and growth of Ag filaments from AgO$_6$ and MoO$_4$ clusters, as constituent polyhedra of β-Ag$_2$MoO$_4$. Quantum theory of atoms in molecules (QTAIM) developed by Bader and co-workers[66–68] allows the analysis of the experimental or theoretical electron density distribution, $\rho(r)$, in a solid, and the study of properties of $\rho(r)$ to reveal the bonding interactions in the crystal system, and the nature of these interactions. The electronic charge of each atom is evaluated using the Bader charge analysis within the QTAIM framework, which is a way of dividing molecules or solids into atoms based on electronic charge density. These computations envisaged in this study are thought to answer the questions: What happens with the electron excess as it approaches the surface and bulk of β-Ag$_2$MoO$_4$? How are the electrons distributed in this material and how can it is related with the structural and electronic evolution? How does the strength of the Ag—O and Mo—O bonds change after electron irradiation β-Ag$_2$MoO$_4$? We shall discuss how the analysis, provided from both experimental and theoretical results, of the structural and electronic structure of β-Ag$_2$MoO$_4$ allows us to explain the Ag nucleation process. The discussion will address the details of image acquisition and analysis and will provide a guide to interpret experimental results.

2. Results and Discussion

Figure 1 shows the X-ray diffraction (XRD) patterns of β-Ag$_2$MoO$_4$, which were prepared using the microwave-assisted hydrothermal method. All of the diffraction peaks of samples can be indexed as cubic structure without any deleterious phases, and with a space group of ($Fd\overline{3}m$) and point-group symmetry (O^7_h) and are in agreement with the standard values of Inorganic Crystal Structure Data (ICSD) base no. 28891.[61]
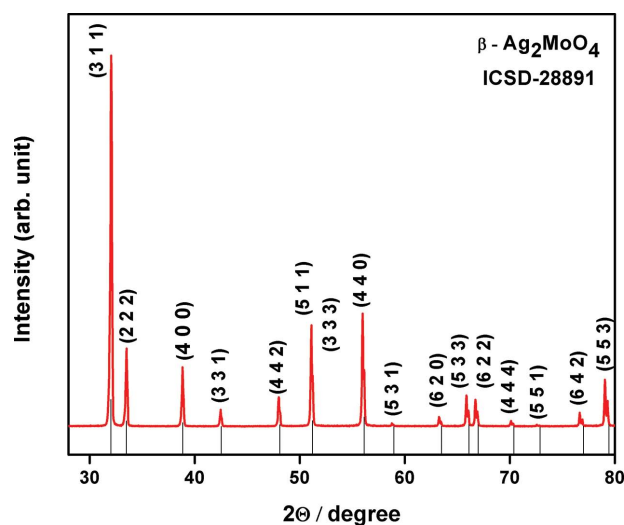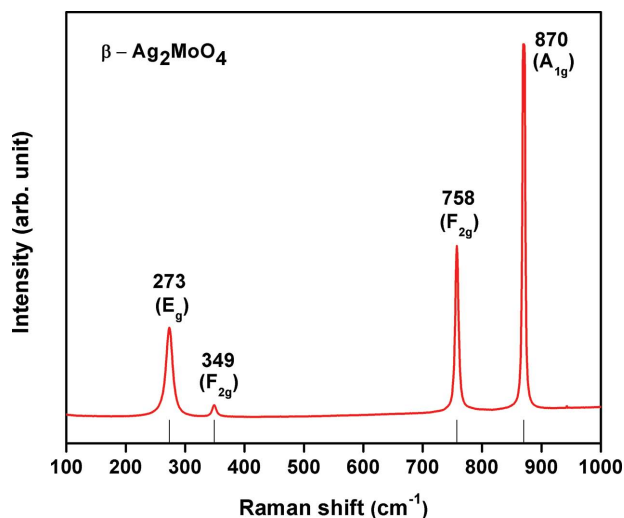

Figure 1. XRD of a β-Ag$_2$MoO$_4$ sample.

Figure 2. Raman spectrum of β-Ag_2MoO_4.

Figure 4. TEM image of β-Ag_2MoO_4.

Figure 2 shows the Raman spectrum of the as-prepared β-Ag_2MoO_4 between 100 and 1000 cm^{-1}. It is possible to verify the presence of four Raman active modes, which indicates the structural order at short range. The active Raman mode (E_g) located at 279 cm^{-1} corresponds to the external structure vibrations, which correspond to octahedral [AgO_6] clusters, while Raman mode (F_{2g}) found at 354 cm^{-1} is related to the torsional vibration of the [O—Mo—O] bonds present in the tetrahedral [MoO_4] clusters. Finally, the active Raman mode (A_{1g}) found at 873 cm^{-1} corresponds to the symmetric stretching vibration of the [←O←Mo→O→] bonds clusters present in the tetrahedral [MoO_4] clusters.[23,65]

Figure 3 shows a time-resolved series of FE-SEM images obtained under high vacuum (1×10^{-5} Pa) during the growth of Ag filaments stimulated by the electron beam on the β-Ag_2MoO_4 surface. Figure 3 a shows an FE-SEM image of
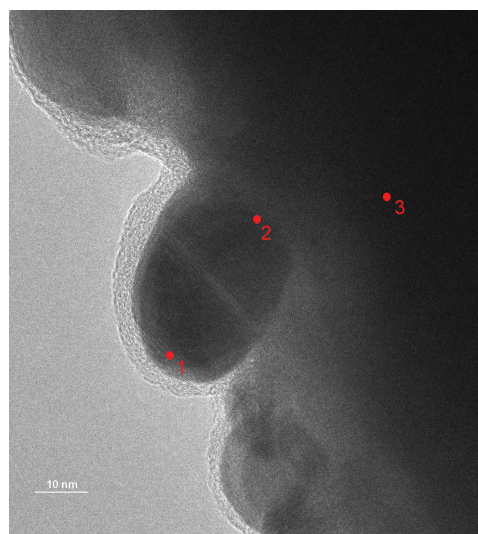
the crystals that were acquired after a rapid approach and focus adjustment (time zero). At this point, the image reveals a small amount of Ag on the surface. Figure 3b shows that after 2 min of exposure to a 30 kV electron beam, the particle shows some regions with Ag on the surface. It is interesting to note that the modifications, even small, occur after a few seconds of exposure. After 6 min of exposure, Figure 3 d, the metallic Ag seems to reach a limit point of growth. Further information, a short video (Video S1, Supporting Information) of the Ag growth is in the Supporting Information.

Figure 4 illustrates the TEM images with energy-dispersive spectroscopy (EDS) characterization. Results of the composition are shown in **Table 1**. Therefore, the end of the region that emerged due to the electron exposure (point 1) confirmed the composition of 100% of Ag in relation of Mo. Furthermore, it is possible to see the crystallographic planes revealing the Ag crystallinity. The region near the interface and inside the particles, points 2 and 3, consisted of about 64% of Mo to 36% of Ag. These results reinforce the fact that the Ag atoms come from the interior deep regions of the particles. This behavior provokes the presence of Ag defects inside β-Ag_2MoO_4 material and this semiconductor changes from *n* to *p* type.

Figure 5a shows the conventional cubic unit cell containing 8 formula units. Mo ions (gray atoms) occupy tetrahedral 8a sites while Ag ions (blue atoms) reside at the octahedral 16d position. Oxygen atoms (red atoms) stay at 32e positions. Arora et al.[60] performed powder XRD measurements at ambient pressure obtaining a single-phase material with a lattice parameter of 9.313 Å. Our calculations at ambient pressure yield a lattice parameter of 9.427 Å, which is only 1.2% greater than the experimental value.[62] The primitive unit cell is depicted in Figure 5 b), with only 2 formula units.

Figure 3. Time-resolved FE-SEM images of β-Ag_2MoO_4.

Table 1. Ag and Mo relationship shown by EDS.

Points	Ag [%]	Mo [%]
1	100	0
2	61	38
3	64	36

In sense to understand the quantum phenomenon observed experimentally of electron absorption, we introduced electrons, separately, up to 10 in the cluster constituent of the cubic unit cell of β-Ag_2MoO_4. The values for the distances Ag—O and Mo—O as a function of the number of electrons, N, are shown in **Figure 6**. In the case of Ag—O distances, there is a pronounced increase with the addition of electrons.

An analysis of the results presented in **Figure 7** shows that the Ag atoms of the $[AgO_6]$ clusters are the more prone to be reduced. At $N = 4$, practically all Ag atoms are reduced whereas, there is a minor decrease of the electron density is sensed for Mo atoms (that form $[MoO_4]$ clusters) (a decrease of 0.2 units at $N = 4$). Therefore, the electron excess imposed in the material is transferred from one cluster to another through the lattice network and the Ag formation process involves $[AgO_6]$ adjacent clusters, and to a minor extent the $[MoO_4]$ clusters.

2.1. Bond Critical Points Densities and Its Laplacian

The calculations of the charge density, ρ_{bcp}, at the (3,–1) bond critical points (BCP) as well as its Laplacian, $\nabla^2\rho_{bcp}$, in Ag—O bonds for $[AgO_6]$ units are presented in **Table 2**. The effect of adding electrons to the material produces striking differences in the values of the Laplacian and charge density at the (3,–1) BCP. Thus, it is worth noting that the Ag—O bonds considerably reduce their Laplacian and charge density values as the number of electrons is added indicating that these bonds become less strong in favor of the formation of metallic Ag.

3. Conclusion

The dynamics and the state properties of excess electrons, provided by an electron beam of TEM, have attracted widespread interest due to the fundamental importance of this process in
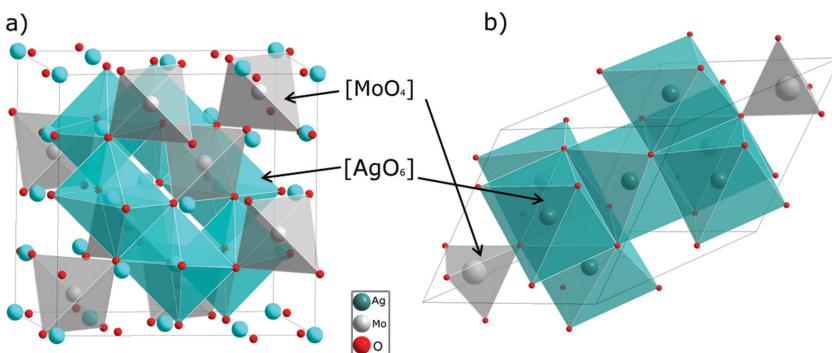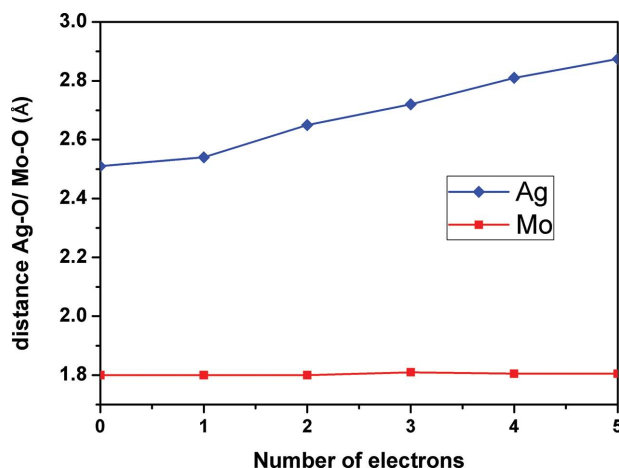
Figure 6. Ag—O and Mo—O distances as a function of the number of electrons added, N.

physics, chemistry, and biology. The electron beam irradiation in TEM provokes the synthesis of nanomaterials and investigating their morphology, structure, and chemical transformation, which is of importance for the development of novel nanostructures, especially for those that cannot be obtained using conventional chemical and physical methods.

Electron–material interactions offer an alternative approach to control the electronic structure and thus the chemical and physical properties, and the corresponding activities. In particular, the addition of electrons generated large change in the charge density resulting in bond modifications. As a consequence, a wide range of different chemistries can be initiated by electron–material interactions.

We report the in situ growth of Ag on β-Ag_2MoO_4, never observed before, by electron beam irradiation, and this work provides a fundamental perspective on the chemistry initiated by electrons on β-Ag_2MoO_4 via a nonclassical mechanism. This insight is relevant to apparently unrelated topics such as surface functionalization or electron beam-induced deposition processes. Moreover, mutual awareness of the common concepts of these different fields will also help to solidify the broader understanding of electron-initiated process because each field, and others, can provide examples that reveal principles of common interest. Electron-initiated chemistry therefore remains an active and dynamic research area and many more interesting discoveries and applications can be expected.

The present study communicates intimate details on the internal processes and these findings raise fundamental questions about the physical nature of this phenomenon itself. The results derived from the present study are based on the information provided by the joint analysis of experimental and theoretical work to provide a deeper insight and understanding of increasingly complex functional materials, and can be considered as a clear example of a complex modeling paradigm as was introduced by Billinge and Levin.[69]
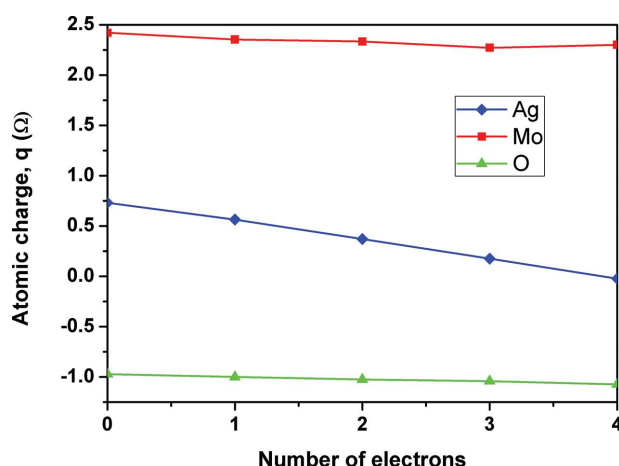

Figure 5. Spinel structure of β-Ag_2MoO_4; a) conventional cell and b) primitive cell.

FULL PAPER

Figure 7. Bader charge density of Ag, Mo, and O centers (of [AgO$_6$] and [MoO$_4$] clusters) as a function of the number of electrons added. q(Ω) represents the number of valence electrons minus the calculated charge density.

4. Experimental Section

Synthesis of β-Ag$_2$MoO$_4$: β-Ag$_2$MoO$_4$ microcrystals were prepared at room temperatures without the use of any surfactant by a simple precipitation method. The typical β-Ag$_2$MoO$_4$ crystals synthesis procedure is described as follows: 1×10^{-3} moles of molybdate sodium dihydrate (Na$_2$MoO$_4$.2H$_2$O; 99.5% purity; Sigma–Aldrich) and 2×10^{-3} moles of silver nitrate (AgNO$_3$; 99.8% purity; Sigma–Aldrich) were each separately dissolved in 50 mL of deionized water. The silver solution was dripped into the molybdate solution under stirring. The resulting suspensions were washed with deionized water several times to remove remaining ions and dried at 60 °C for 12 h.

Experimental Characterizations of β-Ag$_2$MoO$_4$: The β-Ag$_2$MoO$_4$ crystals were structurally characterized by XRD patterns using a diffractometer model LabX XRD-6000 (Shimadzu, Japan) with Cu–Kα radiation (λ = 1.5406 Å) in the 2θ range from 20° to 80° in the normal routine with a scanning velocity of 1 ° min^{-1}. Micro-Raman measurements were recorded using the (Horiba; Jobin-Yvon, France) model LabRAM HR 800 mm.

The shapes, sizes, visualization of Ag filaments, and element distribution of the β-Ag$_2$MoO$_4$ microcrystals were observed with a field-emission scanning electron microscope (FEG-SEM) model Supra 35-VP, Carl Zeiss, Germany operated at 20 kV, and TEM operating at 200 KV, and energy-dispersive spectroscopy (EDS); model Tecnai G2TF20, FEI.

Theoretical Calculations: First-principle total-energy calculations were carried out within the periodic density-functional-theory (DFT) framework using the VASP program.[70,71] The Kohn–Sham equations have been solved by means of the Perdew, Burke, and Ernzerhof exchange-correlation functional,[70] and the electron–ion interaction as described by the projector-augmented-wave pseudopotentials.[72,73]

Table 2. Charge density at the (3,–1) BCPs and its Laplacian in Ag—O bonds for [AgO$_6$] clusters as a function of the number of electrons added, N.

	Ag—O	
N	ρ_{bcp}	$\nabla^2\rho_{bcp}$
0	0.26	3.21
1	0.16	1.93
2	0.11	1.18
3	0.08	0.79
4	0.06	0.61

Due to the well-known limitations of standard DFT in describing the electronic structure of "strongly-correlated" compounds, a correction to the PBE wavefunctions is adopted (PBE+U) with the inclusion of a repulsive on-site Coulomb interaction U following the method of Dudarev et al.[74] Eventually the value of the Hubbard parameter was tested and a value of U = 6 eV was used. The plane-wave expansion was truncated at a cut-off energy of 400 eV and the Brillouin zones have been sampled through Monkhorst-Pack special k-points grids that as sure geometrical and energetic convergence for the Ag$_2$MoO$_4$ structures considered in this study. The keyword NELECT has been used in order to increase the number of electrons in the bulk structure, and all the crystal structures are optimized simultaneously on both the volume of the unit cell and the atomic positions. The relationship between charge density topology and elements of molecular structure and bonding was noted by Bader.[66,75] This relationship, Bader's QTAIM,[66–68] is now a well-recognized tool used to analyze electron density, to describe interatomic interactions, and to rationalize chemical bonding. The different strong and weak interactions between two atoms can be determined unequivocally from QTAIM calculations. According to the standard QTAIM framework, concepts such as (3,–1) BCPs, their respective bond paths (BPs), and $L(r) = -\nabla^2\rho(r)$ maps can be analyzed to reveal the nature of these interactions. A BCP serves as the origin of gradient lines of the electron density that define the interatomic surface or zero-flux surface (a surface that unambiguously defines the boundary between the two atoms and identifies the atomic basin), i.e., the electron density "belonging" to a specific atom.

Supporting Information

Supporting Information is available from the Wiley Online Library or from the author.

[1] V. B. Mikhailik, H. Kraus, G. Miller, M. S. Mykhaylyk, D. Wahl, *J. Appl. Phys.* **2005**, *97*, 083523.

[2] F. Amano, A. Yamakata, K. Nogami, M. Osawa, B. Ohtani, *J. Am. Chem. Soc.* **2008**, *130*, 17650.

[3] K. Fukuda, K. Akatsuka, Y. Ebina, R. Ma, K. Takada, I. Nakai, T. Sasaki, *Acs Nano* **2008**, *2*, 1689.

[4] M. Shang, W. Z. Wang, H. L. Xu, *Cryst. Growth Des.* **2009**, *9*, 991.

[5] S. Y. Song, Y. Zhang, Y. Xing, C. Wang, J. Feng, W. D. Shi, G. L. Zheng, H. J. Zhang, *Adv. Funct. Mater.* **2008**, *18*, 2328.

[6] Y. G. Su, L. P. Li, G. S. Li, *Chem. Mater.* **2008**, *20*, 6060.

[7] D. Ye, D. Z. Li, W. J. Zhang, M. Sun, Y. Hu, Y. F. Zhang, X. Z. Fu, *J. Phys. Chem. C* **2008**, *112*, 17351.

[8] L. W. Zhang, Y. J. Wang, H. Y. Cheng, W. Q. Yao, Y. F. Zhu, *Adv. Mater.* **2009**, *21*, 1286.

[9] Y. Zhao, Y. Xie, X. Zhu, S. Yan, S. X. Wang, *Chem. Eur. J.* **2008**, *14*, 1601.

650 wileyonlinelibrary.com

© 2015 WILEY-VCH Verlag GmbH & Co. KGaA, Weinheim

Part. Part. Syst. Charact. **2015**, *32*, 646–651

[10] L. Zhou, W. Z. Wang, H. L. Xu, S. M. Sun, *Cryst. Growth Des.* **2008**, *8*, 3595.

[11] Y. X. Zhou, Q. Zhang, J. Y. Gong, S. H. Yu, *J. Phys. Chem. C* **2008**, *112*, 13383.

[12] L. Gracia, V. M. Longo, L. S. Cavalcante, A. Beltran, W. Avansi, M. S. Li, V. R. Mastelaro, J. A. Varela, E. Longo, J. Andres, *J. Appl. Phys.* **2011**, *110*, 043501.

[13] V. M. Longo, L. Gracia, D. G. Stroppa, L. S. Cavalcante, M. Orlandi, A. J. Ramirez, E. R. Leite, J. Andres, A. Beltran, J. A. Varela, E. Longo, *J. Phys. Chem. C* **2011**, *115*, 20113.

[14] E. Orhan, F. M. Pontes, C. D. Pinheiro, E. Longo, P. S. Pizani, J. A. Varela, E. R. Leite, T. M. Boschi, A. Beltran, J. Andres, *J. Eur. Ceram. Soc.* **2005**, *25*, 2337.

[15] N. M. Batra, S. K. Arora, T. Mathews, *J. Mater. Sci. Lett.* **1988**, *7*, 254.

[16] M. R. D. Bomio, R. L. Tranquilin, F. V. Motta, C. A. Paskocimas, R. M. Nascimento, L. Gracia, J. Andres, E. Longo, *J. Phys. Chem. C* **2013**, *117*, 21382.

[17] W. S. Cho, M. Yashima, M. Kakihana, A. Kudo, T. Sakata, M. Yoshimura, *J. Am. Ceram. Soc.* **1997**, *80*, 765.

[18] F. Lei, B. Yan, H. H. Chen, Q. Zhang, J. T. Zhao, *Cryst. Growth Des.* **2009**, *9*, 3730.

[19] J. C. Sczancoski, L. S. Cavalcante, N. L. Marana, R. O. da Silva, R. L. Tranquilin, M. R. Joya, P. S. Pizani, J. A. Varela, J. R. Sambrano, M. S. Li, E. Longo, J. Andres, *Curr. Appl. Phys.* **2010**, *10*, 614.

[20] W. Gulbinski, T. Suszko, *Wear* **2006**, *261*, 867.

[21] S. Bhattacharya, A. Ghosh, *Phys. Rev. B* **2007**, *75*, 092103.

[22] L. Cheng, Q. Shao, M. W. Shao, X. W. Wei, Z. C. Wu, *J. Phys. Chem. C* **2009**, *113*, 1764.

[23] E. Y. Liu, W. Z. Wang, Y. M. Gao, J. H. Jia, *Tribol. Lett.* **2012**, *47*, 21.

[24] A. Sanson, F. Rocca, C. Armellini, S. Ahmed, R. Grisenti, *J. Non-Cryst. Solids* **2008**, *354*, 94.

[25] E. K. Fodjo, D.-W. Li, N. P. Marius, T. Albert, Y.-T. Long, *J. Mater. Chem. A* **2013**, *1*, 2558.

[26] D. P. Singh, B. Sirota, S. Talpatra, P. Kohli, C. Rebholz, S. M. Aouadi, *J. Nanopart. Res.* **2012**, *14*, 781.

[27] G. Nagaraju, G. T. Chandrappa, J. Livage, *Bull. Mater. Sci.* **2008**, *31*, 367.

[28] M. Feng, M. Zhang, J.-M. Song, X.-G. Li, S.-H. Yu, *ACS Nano* **2011**, *5*, 6726.

[29] L. Z. Qian, C. X. Tai, X. Z. Ling, *Sci. China Chem.* **2013**, *56*, 443.

[30] Z. Y. Bao, D. Y. Lei, J. Dai, Y. Wu, *Appl. Surf. Sci.* **2013**, *287*, 404.

[31] H. Tang, A. Lu, L. Li, W. Zhou, Z. Xie, L. Zhang, *Chem. Eng. J.* **2013**, *234*, 124.

[32] X. J. Cui, S. H. Yu, L. L. Li, L. Biao, H. B. Li, M. S. Mo, X. M. Liu, *Chem. Eur. J.* **2004**, *10*, 218.

[33] N. de Jonge, F. M. Ross, *Nat. Nanotechnol.* **2011**, *6*, 695.

[34] R. F. Egerton, P. Li, M. Malac, *Micron* **2004**, *35*, 399.

[35] L. R. Parent, D. B. Robinson, T. J. Woehl, W. D. Ristenpart, J. E. Evans, N. D. Browning, I. Arslan, *ACS Nano* **2012**, *6*, 3589.

[36] T. J. Woehl, J. E. Evans, L. Arslan, W. D. Ristenpart, N. D. Browning, *ACS Nano* **2012**, *6*, 8599.

[37] T. J. Woehl, K. L. Jungjohann, J. E. Evans, I. Arslan, W. D. Ristenpart, N. D. Browning, *Ultramicroscopy* **2013**, *127*, 53.

[38] D. Tham, C. Y. Nam, J. E. Fischer, *Adv. Mater.* **2006**, *18*, 290.

[39] M. Y. Yen, C. W. Chiu, F. R. Chen, J. J. Kai, C. Y. Lee, H. T. Chiu, *Langmuir* **2004**, *20*, 279.

[40] Y. Xu, L. Shi, X. Zhang, K. Wong, Q. Li, *Micron* **2011**, *42*, 290.

[41] A. H. Latham, M. E. Williams, *Langmuir* **2008**, *24*, 14195.

[42] J. H. Warner, *Adv. Mater.* **2008**, *20*, 784.

[43] J. U. Kim, S. H. Cha, K. Shin, J. Y. Jho, J. C. Lee, *J. Am. Chem. Soc.* **2005**, *127*, 9962.

[44] J. E. Evans, K. L. Jungjohann, N. D. Browning, I. Arslan, *Nano Lett.* **2011**, *11*, 2809.

[45] J. Park, H. Zheng, W. C. Lee, P. L. Geissler, E. Rabani, A. P. Alivisatos, *ACS Nano* **2012**, *6*, 2078.

[46] J. M. Yuk, J. Park, P. Ercius, K. Kim, D. J. Hellebusch, M. F. Crommie, J. Y. Lee, A. Zettl, A. P. Alivisatos, *Science* **2012**, *336*, 61.

[47] H. Zheng, R. K. Smith, Y.-w. Jun, C. Kisielowski, U. Dahmen, A. P. Alivisatos, *Science* **2009**, *324*, 1309.

[48] W. Neng, M. Martini, W.-n. Su, X. Ling, L.-t. Sun, Y.-t. Shen, *CrystEngComm* **2013**, *15*, 7872.

[49] D. Wan, M. Matteo, W. N. Su, L. Xu, L. T. Sun, Y. T. Shen, *CrystEngComm* **2013**, *15*, 7872.

[50] Y. Liu, X.-M. Lin, Y. Sun, T. Rajh, *J. Am. Chem. Soc.* **2013**, *135*, 3764.

[51] H.-G. Liao, L. Cui, S. Whitelam, H. Zheng, *Science* **2012**, *336*, 1011.

[52] K. W. Noh, Y. Liu, L. Sun, S. J. Dillon, *Ultramicroscopy* **2012**, *116*, 34.

[53] S. Sepulveda-Guzman, N. Elizondo-Villarreal, D. F. A. Torres-Castro, X. Gao, J. P. Zhou, M. Jose-Yacaman, *Nanotechnology* **2007**, *18*, 335604.

[54] R. M. Pattabi, K. R. Sridhar, S. Gopakumar, B. Vinayachandra, M. Pattabi, *Int. J. Nanopart.* **2010**, *3*, 53.

[55] E. Longo, L. S. Cavalcante, D. P. Volanti, A. F. Gouveia, V. M. Longo, J. A. Varela, M. O. Orlandi, J. Andres, *Sci. Rep.* **2013**, *3*, 1676.

[56] V. M. Longo, C. C. D. Foggi, M. M. Ferrer, A. F. Gouveia, R. S. André, W. Avansi, C. E. Vergani, A. L. Machado, J. Andrés, L. S. Cavalcante, A. C. Hernandes, E. Longo, *J. Phys. Chem. A* **2014**, *118*, 5769.

[57] E. Longo, D. P. Volanti, V. R. M. Longo, L. Gracia, I. A. C. Nogueira, M. A. P. Almeida, A. N. Pinheiro, M. M. Ferrer, L. S. Cavalcante, J. Andrés, *J. Phys. Chem. C* **2014**, *118*, 1229.

[58] L. F. da Silva, A. C. Catto, W. J. Avansi, L. S. Cavalcante; J. Andrés, K. Aguir, V. R. Mastelaro, E. Longo, *Nanoscale* **2014**, *6*, 4058.

[59] R. W. G. Wyckoff, *J. Am. Chem. Soc.* **1922**, *44*, 1994.

[60] A. K. Arora, R. Nithya, S. Misra, T. Yagi, *J. Solid State Chem.* **2012**, *196*, 391.

[61] J. Donohue, W. Shand, *J. Am. Chem. Soc.* **1947**, *69*, 222.

[62] A. Beltran, L. Gracia, E. Longo, J. Andrés, *J. Phys. Chem. C* **2014**, *118*, 3724.

[63] L. Gracia, A. Beltran, J. Andres, *J. Phys. Chem. C* **2011**, *115*, 7740.

[64] L. Gracia, A. Beltran, J. Andres, R. Franco, J. M. Recio, *Phys. Rev. B* **2002**, *66*, 224114.

[65] A. F. Gouveia, J. C. Sczancoski, M. M. Ferrer, A. S. Lima, M. R. M. C. Santos, M. S. Li, R. S. Santos, E. Longo, L. S. Cavalcante, *Inorg. Chem.* **2014**, *53*, 5589.

[66] R. F. W. Bader, *Atoms in Molecules: A Quantum Theory*, Clarendon Press Oxford, New York **1990**.

[67] C. F. Matta, R. J. Boyd, *The Quantum Theory of Atoms in Molecules*, Wiley-VCH, Weinheim, Germany **2007**.

[68] P. L. A. Popelier, *Atoms in Molecules: An Introduction*, Prentice Hall, Harlow **2000**.

[69] S. J. L. Billinge, I. Levin, *Science* **2007**, *316*, 561.

[70] G. Kresse, J. Furthmuller, *Comput. Mater. Sci.* **1996**, *6*, 15.

[71] G. Kresse, J. Hafner, *Phys. Rev. B* **1994**, *49*, 14251.

[72] G. Kresse, D. Joubert, *Phys. Rev. B* **1999**, *59*, 1758.

[73] J. P. Perdew, K. Burke, M. Ernzerhof, *Phys. Rev. Lett.* **1996**, *77*, 3865.

[74] S. L. Dudarev, G. A. Botton, S. Y. Savrasov, C. J. Humphreys, A. P. Sutton, *Phys. Rev. B* **1998**, *57*, 1505.

[75] P. Hohenberg, W. Kohn, *Phys. Rev. B* **1964**, *136*, B864.

Part. Part. Syst. Charact. **2015**, *32*, 646–651

© 2015 WILEY-VCH Verlag GmbH & Co. KGaA, Weinheim

wileyonlinelibrary.com **651**

2.5 – A 3D platform for the morphology modulation of materials: first principles calculations on the thermodynamic stability and surface structure of metal oxides: Co$_3$O$_4$, α-Fe$_2$O$_3$ and In$_2$O$_3$

A 3D platform for the morphology modulation of materials: first principles calculations on the thermodynamic stability and surface structure of metal oxides: Co_3O_4, α-Fe_2O_3, and In_2O_3

M M Ferrer[1], A F Gouveia[1], L Gracia[2], E Longo[3] and J Andrés[2]

[1] INCTMN-UFSCar, Universidade Federal de São Carlos, PO Box 676, 13565–905 São Carlos, SP, Brazil
[2] Department of Analytical and Physical Chemistry, University Jaume I (UJI), Castelló 12071, Spain
[3] INCTMN-UNESP, Universidade Estadual Paulista, PO Box 355, CEP 14801–907 Araraquara, SP, Brazil

E-mail: andres@qfa.uji.es

Abstract

Essentially, the exposed crystal planes of a given material, which primarily determine their morphology, tremendously affect its behavior. First principle calculations, based on the Wulff construction model and broken bonding density index, have been performed to calculate the equilibrium and their transformations for different metal oxides: Co_3O_4, α-Fe_2O_3, and In_2O_3. Present results point out that starting by surface thermodynamics is a helpful approach to predict and assess the morphology transformations of these materials. These complete set of morphologies may serve as a guide for researchers, when analyzing the images from electron microscopies, to gain further understanding of how to control crystal shape synthetically by tuning the surface chemistry and by controlling the relative values of surface energies.

Keywords: morphology, Wulff construction, surface energy, Co_3O_4, α-Fe_2O_3, In_2O_3

(Some figures may appear in colour only in the online journal)

M M Ferrer *et al*

1. Introduction

A few years ago, McIlroy *et al* [1] stated: 'Currently, there is a large divide between surface scientists and most catalysis researchers (who make and test new materials), caused by the inability of existing experimental and theoretical techniques to deal with the real-world nano-morphologies. Closing this divide would allow the entire surface science community to be much more effective.' In recent years, there has been such speed and development in this area that this is no longer a valid assessment. The current combination of theory, simulation, and experiment is not only capable of developing new functional materials with predictable and desirable properties, but also enables us to understand the nature of micro and nano-structures with novel morphologies.

Control of the morphology of micro and nanocrystals depends on factors such as the internal structure of the crystal and the external growth conditions. The surface facet energies can be modified by the use of different synthetic methods, reaction times, the nature of surfactants etc. In this sense, the rational design of nanomaterials is one of the holy grails of nanoscience and nanotechnology. The precise regulation and controlled synthesis of specific morphologies is crucial to enhance their performance in practical applications of micro and nanomaterials [2].

Predicting the 3D morphologies of crystalline materials can be used to guide the analysis of field-emission scanning electron microscopy images of the materials, and could be a very useful tool to design the synthesis of new materials. However, there are many scientific and technological challenges to overcome; in particular, we must understand the relationship between properties and structure.

Since various physical and chemical processes occur at surfaces, an understanding of the surface structure and the factors that affect surfaces is important. The shape of crystals grown under or near equilibrium conditions is governed mainly by surface energies, forming simple shapes with well-defined facets that can achieve minimum surface energy [3]. One method of predicting the morphology of a crystal is to calculate the energies of the different surfaces and these value can be associated to the fraction of surface atoms with unsaturated coordination shells, i.e. the number of under-coordinated surface atoms. The predominant surface will be the most stable surface; but measuring the geometries and energies of the surface facets is extremely challenging. In this context, surface energies are not readily acquired by experiment, and computer modeling and simulation are necessary to obtain these energies, being a powerful tool to explore the morphological mechanism at the atomistic/molecular level.

Theory and simulation in this research area should be further strengthened, which focuses on understanding the morphology, can guide the efficient synthesis of outstanding materials. First principles investigations are well established in the study of the morphology and surface properties of materials, from simple to complex metal oxides [4–27]. There are several insightful reviews that report experimental results and theoretical calculations on the most important aspects that govern crystal shape modulation in semiconductors and in metal nanoparticles [12, 28–31]. Theoretical works, in which surface modification by explicit or implicit solvation/hydration/redox effect are taken into account, can be considered the current state-of-the-art on theoretical methods and computing procedures. In this context, good illustrations have been published, as showed in these recent works: (1) the stabilization effect of surface impurities on the structure of ultrasmall ZrO_2 nanoparticles [32], (2) on the basis of theoretical predictions, Yang *et al* have synthesized uniform anatase TiO_2 single crystals with a high percentage of reactive facets [33], (3) theoretical investigations into the structure and surface thermodynamics of the (100) facet of Co_3O_4 at various

45

Modelling Simul. Mater. Sci. Eng. **24** (2016) 025007   M M Ferrer *et al*

redox conditions [34] as well as the morphological control of Co_3O_4 to enhace the oxidation of CO at low tempertaure [35], and (4) the mechanism of morphology transformation of tetragonal phase $LaVO_4$ nanocrystals controlled by surface chemistry: experimental and theoretical insights, in which equilibrium geometries, surface energies, and surface tensions are calculated for selected low-index surfaces of tetragonal $LaVO_4$ under the different surface passivated conditions [24].

Recently, we have determined the morphologies of several metal oxides such as SnO_2, $PbMoO_4$, and $CaWO_4$ using *ab initio* quantum mechanical calculations [15–20]. First principles calculations were also used to study the the effects of surface stability on the morphological transformation of different metals and metal oxides (Ag, anatase TiO_2, $BaZrO_3$, and α-Ag_2WO_4) [36]. Morphological transformations are due to the geometric constraints imposed by the crystal structure and are associated with the relative values of the surface energy of each face. In this context, and we have analyzed theoretical morphology modulation for α-Ag_2WO_4 [37], Ag_3PO_4 [38] and Ag_2MoO_4 [39] materials in order to explain the surface energy changes observed in experimental conditions, and how the knowledge of surface-specific properties can be utilized to design a number of crystal morphologies that may offer improved performance in various applications. It is important to remark that along our calculations specific solvent and/or surfactants interactions or hydration/redox effects on each face are not considered.

The main objective of this work is to show how the values of surface energies, obtained from first principle calculations *in vacuo*, can be used to obtain possible morphologies under thermodynamic equilibrium conditions for three metal oxides: Co_3O_4, α-Fe_2O_3, and In_2O_3 as well as to better understand the mechanism of morphological transformation at atomic level. The results of calculations have been compared with the experimental data. It is important to note the following aspects: (i) we have used the values of surface energy from literature, and we are confident that the proposed set of morphologies is not dependent on the calculation level; (ii) the values of surface energies are obtained *in vacuo*; (iii) from these values we are capable to predict the available morphologies for a crystalline material; (iv) by screening of the relative values of surface energies, a desired morphology can be obtained; (v) an analysis of how the idealized *in vacuo* surface results can be related to the *in situ* behavior, and this strategy allow us to find the target and control of crystal morphologies, as well as to rationalize the different channels starting from the ideal morphology.

The whole paper is arranged as follows: (2) a description of theoretical method and computational procedure, (3) the application of the method and the presentation of results, and (4) our main conclusions and perspectives close this letter.

2. Theoretical method and computational procedure

From the thermodynamic point of view, the free energy of the crystal facets (E_{surf}) determines the equilibrium shape by a classic Wulff construction, which minimizes the total surface free energy at a fixed volume [40]. The Wulff theorem provides a simple relationship between the E_{surf} of the $(h\,k\,l)$ plane and the distance, r_{hkl}, in the normal direction from the center of the crystallite. In addition, we have calculated the broken bonding density (D_b) index proposed by Gao *et al* [41] D_b, the number of bonds broken per area on creation of a new surface calculated from equation (1), where N_b is the number of broken bonds per unit cell area on a particular surface and A is the area of the surface unit cell.

$$D_b = N_b/A \tag{1}$$

46

Modelling Simul. Mater. Sci. Eng. **24** (2016) 025007   M M Ferrer *et al*

Table 1. Values of E_{surf}, number of broken bonds, area, and broken bonding density (D_b) calculated for Co_3O_4.

	Co_3O_4			
Surface	E_{surf} (J m^{-2})	Broken bonds	Area (nm^2)	D_b (nm^{-2})
(1 0 0)	0.92	12	0.3258	36.83
(1 1 0)	1.31	20	0.4607	43.41
(1 1 1)	2.31	15	0.2821	53.17
(1 1 2)	1.46	36	0.7980	45.11

3. Results and discussion

3.1. Co_3O_4

Co_3O_4 is a multifunctional material that has many applications and has received much theoretical and practical investigation [14, 42–45]. Co_3O_4 has a face centered cubic spinel structure, crystallizing in space group *Fd-3m*, and has two formula units ($Z = 2$) in the unit cell. Zasada *et al* [14] obtained the surface energies for the low index faces (1 0 0), (1 1 0), and (1 1 1) using calculations on a Co_3O_4 slab and compared the Wulff construction for this simulated material with the experimental morphology of a Co_3O_4 nanocrystal. Su *et al* [46] synthesized single crystalline Co_3O_4 nanocrystals with different exposed crystal planes and wide range of morphologies such as cubic, pseudo octahedral, nanosheets, and nanoplatelets, and so on. These authors found a correlation between the reducing charge − discharge overpotential with crystal planes of Co_3O_4 and established an order of catalytic activity: (1 1 1) > (1 1 0) > (1 1 2) > (1 0 0), and very recently, Liu *et al* [47] have confirmed the facet-dependent electrocatalytic performance of Co_3O_4 for rechargeable Li − O_2 battery.

The Wulff construction for Co_3O_4 structure has been obtained from the work of Su *et al* [46]. Table 1 lists the values of the surface energies obtained by Su *et al* [46] as well as the broken bonding density (D_b) of the faces used in the Wulff construction. The D_b values can be directly related to the order of surface stability because higher values represent the presence of a larger quantity of defects on the surface (broken bonds). For the Co_3O_4 simulated system, table 1 reveals that the order of stability of the faces is (1 0 0) > (1 1 0) > (1 1 2) > (1 1 1).

The complete set of morphologies for Co_3O_4 structure has been depicted in figure 1, in which the transformations can be obtained by changing the ratio bettwen the values of E_{surf} for each surface. Transformations between the different morphologies are due to the geometric constraints imposed by the crystal structure and are associated with the relative surface energy value of each surface. This interpretation has the advantage that all faces grow from the initial Co_3O_4 crystal (ideal) as function of their surface energy value. It is important to note that these images will serve as a guide to better interpret the morphological changes according to the synthetic method used, and so on. In addition, the different degrees of saturation at the surface, and consequently the different D_b values, in the simulated system play an important role in the predicted morphology of the crystal and these differences must be considered when comparing experimental and theoretical results. In a real system, the surfaces can adsorb species present during synthesis, and these adsorbed species will affect the surface energy and, thus, the final morphology, as shown in figure 1. Therefore, several research groups have been reported the synthesis of different morphologies of the Co_3O_4 indicated on figure 1, such as cubic (a) [46–49], octahedron (b) [47], and pseudo octahedron (c) [46], in which it is necessary to differ one of the (1 1 0)-surface group ($E_{surf}^{(1 1 0)*}$ can be $E_{surf}^{(1 1 0)}$ or $E_{surf}^{(0 1 1)}$ or $E_{surf}^{(1 0 1)}$).

47

Modelling Simul. Mater. Sci. Eng. **24** (2016) 025007   M M Ferrer *et al*
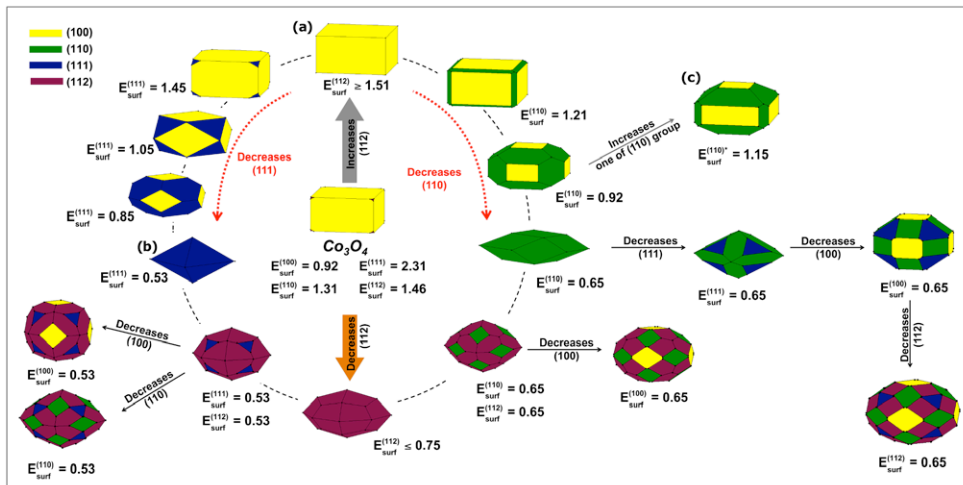
Figure 1. Crystallographic structure and morphologies of Co_3O_4 with crystal planes (1 0 0), (1 1 0), (1 1 1) and (1 1 2). Surface energy is in joule per·square meter.

3.2. α-Fe_2O_3

Iron nanomaterials are used in catalysts and electrodes, as medical imaging contrast agents, adsorbents, and magnetic recording devices. The morphology of individual particles is one of the determining factors in their performance, stability, and in the safety of both engineered nanoparticles as well as natural samples. For example, pseudocube-shaped hematite nanoparticles have a significantly larger permanent magnetization and coercivity than rice-shaped particles [50].

Hematite (α-Fe_2O_3) also has unique optical and electronic properties and is among the most important materials discussed in literature regarding energy-conversion processes [51–55]. Thus, there is considerable scientific and technological interest in the morphology of iron oxides, as it is demonstrated in various studies, reporting different morphologies synthesized via a template-free hydrothermal route [56], under the influence of $H_2PO_4^-$ ions [57], prepared by forced hydrolysis of ferric chloride [58], synthesized via an octadecylamine-assisted [59] and via atriphenyl-phosphine-assisted [60] hydrothermal method and with an oriented attachment mechanism controlled by different solvents [61]. Recently, a relationship between surface structure of hematite (0 0 1) and the macroscopic charging (zetapotential measurements in electrolyte solutions as a function of pH) has been reported [62], and the shape of Fe_3O_4 ferroferric oxide nanoparticles synthesized by a coprecipitation method as well as their electrochemical performances has been investigated [63]. Much effort is being directed towards the controlled synthesis of functional nanomaterials in which the shape and size can be engineered.

α-Fe_2O_3 crystallizes in the trigonal space group *R-3c*, and is isostructural with corundum, Al_2O_3. It is one of the most thermodynamically stable and abundant phases among all of the iron oxides and oxyhydroxides. Each rhombohedral unit cell contains four Fe atoms, distributed over two cation layers. The spins of the Fe atoms in the layers perpendicular to the [0 0 0 1] axis are aligned. The spin of the alternating layers is antiparallel, which leads to an antiferromagnetic material.

Guo *et al* [64] performed surface energy calculations for α-Fe_2O_3. The authors studied the most important surfaces of hematite: (0 0 1)-Fe, (0 1 2), (1 0 0) and (1 1 0), of which

48

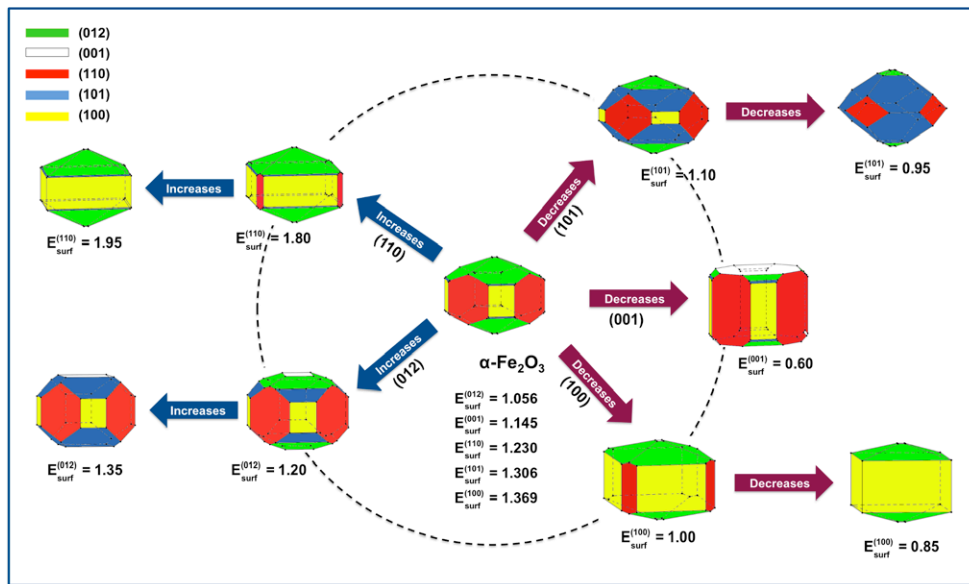Modelling Simul. Mater. Sci. Eng. **24** (2016) 025007   M M Ferrer *et al*

Figure 2. Crystallographic structure and morphologies of α-Fe$_2$O$_3$ with crystal planes (001), (012), (100), (101) and (110). Surface energy is in joule per·square meter.

(001) was the most extensively studied. The reported surface energies for these slabs and the morphologies generated by Wulff construction are shown in the center of figure 2. Central morphologies of figure 2 seem to be in agreement with scanning electron microscopy images of α-Fe$_2$O$_3$ particles formed in 5 mol% octadecylamine (ODA) for 48 h reported by Liu *et al* [59]. However, they reported a tetrakaidecahedral morphology increasing ODA to 12 mol% and enhancing the appearance of (112), (001) and (−112) facets over the other. The influence in morphology of temperature as well as a mixture EtOH/H$_2$O has been investigated [56] obtaining rhombohedra more or less truncated and cubic morphologies, which fit with some morphologies depicted in figure 2 involving different ratios of (012) and (100) surfaces.

Table 2 shows that the value for D_b index decreases in the order: (001)/Fe > (100) > (101) > (001)/O > (012) > (110), while the surface energy decreases in this order: (100) > (101) > (110) > (001)/Fe > (012) > (001)/O. Because H atoms were added to the (001)-O surface there is a large difference in the order of the (001)-O surface energy compared to the D_b representation. For this reason, the (001)-O surface energy was not used in the Wulff construction to generate the hematite morphology shown in figure 2. From the analysis of the (001)-O surface, it is clear that H atoms stabilized the under-coordinated O atoms on the surface, and this decreased both the surface energy and the density of broken bonds. In this system, the D_b values are not consistent with the simulated surface energy order. This can be related to the theoretical methodology used by Guo *et al* [64] to study the surface energy. That is, the surface model contained surface vacancies that are not fully explained.

3.3. In$_2$O$_3$

Indium oxide (In$_2$O$_3$) is an n-type highly degenerate wide band gap material that has many applications. Indium oxide is used in flat panel displays, photoelectric devices, windshield defrosting layers, heat-reflecting mirrors, high-transparency layers and gas sensor devices

49

Modelling Simul. Mater. Sci. Eng. **24** (2016) 025007 M M Ferrer *et al*

Table 2. Values of E_{surf}, number of broken bonds, area, and broken bonding density (D_b) calculated for α-Fe$_2$O$_3$.

	α-Fe$_2$O$_3$			
Surface	E_{surf} (J m^{-2})	Broken bonds	Area (nm^2)	D_b (nm^{-2})
(0 0 1)-Fe	1.145	12	0.2196	54.65
(0 1 2)	1.056	8	0.2733	29.27
(1 0 0)	1.369	28	0.6923	40.44
(1 0 1)	1.306	12	0.2421	49.57
(1 1 0)	1.230	8	0.3997	20.01
(0 0 1)-O	0.782	9	0.2196	40.99
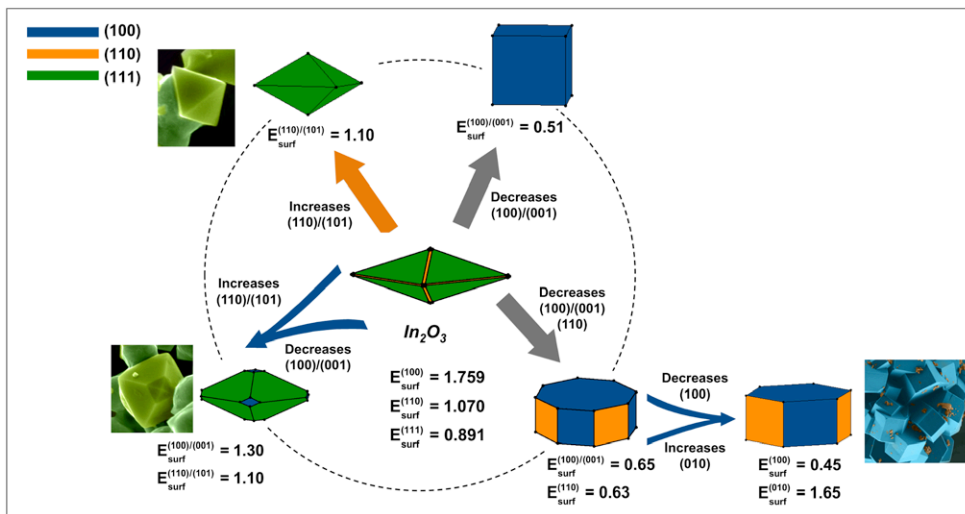
Figure 3. Crystallographic structure and morphologies of In$_2$O$_3$ with crystal planes (1 0 0), (1 1 0) and (1 1 1). Surface energy is in joule per·square meter.

[65]. The body-centered cubic polymorph of In$_2$O$_3$ crystallizes in the space group *Ia-3* with eight formula units ($Z = 8$) in the unit cell.

Walsh and Catlow [66] performed surface energy calculations for In$_2$O$_3$. We have used their surface values to generate the Wulff construction and the morphologies of In$_2$O$_3$. Figure 3 shows the energies, morphologies and the comparison with experimental results for In$_2$O$_3$ in our laboratory [67].

According to table 3, the order of stability using the D_b method is (1 1 1) < (1 1 0) < (1 0 0), the same as the theoretical surface energies. Thus, In$_2$O$_3$ surfaces with higher energies possess the highest amount of unsaturation on the surface.

4. Conclusions

It is mandatory to control the morphology of a micro/nanocrystal for for many scientific and technological applications. In this work, we used first principle calculations, based on the Wulff construction model and broken bonding density index, to investigate the effect of surface chemistry on the mechanism of morphology transformation of metal oxides: Co$_3$O$_4$, α-Fe$_2$O$_3$,

Modelling Simul. Mater. Sci. Eng. **24** (2016) 025007

M M Ferrer *et al*

Table 3. Values of E_{surf}, number of broken bonds, area, and broken bonding density (D_{b}) calculated for In_2O_3.

	In₂O₃			
Surface	E_{surf} (J m^{-2})	Broken bonds	Area (nm^2)	D_{b} (nm^{-2})
(1 0 0)	1.759	48	1.024	46.90
(1 1 0)	1.070	24	0.7238	33.16
(1 1 1)	0.891	42	1.773	23.69

and In_2O_3. Using a methodology recently developed by our research group, a detailed configurational analysis of the different faces was performed. A correlation between the broken bonding density (D_{b}) and the surface energies was found. The relaxed structures and surface energies were used to obtain a complete array of accessible morphologies. Manipulating the values of surface energy for each face plays a significant role, and it is exemplified in the aforementioned materials.

This method provides an approach with both predictive and explanatory capabilities and the results presented here are an illustration of how first principle calculations can rationalize the mechanisms stabilizing the morphology of micro- and nano-particles at the atomic level. The calculated diagrams relate the crystal growth conditions with the observed morphologies in an attempt to rationalize the morphologies obtained under different conditions. The morphological transformation of Co_3O_4, α-Fe_2O_3, and In_2O_3 materials revealed by this model was consistent with the Wulff construction.

Our results point out that starting by surface thermodynamics is a helpful approach to predict and assess the morphology transformation of materials and they are very useful in interpreting changes in crystal morphology. By this way, this method allow to understand how tuning the surface can control the shape of micro and nanocrystals synthetically. We expect that our work is beneficial to get a profound understanding of how to achieve shape-controlled materials synthesis than the normal trial and error synthetic procedure.

Acknowledgments

References

[1] McIlroy A *et al* 2006 *Basic Research Needs for Clean and Efficient Combustion of 21st Century Transportation Fuels* (US Dept. of Energy, Basic Energy Sciences, 2007) (http://science.energy.gov./~/media/bes/pdf/reports/files/ctf_rpt.pdf)
[2] Kuang Q, Wang X, Jiang Z, Xie Z and Zheng L 2014 *Acc. Chem. Res.* **47** 308–18
[3] Chen K, Sun C, Song S and Xue D 2014 *CrystEngComm.* **16** 5257–67
[4] Tompsett D A, Parker S C, Bruce P G and Islam M S 2013 *Chem. Mater.* **25** 536–41
[5] Kim Y, Lee H and Kang S 2012 *J. Mater. Chem.* **22** 12874–81
[6] Karim A, Fosse S and Persson K A 2013 *Phys. Rev.* B **87** 075322
[7] Eunseok L and Kristin A P 2013 *Nanotechnology* **24** 424007

M M Ferrer *et al*

[8]   Hörmann N G and Groß A 2014 *J. Solid State Electrochem.* **18** 1401–13
[9]   Li Y *et al* 2014 *Phys. Chem. Chem. Phys.* **16** 24604–9
[10] Barnard A S 2012 *Acc. Chem. Res.* **45** 1688–97
[11] Barnard A S and Kirkland A I 2008 *Chem. Mater.* **20** 5460–3
[12] Seyed-Razavi A, Snook I K and Barnard A S 2010 *J. Mater. Chem.* **20** 416–21
[13] Gurlo A 2011 *Nanoscale* **3** 154–65
[14] Zasada F *et al* 2011 *J. Phys. Chem.* C **115** 6423–32
[15] Stroppa D G *et al* 2011 *Chem. – Eur. J.* **17** 11515–9
[16] Beltrán A, Andrés J, Longo E and Leite E R 2003 *Appl. Phys. Lett.* **83** 635–7
[17] Leite E R, Giraldi T R, Pontes F M, Longo E, Beltrán A and Andrés J 2003 *Appl. Phys. Lett.* **83** 1566–8
[18] Stroppa D G *et al* 2014 *Phys. Chem. Chem. Phys.* **16** 1089–94
[19] Bomio M R D *et al* 2013 *J. Phys. Chem.* C **117** 21382–95
[20] Longo V M *et al* 2011 *J. Phys. Chem.* C **115** 20113–9
[21] Qi K *et al* 2014 *J. Phys. Chem.* C **118** 23320–7
[22] Piskorz W *et al* 2012 *J. Phys. Chem.* C **116** 19307–20
[23] Whiteside A, Fisher C A J, Parker S C and Saiful Islam M 2014 *Phys. Chem. Chem. Phys.* **16** 21788–94
[24] Li P *et al* 2012 *Cryst. Growth Des.* **12** 5042–50
[25] Suleiman I *et al* 2015 *Phys. Chem. Chem. Phys.* **17** 7038–45
[26] Kanaki E, Gohr S, Mueller C and Paulus B 2015 *Surf. Sci.* **632** 158–63
[27] Barmparis G D, Lodziana Z, Lopez N and Remediakis I N 2015 *Beilstein J. Nanotechnol.* **6** 361–8
[28] Lovette M A, Browning A R, Griffin D W, Sizemore J P, Snyder R C and Doherty M F 2008 *Ind. Eng. Chem. Res.* **47** 9812–33
[29] Chen J, Lim B, Lee E P and Xia Y 2009 *Nano Today* **4** 81–95
[30] Jiang Z-Y, Kuang Q, Xie Z-X and Zheng L-S 2010 *Adv. Funct. Mater.* **20** 3634–45
[31] Lee K, Kim M and Kim H 2010 *J. Mater. Chem.* **20** 3791–8
[32] Grena R *et al* 2015 *J. Phys. Chem.* C **119** 15618–26
[33] Yang H G *et al* 2008 *Nature* **453** 638–41
[34] Zasada F, Piskorz W and Sojka Z 2015 *J. Phys. Chem.* C **119** 19180–91
[35] Xie X, Li Y, Liu Z-Q, Haruta M and Shen W 2009 *Nature* **458** 746–9
[36] Andrés J, Gracia L, Gouveia A F, Ferrer M M and Longo E 2015 *Nanotechnology* **26** 405703–13
[37] Roca R A *et al* 2015 *Catal. Sci. Technol.* **5** 4091–107
[38] Botelho G, Andres J, Gracia L, Matos L S and Longo E 2015 *Chem Plus Chem.* doi: 10.1002/cplu.201500485
[39] Fabbro M T *et al* 2015 *Sci. Technol. Adv. Mater.* **16** 065002
[40] Wulff G 1901 *Z. Kristallogr.* **34** 449–530
[41] Gao Z-Y, Sun W and Hu Y-H 2014 *Trans. Nonferr. Met. Soc.* **24** 2930–7
[42] Mulinari T A, La Porta F A, Andres J, Cilense M, Varela J A and Longo E 2013 *CrystEngComm.* **15** 7443–9
[43] Sun H, Ang H M, Tade M O and Wang S 2013 *J. Mater. Chem.* A **1** 14427–42
[44] Yuan C, Zhang L, Hou L, Pang G and Oh W-C 2014 *RSC Adv.* **4** 14408–13
[45] Singh V, Kosa M, Majhi K and Major D T 2014 *J. Chem. Theory Comput.* **11** 64–72
[46] Su D, Dou S and Wang G 2014 *Sci. Rep.* **4** 5767
[47] Gao R, Zhu J, Xiao X, Hu Z, Liu J and Liu X 2015 *J. Phys. Chem.* C **119** 4516–23
[48] Mu J, Zhang L, Zhao G and Wang Y 2014 *Phys. Chem. Chem. Phys.* **16** 15709–16
[49] Xiao J, Kuang Q, Yang S, Xiao F, Wang S and Guo L 2013 *Sci. Rep.* **3** 2300
[50] Cao H, Wang G, Zhang L, Liang Y, Zhang S and Zhang X 2006 *ChemPhysChem.* **7** 1897–901
[51] Braun A *et al* 2012 *J. Phys. Chem.* C **116** 16870–5
[52] Hisatomi T *et al* 2012 *Faraday Discuss.* **155** 223–32
[53] Sivula K 2013 *J. Phys. Chem. Lett.* **4** 1624–33
[54] McKone J R, Lewis N S and Gray H B 2013 *Chem. Mater.* **26** 407–14
[55] Mayer M T, Lin Y, Yuan G and Wang D 2013 *Acc. Chem. Res.* **46** 1558–66
[56] Li X, Lei Y, Li X, Song S, Wang C and Zhang H 2011 *Solid State Sci.* **13** 2129–36
[57] Lv B, Xu Y, Wu D and Sun Y 2011 *CrystEngComm.* **13** 7293–98
[58] Wang W, Howe J Y and Gu B 2008 *J. Phys. Chem.* C **112** 9203–8
[59] Liu Z, Lv B, Wu D and Sun Y 2012 *Particuology* **10** 456–61
[60] Liu Z, Lv B, Wu D, Sun Y and Xu Y 2013 *Particuology* **11** 327–33

M M Ferrer *et al*

[61] Chakrabarty S and Chatterjee K 2013 *J. Cryst. Growth* **381** 107–13
[62] Lützenkirchen J *et al* 2015 *Faraday Discuss.* **180** 55–79
[63] Liang C *et al* 2015 *New J. Chem.* **39** 2651–6
[64] Guo H and Barnard A S 2011 *J. Mater. Chem.* **21** 11566–77
[65] Mehta B R and Singh V N 2005 *Pramana – J. Phys.* **65** 949–58
[66] Walsh A and Catlow C R A 2010 *J. Mater. Chem.* **20** 10438–44
[67] Motta F V, Lima R C, Marques A P A, Leite E R, Varela J A and Longo E 2010 *Mater. Res. Bull.* **45** 1703–6

3 – CONCLUSIONS

In summary, a set of published articles was presented reporting intimate details of the internal process of distinct behavior, and these findings brings new fundamental questions that open space for new researches.

The results derived from the present studies are based on the information obtained by the joint analysis of experimental and theoretical works to provide a deeper insight and understanding of complex functional materials.

It is possible to find several utilities for the use of quantum mechanics calculations about applications and design of materials. Among the results presented here, the photoluminescence emission of ZnS was modified with the substitution of small amount of Zn for Eu atoms (see pag. 5). Theoretical results provided support for the explanation of this fact and showed details about the behavior of the bonds and electronic bands.

Other example about the importance of the theoretical implementations in experimental systems was the new method about how to evaluate the morphology and the necessary configurations for its changes (see pag. 42). It is an important tool due to the relation of the properties and the surfaces of a crystal.

Besides the design of new materials, the theoretical tools were used also to the explanation of a new phenomenon caused by electron bombing, which was observed in Ag_2WO_4 and Ag_2MoO_4 crystals. The results showed that the Ag reduction caused the distancing of certain metallic Ag of other clusters and therefore, filaments of metallic Ag were observed during the electronic microscopy (see pag. 15, 23 and 35).

These methods provide an approach with both predictive and explanatory capabilities and the results presented here are an illustration of how first principle calculations and the experimental system interact perfectly. We expect that our works are beneficial to get a profound understanding of how to achieve desired materials synthesis than the normal trial and error synthetic procedure.

4 – REFERENCES

1.	DE GUIRE E. "History of Ceramics". The American Ceramic Society. 2014. Available on: http://ceramics.org/learn-about-ceramics/history-of-ceramics

2.	WANG L. & LI Y. "Controlled Synthesis and Luminescence of Lanthanide Doped NaYF$_4$ Nanocrystals." Chem. Mater., **19**: 727, 2007.

3.	ZHAI T., FANG X., BANDO Y., XU X., BANDO Y. & GOLBERG D. "Characterization, Cathodoluminescence, and Field-Emission Properties of Morphology-Tunable CdS Micro/Nanostructures". Adv. Funct. Mater., **19**: 2423, 2009.

4.	PANDEY K. C. "Reconstruction of Semiconductor Surfaces: Buckling, Ionicity, and π-Bonded Chains". Phys. Rev. Lett., **49**: 223, 1982.

5.	KRESSE G. & FURTHMÜLLER J. "Efficiency of ab-initio total energy calculations for metals and semiconductors using a plane-wave basis set". Comput. Mater. Sci., **6**: 15, 1996.

6.	KRESSE G. & HAFNER J. "Ab initio molecular-dynamics simulation of the liquid-metal-amorphous-semiconductor transition in germanium". Phys. Rev. B., **49**: 14251, 1994.

7.	DOVESI R., ORLANDO R., ERBA A., ZICOVICH-WILSON C. M., CIVALLERI B., CASASSA S., MASCHIO L., FERRABONE M., DE LA PIERRE M., D'ARCO PH., NOËL Y., CAUSÀ M., RÉRAT M. & KIRTMAN B. "CRYSTAL14: A program for the ab initio investigation of crystalline solids". Int. J. Quantum Chem., **114**: 1287, 2014.

8.	BISWAS S. & KAR S. "Fabrication of ZnS nanoparticles and nanorods with cubic and hexagonal crystal structures: a simple solvothermal approach". Nanotechnology., **19**: 045710, 2008.

9.	BREDOL M. & MERIKHI J. "ZnS precipitation: morphology control". J. Mater. Sci., **33**: 471, 1998.

10.	CALANDRA P., GOFFREDI M. & LIVERI V. T. "Study of the growth of ZnS nanoparticles in water/AOT/n-heptane microemulsions by UV-absorption spectroscopy". Colloids and Surfaces A., **160**: 9, 1999.

11.	YAMAMOTO T., KISHIMOTO S. & IIDA S. "Control of valence states for ZnS by triple-codoping method". Physica B., **308–310**: 916, 2001.

12.	WEN X., LI M., WANG Y., ZHANG J., FU L., HAO R., MA Y. & AI X. "Colloidal nanoparticles of a europium complex with enhanced luminescent properties". Langmuir., **24**: 6932, 2008.

13.	SILVA D., ABREU A., DAVOLOS M. & ROSALY M. "Determination of the local site occupancy of Eu^{3+} ions in ZnAl$_2$O$_4$ nanocrystalline powders". Opt. Mater., **33**: 1226, 2011.

14.	EKAMBARAM S. "Effect of host-structure on the charge of europium ion". J. Alloys Compd., **390**: L1, 2005.

15.	SAPRA S., PRAKASH A., GHANGREKAR A., PERIASAMY N. & SARMA D. "Emission properties of manganese-doped ZnS nanocrystals". J. Phys. Chem. B., **109**: 1663, 2005.

16.	CAVALCANTE L. S., ALMEIDA M. A. P., AVANSI JR W., TRANQUILIN R. L., LONGO E., BATISTA N. C., MASTELARO V. R. & SIU LI M. "Cluster coordination and photoluminescence properties of α-Ag$_2$WO$_4$ microcrystals". Inorg. Chem., **51**: 10675, 2012.

17.	ZIMAN J. M. "Models of disorder: the theoretical physics of homogeneously disordered systems: CUP Archive", 1979.

18.	KUANG Q., WANG X., JIANG Z., XIE Z. & ZHENG L. "High-energy-surface engineered metal oxide micro-and nanocrystallites and their applications". Acc. Chem. Res., **47**: 308, 2013.